FABRICATION, CHARACTERIZATION, AND OPTIMIZATION OF POROUS ELECTRODES FOR ELECTROCHEMICAL DESALINATION

BY

ERIK REALE

DISSERTATION

Submitted in partial fulfillment of the requirements
for the degree of Doctor of Science in Mechanical Engineering
in the Graduate College of the
University of Illinois Urbana-Champaign, 2021

Urbana, Illinois

Doctoral Committee:

Professor Kyle Smith, Chair
Professor Shen Dillon
Professor Gabriel Juarez
Professor Nenad Miljkovic

ABSTRACT

Faradaic deionization (FDI) is an emerging technique for the removal of salt ions from water due to Faradaic electrodes, such as those composed of Prussian blue analogues (PBAs), having high ion storage capacity. However, when compared with desalination technologies such as reverse osmosis, FDI is currently limited by impractically high energy consumption and low salt removal. The work in this dissertation is focused on reducing FDI energy consumption per unit salt removed by modifying the electrodes and surrounding desalination system to increase electronic conductivity, ionic conductivity, hydraulic permeability, and active material utilization of PBA electrodes. These modifications range in scale from control over colloidal forces between constituent microscopic particles in the electrode slurry, increasing electrode density, laser-milling of macroscopic ion-conducive patterns into the electrode, flow-through electrode cell design, and construction of an automated recirculating fluid system. Iterations were made as these techniques were developed, with experimental studies testing the reduction of energy consumption over previous designs and leading to the creation of an automated recirculating FDI cell using dense, patterned, highly conductive intercalation electrodes with an eightfold greater electrode area than the initial cell. This novel system can remove more than half the salt from influent with salinity comparable to seawater while achieving a thermodynamic energy efficiency of over 50%, far exceeding the performance of previous FDI systems. Higher removal rates are achievable at the cost of greater energy consumption, however experimental results demonstrate that FDI can be a highly efficient desalination technology. The combination of enhancements at every scale of the system has addressed the most significant practical challenges of FDI and brought the technology closer to viability.

ACKNOWLEDGEMENTS

I want to thank Dr. Kyle Smith for supporting me in my research, and my colleagues in the Smith Group who consistently aided my work. I also thank Professor Roland Cusick, Akash Bhat, Professor David Willis, and Haosen Tan for their collaboration. The research in this thesis was funded by the US National Science Foundation Award No. 1605290 – "SusChEM: Increasing Access to Sustainable Freshwater Resources with Membrane Capacitive Deionization", the US National Science Foundation Award No. 1931659, and by the Department of Mechanical Science and Engineering at the University of Illinois at Urbana-Champaign (UIUC). I thank Dr. Slawomir Porada for providing the YP-50 activated carbon used in early experiments, and Fitz Chem Corporation for providing Ketjen black material as a conductive additive in our electrodes. Scanning electron microscopy (SEM) was performed at the Materials Research Laboratory at UIUC, and X-ray computed tomography (CT) was performed at the Beckman Institute for Advanced Science and Technology. The MechSE Machine Shop, Rapid Prototyping Lab, and SCS Machine Shop were vital to the construction of experimental systems, as was the ME470 team of Adreet Agrawal, Brian Dardon, Nicholas DiCola, Lyle Regenwetter, and Sathvik Sanagala.

TABLE OF CONTENTS

LIST OF SYMBOLS

ε: porosity

τ: tortuosity, or half-cycle time (s)

Mc: Macmullin number

D: diffusivity (m^2/s)

ρ: density (kg/m^3)

ϕ: polarization (V)

c: salt concentration (mM)

C_{EDL}: specific capacitance (F/g)

Q: charge (C)

H: Heaviside function

$t_{-/+}$: transference number

$\dot{S}$: salt production rate (mol/s)

R_g: ideal gas constant (J/mol-K)

k: Boltzmann constant (J/K)

T: temperature (K)

F: Faraday constant (C/mol)

Z: impedance (Ω)

γ: constant phase exponent, or water recovery rate

α: Bruggeman exponent

i: current density (A/m^2)

σ_{eff}: effective electronic conductivity (S/m)

κ_{eff}: effective ionic conductivity (S/m)

κ_0: bulk ionic conductivity (S/m)

β: stretching factor

k_h: hydraulic permeability (m^2)

l: electrode length (m)

w: electrode thickness (m)

d: electrode width (m) or inter-particle distance (m)

μ: viscosity (Pa-s)

q: volumetric capacity (C/m^3)

$\dot{\forall}$: flow rate (m^3/s)

$\forall$: volume (m^3)

Λ: charge efficiency

p: pressure (Pa)

z: cation valence

e: elementary charge (C)

$ASAR$: average salt absorption rate (mol/min-cm^2)

SEC: specific energy consumption (kJ/mol)

TEE: thermodynamic energy efficiency

A: area (m^2) or Hamaker constant (J)

R: particle radius (m)

ζ: zeta potential (V)

λ_D: Debye length (m)

x: distance (m)

CHAPTER 1: INTRODUCTION

1-1 Background of electrochemical desalination

With more than half of the global population presently facing freshwater scarcity for one month during a given year [1], desalination of sea and brackish waters could increase freshwater access [2]. While reverse osmosis (RO) presently comprises the majority of global desalination capacity [3], high energy efficiency requires large RO plants, and brine concentrations must remain lower than 1.6 mol/L of monovalent salt assuming an 80 bar limit for spiral wound RO pressure vessels [4]. Brine production in RO is another problem, as recent analysis estimates that roughly 1.5 units of concentrated brine are globally generated for every unit of desalinated water, averaged across all water sources, sectors, and technologies [3]. Depletion of natural freshwater sources motivates the need for new water treatment technologies while also combatting climate change by consuming less energy, in addition to replacing aging infrastructure [5].

Electrically driven desalination processes avoid the mechanical limitations of RO by separating dissolved ions rather than driving water molecules through a membrane. Among such processes [6,7], Faradaic deionization (FDI) using cation intercalation materials (CIMs) shows great promise on the basis of reversible Na concentrations in the solid-state (namely 5.0 mol/L for the Prussian blue analogue investigated here with 65 mAh/g charge capacity and 2 g/cc nominal density) that exceed seawater salinity (0.5 mol/L as NaCl) by ten-fold. Techno-economic analysis of FDI and comparison with the more frequently studied capacitive deionization (CDI) shows the former method to output more desalinated water at a lower cost while being a more compact technology, in part due to the greater capacity of CIMs [8]. Despite early modeling that introduced a novel symmetric Na-ion battery architecture to realize seawater desalination using CIMs,

referred to as cation intercalation desalination (CID) [9–11], work in FDI has yet to produce potable water [12,13]. Individual improvements in properties such as capacity or permeability boast exceptional performance, but research in FDI often ignores other limitations of a system or does not combine new developments. The following chapters of this dissertation document several novel techniques and experimental studies which culminate in a final desalination cell containing improvements to electronic and ionic conductivity, hydraulic permeability, active particle loading, FDI cell design, and recirculating flow aiming to maximize salt removal and energy efficiency.

1-2 Thesis organization

The work in this dissertation covers several experimental studies making incremental improvements to electrochemical desalination systems, aiming to reduce energy consumption and increase salt removal from inflowing water. Electrode transport properties determine the energy required to desalinate water, including the ionic conductivity, electronic conductivity, and hydraulic permeability, each of which was targeted for improvement in addition to innovations in FDI cell design. As these techniques were studied, they were ultimately combined with the goal of creating a small-scale Faradaic deionization device able to desalinate water with NaCl content comparable to seawater.

Ionic conductivity was the first property studied in Chapter 2, and is determined by electrode microstructure restricting the paths of ions moving to reach active particles [14,15]. The addition of linear macroscopic pores can theoretically increase ionic conductivity by including ionically-conductive regions in electrode microstructure [16], though previously this method was only simulated. By micromachining such pores into the surface of capacitive electrodes, ionic conductivity was increased. Later developments led to the use of laser-milling, patterning

electrodes more expediently, in the form of an interdigitated pattern rather than macro-pores extending across an electrode's entire length.

Electronic conductivity determines utilization of active material due to the voltage difference from internal resistance, and the rate with which electrons can conduct to active particles. Over the course of the work presented in this thesis, methods of reducing energy consumption in FDI were studied through new electrode fabrication techniques. Increasing electronic conductivity is a primary goal of this research, as by reducing polarization more electrode material can be utilized within a voltage window small enough to prevent hydrogen evolution in the aqueous electrolyte. In Chapter 3, studies comparing effect of particle morphology and conductive additive content informed future selection of carbon black and led to investigation of inter-particle forces in an electrode slurry to understand how solidified microstructure was determined. Simulations of Li-ion electrode slurries showed conductivity could be influenced by particle morphology and slurry temperature [17,18], however such insights were not applied to real electrodes. Calendering, the process of compressing an electrode to reduce porosity, has proven able to increase electronic conductivity and rate capability [19], desirable improvements in an FDI cell which can be easily implemented. Understanding the forces between an electrode's particles at the microscopic scale also led to the development of more conductive electrode. In Chapter 5 it is shown how combining modifications to electrode fabrication, denser, more conductive electrodes can be manufactured to more efficiently remove salt.

The role of hydraulic permeability is also important FDI's development, as to ignore the mechanical limit of pumping power in RO, pressure drops and pumping energy losses from flowing electrolyte through the electrode must remain small. In flow-by cell architectures, pumping power is small enough to be considered negligible [20,21] because in such cases the

majority of the fluid is not flowing through the electrode's microscopic pores. However, flow-through electrodes which would require high pumping energies show superior performance over flow-by cases [18]. To reap the benefits of flow-through electrodes, a method of reducing pumping power was found by studying redox flow batteries, in which different pattern geometries are often studied for pressure drop reductions. The role of such electrodes is detailed in Chapter 7, combined with the macro-pores studied in Chapter 2.

As developments in electrode fabrication with targeted improvement of transport properties were implemented, a small-scale FDI cell was needed for testing. The earliest experiments with FDI, detailed in Chapter 4, were performed in a custom-made single-pass system containing PBA electrodes, and showed an order-of-magnitude reduction in energy consumption compared with other FDI research before reaching the limit of how much salt the system could remove. Gradients in concentration and state-of-charrge limited the utilization of the electrode [11], decreasing electrode utilization and preventing complete desalination. To overcome this limit, fluid recirculation was considered as a means of removing salt incrementally over many passes, and Chapter 6 focuses on optimization and testing of the system with increasingly dense and electronically conductivity electrodes. The recirculating cell removed the majority of the salt from the water, and achieved up to 80% thermodynamic energy efficiency (TEE). The next step was to increase the scale of the system to study how performance may change with the increased total capacity of the electrodes.

The final FDI cell produced has excellent electronic conductivity, ionic conductivity, and hydraulic permeability thanks to a combination of developments, including judicious choice of conductive addiction, colloid-inspired electrode solidification, calendering to high density, and laser-patterning of interdigitated macropores. Results obtained are explored in Chapter 7. This new

FDI cell is more energy efficient than any other before it, capable of removing over 60% of the salt from influent comparable to seawater, and the techniques which went into the cell's construction could advance the entire field. These techniques are shown in Figure 1-1, organized by ascending length scale as the system was developed. The developments in electrode fabrication and cell design have led to reductions in energy consumption and increases in salt removal far exceeding prior work, which typically reduced concentration by smaller amounts for lower-concentration influents [13,22–25]. FDI research which removed comparable levels of salt only did so in experiments without flow, neglecting the engineering challenges caused by cell design and pumping losses [26,27]. The final system described in Chapter 7 was able to remove 68% of salt from water with comparable salinity to seawater, with the achievable removal determined primarily by the concentration difference between brine and diluate, rather than initial concentration. Brine production remains a costly obstacle in the development of sustainably supplying potable water [3], requiring costly disposal processes such as discharge into large bodies or water, dedicated evaporation ponds, and deep well injection [28]. The disposal of brine can cause ecological damage, as marine organisms cannot survive the increase in salinity [29]. One limitation of RO is the pressure needed to desalinate high-concentration solutions becomes impractically high, creating an upper limit on how much water recovery is possible as the brine becomes more concentrated. The ability of FDI to operate with higher salinity influent than RO allows it to reduce brine concentration back to a level which RO can process, increasing water recovery rate and decreasing brine output, reducing disposal costs and environmental damage. With the developments in improvement of electronic conductivity, reduced pumping power requirements, and the recirculation system, the most significant obstacles to FDI's practicality have been resolved.

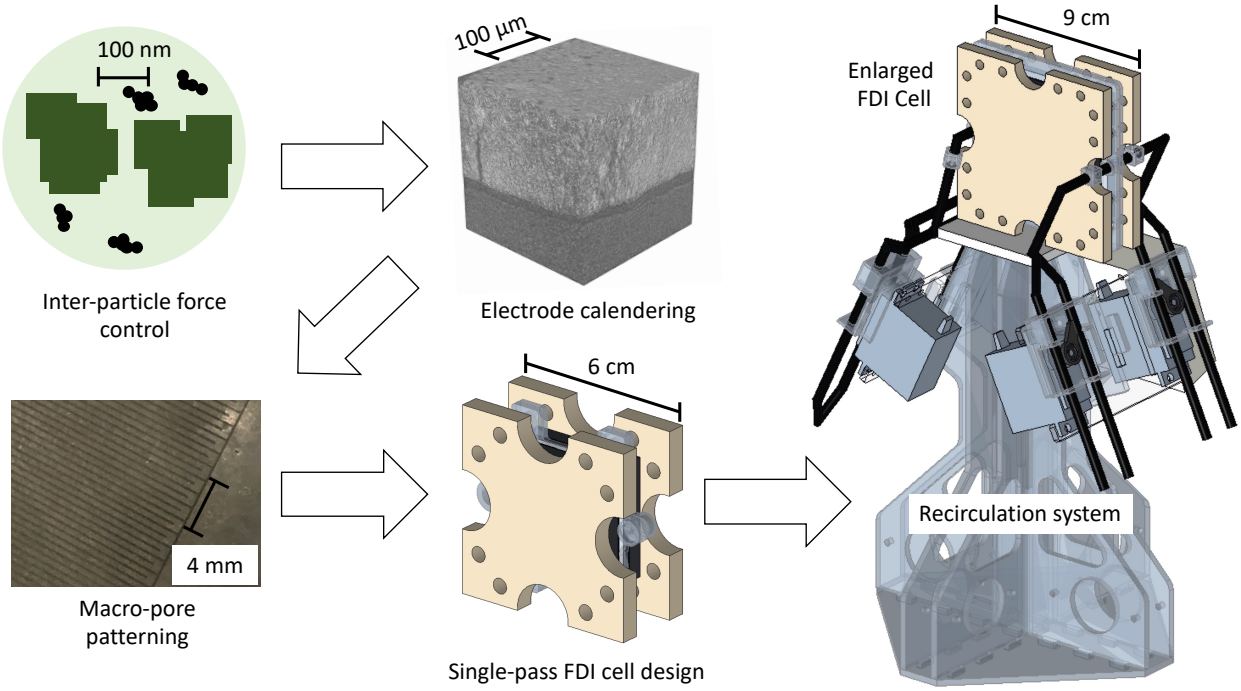

Figure 1-1: Views of the processes studied in this dissertation, leading from controlling forces between PBA and carbon black particles in slurry, to calendering dense electrodes, to macro-pore patterning, to the single pass FDI cell, and finally to the enlarged FDI cell with the recirculating flow system. The CAD assembly of the final desalination cell was made using Creo Parametric, including the core FDI cell, conductivity probes at the inlets and outlets, connecting tubes, and the valves which control fluid recirculation, all mounted on a support stand.

CHAPTER 2: MACRO-PORE PATTERNING AND CAPACITIVE DEIONIZATION

2-1 Ion transport in capacitive deionization

Potable water demand together with agricultural and industrial needs are likely to drive the desalination of seawater, wastewater, and brackish water resources, and capacitive deionization (CDI) is one potential technology for these purposes [6]. In CDI anions and cations are removed from feedwater solution by way of capacitive adsorption into electric double-layers (EDLs). The rate of salt removal in CDI ultimately influences the cost of water production, and, hence, achieving high salt removal rates is critical to making economical CDI devices. Salt removal rate typically increases with the current density used [30] because one electron is transferred for every monovalent ion adsorbed when co-ion adsorption is negligible. Thick electrodes in CDI have the potential to increase areal capacitance and enable the treatment of concentrated salt water, but such electrodes typically suffer from cracking during fabrication, increased ionic resistance, and energy consumption that typically restricts thickness to less than 350 μm [31]. While alternative strategies can be used to eliminate these effects (including flow-electrode architectures [32] and intercalation-based electrodes [33–35]) strategies to simultaneously increase salt removal rate with conventional EDL-based electrodes are desirable.

In porous electrodes, including both EDL- and intercalation-based, microstructure is known to influence internal resistance, capacitance, and energy efficiency. In particular, the tortuosity τ of a porous electrode material is the ratio of the microscopic path length that an ion takes within pores normalized by the Cartesian distance between the endpoints of the path [15,16,36]. In general, porous electrodes exhibit tortuosity exceeding unity as a result of the random arrangement of impenetrable solid matrix comprising the electrode. Aside from its

geometric interpretation, tortuosity impacts electrode charging dynamics by way of the effective ionic conductivity $\kappa_{eff} = \kappa_0 \varepsilon/\tau$ and the effective ionic diffusivity $D_{eff} = D_0 \varepsilon/\tau$, where κ_0 and D_0 are the bulk values of ionic conductivity and diffusivity, and ε is porosity [36–40]. The reduction of the effective transport property relative to its corresponding bulk value can be captured using the MacMullin number, Mc, from the following definition: $\kappa_{eff}/\kappa_0 = 1/Mc = \varepsilon/\tau$ [39].

While the tortuosity of microstructures with monodisperse pores typically increases with increasing total porosity [41], microstructures with two disparate structural length scales can be used to decrease apparent tortuosity at fixed porosity [16]. Such bi-tortuous electrodes have been studied in the context of Li-ion batteries experimentally [40] and theoretically [16,42,43]. Note that the term "bi-tortuous" refers to a bimodal distribution of pores with dissimilar tortuosity, in contrast with the anisotropic tortuosity with directionally dependent tortuosity [37,40,44] The orientation of solid particles comprising porous electrodes for energy storage has also been used as a strategy to control tortuosity experimentally, and thereby enhance cycling performance relative to conventionally fabricated electrodes [45,46].

The following chapter investigates ion transport in capacitive electrodes that use two disparate length scales of tortuosity, reprinting work from Ref. [47] with permission from the Journal of the Electrochemical Society. Experiments on eight different electrode samples having four different thicknesses, with and without such bi-tortuous structures, show that the addition of macroscopic, low-tortuosity pores aligned with the thru-plane direction improves electrode capacitance at high sweep rates. The tortuosity of both types of electrodes with several different geometric arrangements of macro-pores and with various salt concentration levels in the electrolyte is characterized using electrochemical impedance spectroscopy. The current

distributions within bi-tortuous electrodes of various thicknesses are also simulated using porous electrode theory to reveal the microscopic impact of macro-pores.

2-2 Electrode fabrication

To test the utility of bi-tortuous electrodes in CDI, activated carbon was chosen as a capacitive material for experimental tests of EDL capacitance. Electrode samples were prepared by mixing 85%-by-mass YP-50 activated carbon (Kuraray, Japan), 5% C45 carbon black (MTI, USA) as a conductive agent, and 10% polyvinylidene fluoride (PVDF) binder (MTI, USA). The solid electrode material was dissolved using 3 mL of N-methyl-2-pyrrolidone (NMP) solvent (MTI, USA) for every 1 gram of the powder mixture [48]. The carbon black was added in place of more active material to increase the electronic conductivity of the electrode so that the effective ionic conductivity controlled by solution concentration and electrode tortuosity would be the determining factor of the experiments [49,50]. Once all ingredients were combined, the slurry was homogenized in a Thinky Planetary AR-310 Mixer with 15 minutes for mixing, and 5 minutes for deaeration to ensure the resulting slurry was completely homogeneous and free of air bubbles. Fabrication of activated carbon electrodes was developed using recipes and procedures taken from literature, while the patterning process needed to make the bi-tortuous samples was developed specifically for this work.

A total of four electrodes were cast at different thicknesses onto sheets of 100 μm-thick graphite foil manufactured by CeraMaterials using an Elcometer film applicator. To ensure the graphite foil remained completely flat during casting, ethanol was sprayed onto the applicator before applying the foil, which was then pressed to push out the ethanol and to seal the foil onto the surface. Controlling the final thickness post-drying was imprecise as the dried electrodes were

approximately 1/3 the thickness they were cast at, as measured using an MTI precision thickness gauge with a resolution of 1 μm. Increasing thickness of the electrodes beyond 200 μm caused electrodes to crack upon drying, limiting the experiments to a total of four thicknesses. Solvent was removed from the sample through wet-phase inversion, keeping the cast electrodes immersed in deionized water for several hours as the water replaced the NMP [48,51]. After the solvent was replaced with deionized water, the electrodes were air-dried for two hours to remove any water and trace amounts of solvent, and to make them machinable. The total porosity of each dried electrode was calculated as $\varepsilon = 1 - \rho_{total}/\rho_{solid}$, where ρ_{solid} is the mass density of electrode constituents per unit solid volume (calculated to be 2.01 g/cc for the present recipe) and ρ_{total} is total density of the electrode determined by independent measurements of electrode mass, thickness, and area.

2-3 Macro-pore patterning

The cast samples then had linear macro-pores cut into a ~4 cm^2 area using a 100 μm diameter flat micro-mill manufactured by the Harvey Tool Company, at a spindle speed of 1200 rpm and a feed rate of 1 inch/minute. The depth of the trenches was targeted at >75% of the total electrode thickness, a limit in precision imposed by the end mill used, as spindle depth could only be controlled up to a resolution of 25 μm. The macro-pores were spaced to obtain a specific macro-pore coverage, defined as the total projected area of the macro-pores compared to the microporous electrode. The electrodes tested all possessed macro-pore coverage of 25% unless stated otherwise by spacing the 100 μm pores 400 μm apart, as this was found in previous simulations of bi-tortuous Li-ion batteries to produce the highest discharge capacity [16]. Following the patterning step, the

electrodes were immersed in deionized water for twelve hours to re-wet the microstructure and to remove air bubbles.

2-4 Cell assembly and testing

Completion of the patterning process ended preparation of the electrodes, which were then cut into circular samples, 12.5 mm in diameter. Samples were then submerged in 100 mM aqueous NaCl electrolyte and loaded into a two-electrode Swagelok cell with a 25 μm thick, 55% porous Celgard 3501 separator between the anode and cathode. The separator was cut into a rough circle with a diameter of ~14 mm to completely cover the electrodes and prevent short-circuiting. The molarity of the electrolyte was chosen as it is in the range of brackish water found in areas such as estuaries and deltas, which have salinity in between fresh and seawater [48,52]. The separators used, like the electrodes, were all submerged in DI water, followed by electrolyte, before assembly to ensure no air bubbles were trapped in the cell. The electrodes were then compressed between two solid graphite current collectors [15]. Cyclic voltammetry tests were performed over a voltage range of -0.1 to 0.1V, centered at 0V, at sweep rates between 1 and 30 mV/s for 5 cycles each, ensuring the final cycles were identical and unaffected by initial voltages or currents. This produced symmetric curves similar to what could be expected for charging and discharging in capacitive deionization applications, without using a large enough voltage that hydrogen evolution could occur in the aqueous electrolyte, though a practical CDI setup could use a voltage range between -1 and 1V with larger sweep rates resulting in similar charging times [30,53].

Electrochemical impedance spectroscopy (EIS) tests were also performed from 10 mHz to 100 kHz at an amplitude of 2 mV using the same Swagelok cell setup as the CV tests. In addition to the tests on samples of varying thickness, EIS experiments for varying concentration of aqueous

NaCl electrolyte were performed at concentrations of 10, 25, 50, 75, and 100 mM on a pair of 108 μm thick electrodes for both unpatterned and bi-tortuous cases made using the same recipe and process as constant-concentration experiments, though fabricated at a later time. The intent of this experiment was to find what, if any, effect a change in concentration would have on the tortuosity of the electrodes for molarities similar to brackish water [48,54].

2-5 Modeling details

The simulation model was based on the equations developed by Newman for modeling porous electrodes, which have been used in many previous studies of such materials in applications such as supercapacitors, batteries, and capacitive deionization [30,55,56]. This model takes into account current and salt conservation in the electrolyte, current conservation in the solid matrix, and capacitive electrosorption within capacitive particles. Excluding electrosorption processes, all of the preceding mechanisms are modeled using the governing equations and boundary conditions presented in Ref. [16]. In contrast with the cation intercalation reactions considered in Ref. [16], the charge-sign of ions that adsorb to the EDL, and consequently the adsorbed salt, depends on interfacial polarization $\Delta\phi = \phi_s - \phi_{ES}$, where ϕ_s is the solid-phase potential and ϕ_{ES} is the electrostatic potential. In porous electrode theory for cation intercalation cells electrolyte current conservation is posed in terms of "solution-phase potential" ϕ_e, which is more precisely defined as the reduced electrochemical potential of cations in solution given by $\phi_e = \phi_{ES} + RT/F\ ln(c_e)$, where c_e is salt concentration [16,33,57].

The EDL is modeled using Helmholtz theory for which the stored charge due to anions is $Q_- = -\rho_{total} C_{EDL} \Delta\phi H(\Delta\phi)$ and due to cations is $Q_+ = -\rho_{total} C_{EDL} \Delta\phi H(-\Delta\phi)$. C_{EDL} is the specific capacitance for which a value of 50 F/g is assumed, similar to the results from low sweep

rate capacitance measurements. H is the Heaviside function, with the discontinuity of is smeared by 5 mV to ease numerical convergence. The rate of salt production per unit total electrode volume within the electrolyte can then be expressed as $\dot{S} = \left(t_{-}\dot{Q}_{+} - t_{+}\dot{Q}_{-}\right)/F$. This salt production rate replaces the salt production term which appears in the salt transport equation in Ref. 10 to account for electrosorption of both cations and anions. Similar equations have been derived previously by Johnson and Newman [55]. The total rate of charge adsorption per unit electrode volume can also be expressed as $\dot{Q} = \dot{Q}_{+} + \dot{Q}_{-}$. This charge adsorption rate replaces the charge adsorption term which appears in the current conservation equations for both the electrolyte and the solid matrix.

Values for the tortuosity, porosity, and electrode thickness were all determined from experimental data described in the Results and Discussion section. The aqueous NaCl electrolyte was modeled as a dilute solution with ideal activity coefficients (i.e., the thermodynamic factor in Ref. [16] is unity) and considered a constant salt diffusion coefficient $D_0 = 1.61 \times 10^{-9}$ m^2/s, which is affected by the individual diffusion coefficients of cations and anions in solution [58]. Cation and anion transference numbers are assumed to be 0.39 and 0.61, respectively, corresponding to their dilute values [37]. Thermodynamically consistent values of ionic conductivity were thereby calculated assuming these parameters as $\kappa_0 = D_0 c_e F^2/\left(2R_g T t_{+} t_{-}\right)$ where F, R_g, and T are Faraday's constant, the gas constant, and temperature respectively [57,60]. This relation is noted to produce a constant equivalent conductance together with the assumed D_0 value, and that previous CDI models effectively produce constant equivalent conductance (for example see Refs. [56,61,62]). For the present simulations this assumption produces at most 20% larger ionic conductivity than experiment [63] for salt concentrations up to 100 mM.

As the simulations were of cyclic voltammetry, boundary conditions were set to apply a linearly time-dependent solid-phase potential to one current collector while the second current

collector acted as ground. Periodic boundary conditions were employed at the lateral edges of the domain with macro-pores placed at the center in the relevant cases. The model was implemented in MATLAB using the finite-volume method with implicit differencing in space and explicit differencing in time to find the spatiotemporal distribution of concentration and potential. Ref. [16] describes discretization and validation of the porous electrode code used here in greater detail. To simulate macro-pores the local porosity and tortuosity in the associated region of the electrode were both set to unity. Simulations were performed for several thicknesses spanning the range fabricated experimentally (approximately 50 to 200 μm).

2-6 Electrode capacitance characterization using cyclic voltammetry

Unpatterned and bi-tortuous electrode samples were tested using cyclic voltammetry (CV) and electrochemical impedance spectroscopy (EIS). The effects of electrode thickness, macro-pore coverage, and electrolyte salt concentration on the apparent tortuosity, capacitance, and impedance were explored. Complementary simulations were then performed to reveal how bi-tortuous electrode design affects electrolyte current distribution. In all results presented hereafter electrode samples were fabricated with an identical casting and drying process described in section 1-2 that resulted in a pre-patterned porosity of approximately 75% on average. Figure 2-1A shows a homogeneous distribution of activated carbon particles with 5-10 μm diameter embedded in an electrode with meso-pores visually estimated to be 10 μm or less. Bi-tortuous electrode samples were prepared from these unpatterned electrodes by precision mechanical milling (see Methods). Figure 2-1B shows macro-pores approximately 100 μm wide were generated as a result of this process. The machining process is noted to result in residual material and mild roughness at the top and side surfaces after milling. In all cases bi-tortuous electrodes of a given thickness had 72-

81% of the mass of their unpatterned counterparts, compared with 75% expected based on an ideal 100 μm wide trench repeated at 400 μm intervals.

Cyclic voltammetry was used to assess the capacitance of unpatterned and bi-tortuous electrode samples. First, the instantaneous capacitance (defined as current density divided by sweep rate) of 214 μm thick unpatterned and bi-tortuous electrodes is assessed as a function of applied cell voltage for several sweep rates, as shown in Figs. 2-1E and 2-1F respectively. The cyclic voltammograms (CVs) of both electrodes approach ideal response at 1 mV/s, where capacitance rises rapidly to a near-steady value. At this sweep rate the unpatterned electrode shows a terminal instantaneous capacitance of 747 mF/cm^2, while the bi-tortuous electrode shows 634 mF/cm^2. The 16% smaller value for the bi-tortuous electrode is the result of the mass removed during milling. As sweep rate increases the response of both electrodes becomes more dominated by resistive effects and the voltammograms depart from the ideal rectangular shape. This effect results from the finite time-scale for the transient development of current, the scaling of which is later considered with respect to electrode thickness. At the highest sweep rate tested (30 mV/s) the unpatterned electrode shows a terminal capacitance of 421 mF/cm^2, whereas the bi-tortuous electrode shows 525 mF/cm^2. While the capacitance of the bi-tortuous electrode compares unfavorably with the unpatterned one at low sweep rate (due to the less electrode mass), the low tortuosity of macro-pores within the bi-tortuous electrode reduces electrode resistance and enables sustained capacitance at high sweep rates.

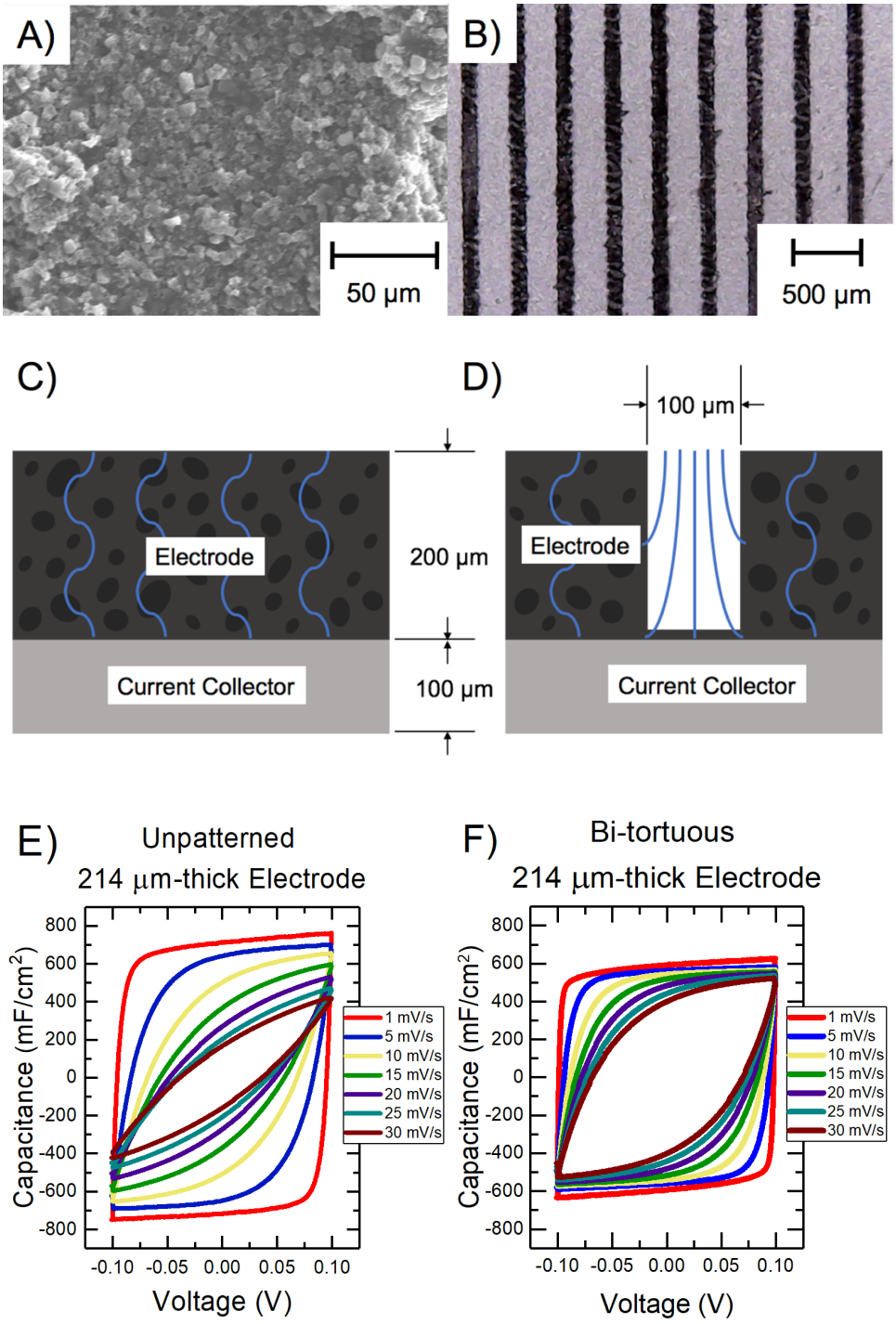

Figure 2-1. A) SEM image of the activated carbon particles on the surface of the cast electrodes. B) Optical image of a series of macro-pores milled into the surface of an activated carbon electrode with 25% macro-pore coverage. A simple illustration of the cross-sections of C) an unpatterned electrode and D) a bi-tortuous electrode cast onto a graphite foil current collector with a 100 µm wide macro-pore milled into it, including expected paths for the current to flow. E) and F) show the instantaneous areal capacitance values found from cyclic voltammetry curves for the

Figure 2-1 (cont.) unpatterned and bi-tortuous electrodes, respectively, calculated by dividing the instantaneous current density by the sweep rate to make the curves on the same scale and more visible. Data shown is from experiments on 214 μm-thick unpatterned and bi-tortuous electrodes, tested at sweep rates ranging from 1-30 mV/s.

After comparing the capacitive performance of unpatterned and bi-tortuous electrodes of a single thickness a range of electrode thicknesses (62, 102, 141, and 214 μm) were tested. For all bi-tortuous electrodes the macro-pore spacing and width were fixed to 400 and 100 μm, respectively. The addition of macro-pores and the resulting reduction of tortuosity allows ions to conduct more easily through electrolyte, but the significance of this effect is expected to depend on electrode thickness. For example, 50 μm thick electrodes possess low ionic resistance even without the use of macro-pores, causing the differences between the two electrode types to be nearly negligible. Since macro-pores provide a pathway for charge adsorption in parallel with direct transport through the electrode thickness (because their "currents" are additive), their impact on measured capacitance is expected to diminish for thin electrodes.

For the various electrode thicknesses tested, average capacitance was calculated per unit area and per unit mass of the electrodes. Here, the areal capacitance C of a single electrode (in mF/cm^2) was calculated as $C = 4 \int i dV / \left(\dot{V} \Delta V\right)$, where i, $\dot{V}$, and ΔV are current density, sweep rate, and the voltage window spanned, respectively. The current density is normalized to the projected area of the circular electrode's top surface, not taking into account surface area exposed by the addition of macro-pores. The "4" factor is included to account for two electrodes in series, making the capacitance of one electrode twice that of the cell, and the mass of that anode or cathode is half that of the total material present [64].

Figures 2-2A and 2-2B show the average capacitance as a function of sweep rate for the various thicknesses tested in both unpatterned and bi-tortuous forms. The capacitance of thicker electrodes is more sensitive to sweep rate than thin ones. Also, for a given electrode thickness the

bi-tortuous electrodes are generally less sensitive to sweep rate than unpatterned ones. The difference in rate-sensitivity between the two types of electrodes increases with thickness. This sensitivity causes the difference between the two electrode types to increase with both sweep rate and thickness, as shown in Fig. 2-2C. The improvement of the thinnest electrode is negligible and does not outweigh the effect of mass loss, while the thickest bi-tortuous electrodes can reach over twice the areal capacitance of unpatterned electrodes over the tested range.

The observed trends can be explained by considering the scaling of electrode resistance and theoretical capacitance with electrode thickness. As shown in Figs. 2-1E and 2-1F, the measured instantaneous capacitance develops transiently to its maximum value after a certain time-scale. When electrode thickness increases this transient time scale also increases due to the dependence of resistance and capacitance on thickness. This effect reduces the measured specific capacitance of thicker electrodes at high sweep rates.

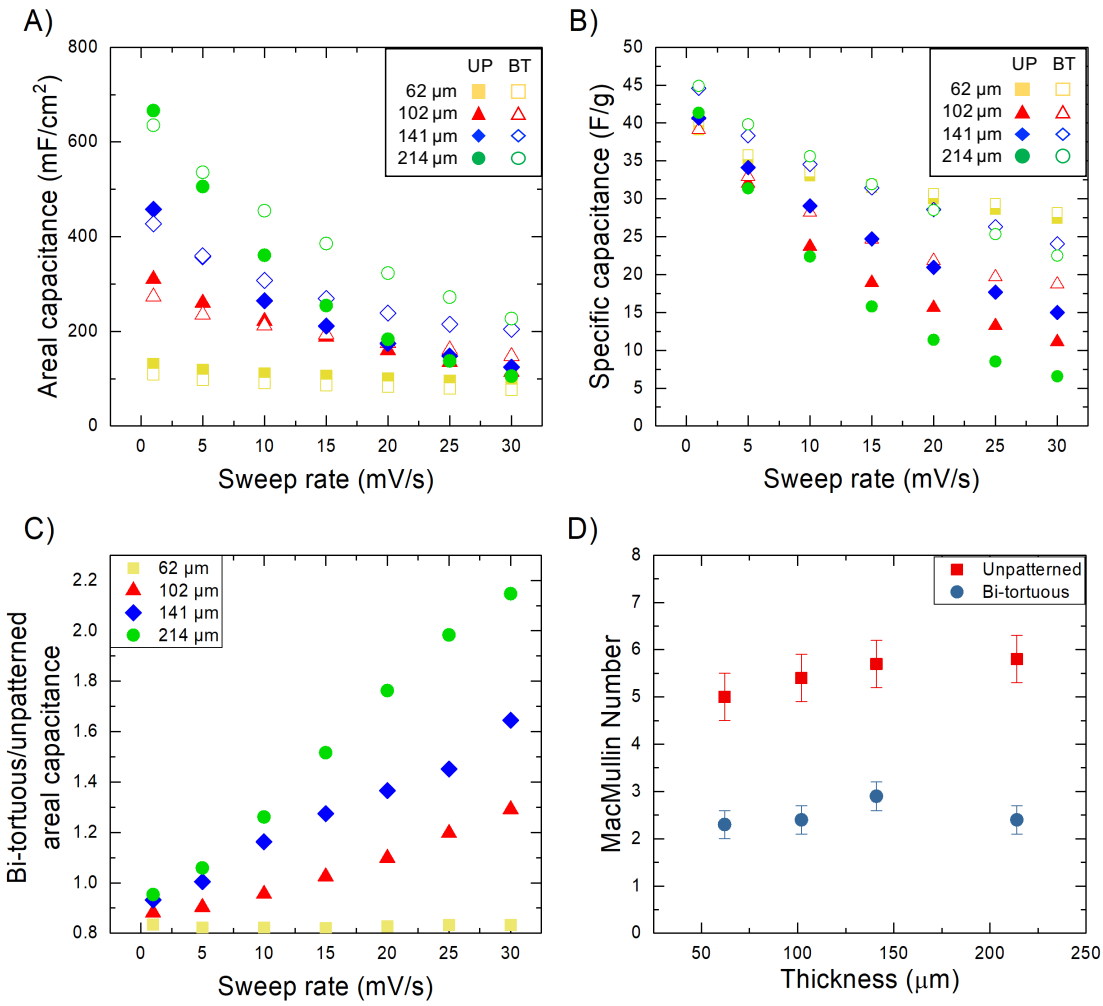

Figure 2-2. A) Areal capacitance data for unpatterned and bi-tortuous electrodes of varying thickness, showing the difference in the rate of change across the sweep rates for the two electrode types. B) Specific capacitance data from the same experiments. C) Ratios between the areal capacitance of bi-tortuous and unpatterned electrodes for the four thicknesses. D) MacMullin numbers for the unpatterned and bi-tortuous electrodes determined from EIS, discussed in section 2-7. Error bars span the difference between the maximum and minimum of the four points measured.

The areal capacitance of the two electrode types can be distinguished by examining Fig. 2-2C, which shows the ratio of bi-tortuous to unpatterned areal capacitance for the cases presented in Figs. 2-2A and 2-2B. Although the values for specific capacitance in Fig. 2-2B are higher for

all bi-tortuous cases, areal capacitance is less at lower sweep rates due to their reduced post-milling mass. However, bi-tortuous electrodes stop showing lower areal capacitance as sweep rate rises because macro-pores reduce the effective resistance of the electrode, giving ions a more direct path to the EDL and reducing the transient current time-scale. For a thick electrode, such as 214 μm, four-fold higher resistance and areal capacitance are theoretically expected compared to the 62 μm electrode, making the effect of macro-pores more pronounced as they expose paths to capacitive material deeper in the electrode and decrease the time needed to reach the maximum current. As the capacitance of bi-tortuous electrodes was shown to exceed that of unpatterned ones under certain conditions, the tortuosity of both electrode types was subsequently characterized.

2-7 Tortuosity characterization using electrochemical impedance spectroscopy

EIS was used to characterize tortuosity of both electrode types by fitting impedance data to the predictions of a transmission line model (TLM) using MATLAB. EIS experiments were performed both for the four electrode thicknesses previously discussed, and then across five different salt concentrations. Nyquist plots for the 108 μm thick bi-tortuous and unpatterned electrodes are shown in Figs. 2-3A and 2-3B. Two effects are apparent from these plots: (1) EDL capacitance increases with salt concentration, resulting in a reduced imaginary impedance at higher concentrations, (2) as salt concentration increases ionic conductivity increases and consequently reduces real impedance, and (3) the decrease in tortuosity from unpatterned to bi-tortuous structures decreases the magnitude of the real impedance. As the frequency of the EIS tests increases, the value for impedance converges near that of an equivalent circuit consisting of the ionic and electronic resistors in parallel with each other and, hence, can be used to extract the tortuosity from EIS spectra.

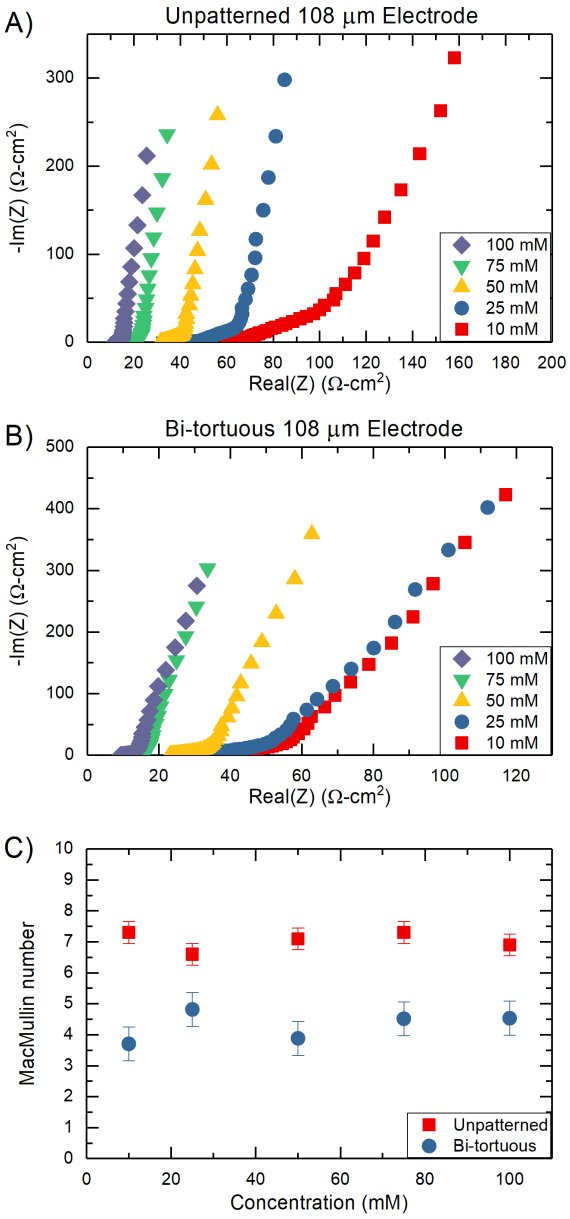

Figure 2-3. Nyquist plots from EIS experiment for A) unpatterned and B) bi-tortuous electrodes with NaCl electrolyte ranging in concentration from 10 to 100 mM. C) MacMullin numbers for the bi-tortuous electrodes compared to the unpatterned electrodes over all five tested concentrations. Error bars span the difference between the maximum and minimum of the five points measured.

The above effects can be explained by determining tortuosity with the aid of the TLM described hereafter. The TLM represents a porous electrode as a continuous system of ionic resistors, capacitors, and electronic resistors with corresponding impedance parameters Z_i, Z_t, and

Z_e, respectively. The ionic impedance Z_i depends on tortuosity τ as $Z_i = \frac{\tau}{\varepsilon} \cdot \frac{t}{\kappa_0 A}$ with electrode thickness t, projected area A, and bulk ionic conductivity κ_0. Values for κ_0 used in the fitting were found from linear interpolation of tabulated values for the ionic conductivity of aqueous NaCl, rather than the approximation for dilute solutions [63]. The capacitive impedance Z_t is defined as $Z_t = \frac{1}{(i\omega)^\gamma C}$ with frequency ω, constant-phase exponent γ (accounting for non-ideal response such as variations in dielectric constant [65,66]), and theoretical maximum capacitance C. Among the various datasets tested the fitted γ values varied between 0.92 and 0.99, with unity for an ideal capacitor. The electronic impedance Z_e is defined as $Z_e = \frac{t}{\sigma_{s,eff} A}$ with effective electronic conductivity $\sigma_{s,eff}$ measured to be 0.72 S/m based on the dry resistance of the electrode. The total electrode impedance for the TLM is given by [14]:

$$Z_{el} = \frac{1}{\frac{1}{Z_i} + \frac{1}{Z_e}} \left(1 + \frac{2 + \left(\frac{Z_e}{Z_i} + \frac{Z_i}{Z_e}\right) cosh\left(\sqrt{\frac{Z_e + Z_i}{Z_t}}\right)}{\sqrt{\frac{Z_e + Z_i}{Z_t}} sinh\left(\sqrt{\frac{Z_e + Z_i}{Z_t}}\right)} \right) \qquad (2-1)$$

The measured impedance for full-cell EIS tests Z_{cell} includes contributions from current collectors Z_{CC}, the separator Z_{sep}, and each electrode Z_{el}. These impedances were assumed to be in series, in which case Z_{cell} is expressed as $Z_{cell} = Z_{CC} + Z_{sep} + 2 \cdot Z_{el}$. Separator impedance was calculated from the 25 μm thickness of the Celgard 3501 membrane, bulk ionic conductivity, projected area, a porosity of 0.55 per manufacturer specifications, and a tortuosity of 2.8 measured independently by EIS. This separator's tortuosity is notably similar to previous measurements on Celgard 3500 (3.4±0.1 from Ref. [14]). Current collector impedance was a fitting parameter in all measurements.

Tortuosity values determined by fitting the TLM to EIS spectra for both electrode types are shown in Fig. 2-2D for various electrode thicknesses with 100 mM NaCl and in Fig. 2-3C for various salt concentrations with 108 μm thick electrodes. From Fig. 2-2D the patterning process is observed to reduce tortuosity by as much as 49% across the tested electrode thicknesses, with an average tortuosity reduction of 39%. This finding indicates that tortuosity is practically independent of salt concentration, a principle that is often assumed in porous media models. Capacitive electrodes possess a plurality of pore sizes, the largest of which facilitate ion conduction (both meso-pores between activated carbon particles and macro-pores machined into the electrodes) and the smallest of which store charge (micro-pores within activated carbon particles). Variations in salt concentration will change the size of the EDL and hence the distribution of pores over which ion conduction and charge storage take place. To quantify the likelihood of such effects, the Debye length was calculated, which at the tested concentrations is 1-5 nm, orders of magnitude smaller than the 100 μm macro-pores and ~10 μm meso-pores. Hence, the observed independence of tortuosity with salt concentration is consistent with theoretical expectations.

To enable the future design of bi-tortuous electrodes a simple analytical formula was constructed using a parallel resistance circuit. For microstructures with isotropic and monodisperse tortuosity the MacMullin number Mc is often estimated using the Bruggeman relation. This relation treats Mc as a function of porosity alone, $Mc = \tau/\varepsilon = \varepsilon^{-(1+\alpha)}$, where α is the Bruggeman exponent with a value of 0.5 for spheres or other empirically-found values [15,37]. The higher the porosity of a material, the less tortuous it is. In the case of bi-tortuous electrodes, the removal of material to produce macro-pores makes the tortuosity no longer solely dependent on the local porosity within meso-pores (i.e., of the unpatterned region of a bi-tortuous electrode),

as results in Fig. 2-2D and 2-3C show. The electrodes have similar microstructural tortuosity, but their tortuosity can be reduced by as much as 50% due to the addition of macro-pores.

As depicted in the inset of Fig. 2-4 model the bi-tortuous structure was modeled as a periodic circuit with parallel resistance components due to macro-pores and the mesoporous regions of the electrode. Using this approach the following expression for the MacMullin number of the entire structure is obtained:

$$Mc = \frac{Mc_{meso}}{(Mc_{meso}-1)\cdot\varepsilon_{macro}+1} \qquad (2-2)$$

Here, the local MacMullin number of the mesoporous region is Mc_{meso} and the macro-pore coverage is ε_{macro}. Figure 2-4 shows that this equation produces Mc values that decrease from Mc_{meso} and approach unity with increasing macro-pore coverage. To corroborate the predicted values an additional EIS experiment was conducted with the same parameters using 12.5% macro-pore coverage, the results of which are shown in Fig. 2-4. The value for this intermediate coverage was expected and found to be between those of the electrodes used in other experiments, validating the effect of increasing coverage lowering the tortuosity.

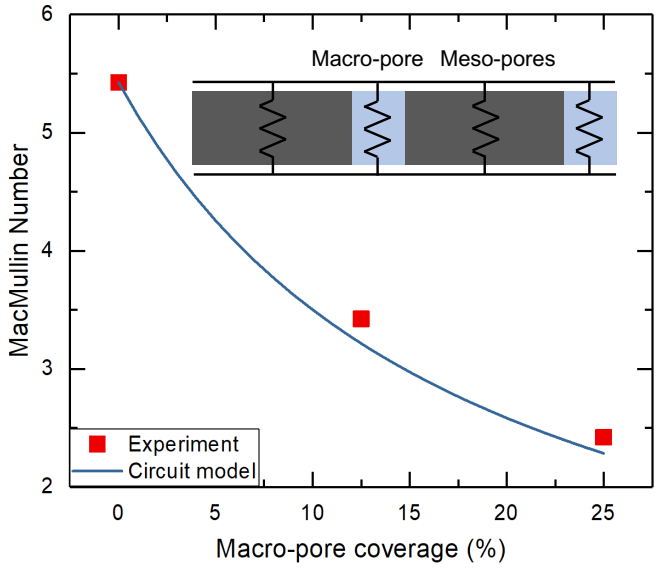

Figure 2-4. MacMullin numbers of a 118 µm thick electrode in 100 mM electrolyte with varying macro-pore coverage, showing the decline of the number as more macro-pores are added to the electrode. The solid curve was obtained with the circuit model described in the text.

2-8 Electrolyte current distribution simulations

Simulations of bi-tortuous electrodes were performed to understand the impact of bi-tortuosity on local transport and ion adsorption processes. Simulation parameters were selected to replicated experimental conditions as closely as possible, including theoretical capacitance, solution molarity, and the MacMullin number of mesoporous regions of the electrodes. The MacMullin number of the mesoporous region was set to 5.5, the average value measured for electrodes of different thickness. Within the macro-pores, which are, by definition, regions with no electrode material, the MacMullin number becomes equal to unity, as the ions can move in straight paths without intersecting the solid phase, and the entire region contains only the solution phase, making it completely porous.

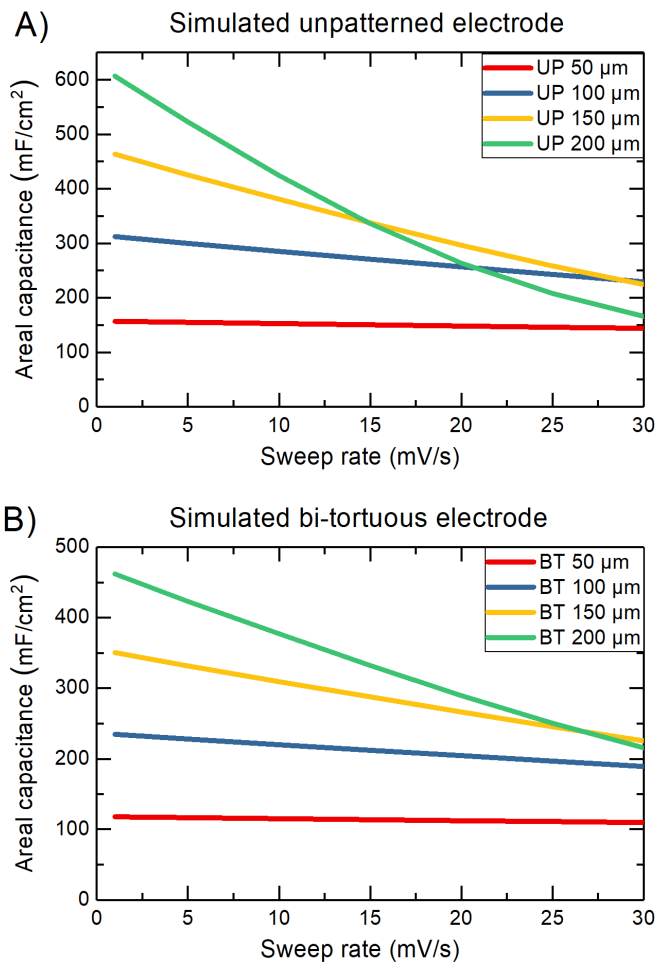

Figure 2-5. Simulated areal capacitance values of A) unpatterned and B) bi-tortuous electrodes, showing slower decline in capacitance for the bi-tortuous electrodes versus the unpatterned cases.

The results of these simulations are shown in Fig. 2-5, in which the values of capacitance in simulations and their trends with sweep rate agree with the experimentally observed trends. Figure 2-6A shows the ratio of areal capacitance for the two electrode types. Bi-tortuous electrodes display an improvement over the unpatterned cases at higher sweep rates, and the improvement becomes more significant with increasing thickness. Agreement between experimental and simulated trends includes the effect that bi-tortuous electrodes surpass the areal capacitance of their unpatterned equivalents as sweep rate increases, as seen in Fig. 2-6A. The results of

simulations show areal capacitance in a similar range as experiment on the order of hundreds of mF/cm^2, dependent on the simulated electrode thickness [67].

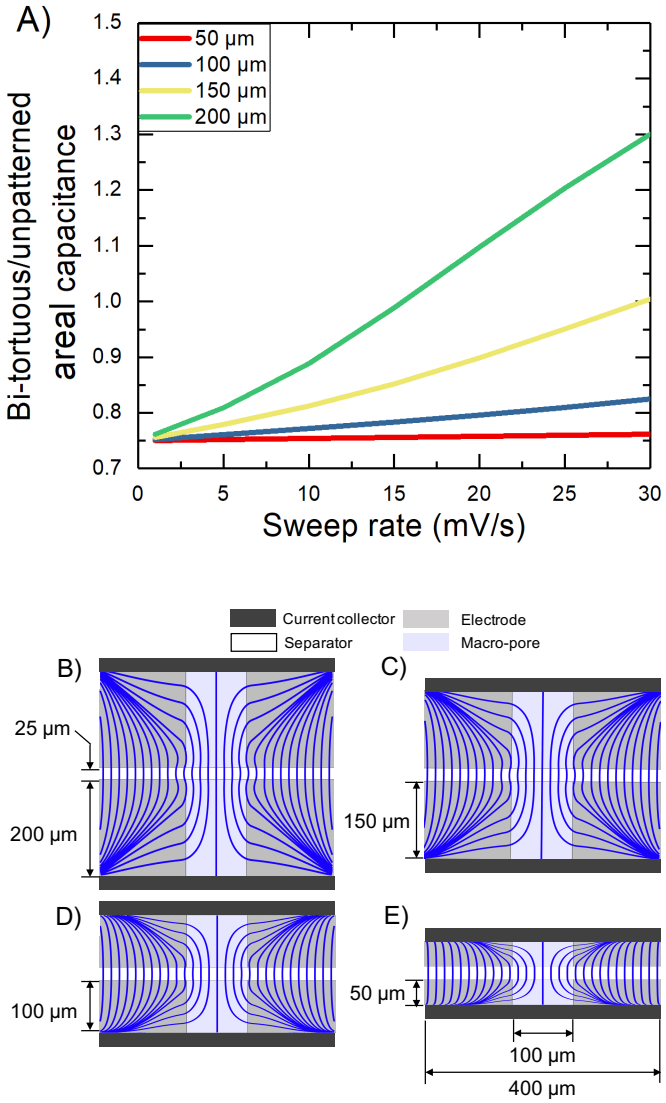

Figure 2-6. A) Ratios of areal capacitance between simulated bi-tortuous and unpatterned electrodes. Initially, this ratio is slightly greater than 0.75 for all thicknesses due to the reduction of mass caused by 25% macro-pore coverage, then the ratio increases with sweep rate. B-E) Plots of ionic current path lines in a simulated electrode at the final time step for cycling at 30 mV/s. The simulated anode and cathode correspond to the curves in 6A, and are 200, 150, 100, and 50 µm thick, shown to scale, with a 25 µm separator between the two. As thickness increases, the paths of the current increasingly diverge from the perfectly vertical lines expected for an unpatterned electrode.

Comparison of Fig. 2-2C and Fig. 2-6A shows the improvement that comes from patterning is more significant in experiments than in simulations. Additionally, both types of simulated electrodes showed a slower decline with sweep rate in capacitance compared to experimentally found values. A factor that could account for faster decline in experiments, in part, is the experimental electrical contact resistance that the simulation does not take into account. Another explanation is the overestimation of porosity of the microstructure and the equivalent conductance, and by extension effective ionic conductivity. Isotropic tortuosity is assumed, though there may be anisotropy due to the directionality of the drying process. By including porous space inside the capacitive particles through which ions do not flow, the simulated electrodes have a lower MacMullin number than in experiments.

As a result of the addition of macro-pores, the simulated electrodes showed a slower decline in capacitance compared to the unpatterned cases. However, due to the loss of 25% of the mass of active material in bi-tortuous electrodes when adding the macro-pores, the areal capacitances of the bi-tortuous electrodes were lower than the unpatterned cases at lower sweep rates, as in the experiments. The ratio of the capacitances for the bi-tortuous and unpatterned electrodes initially started between 0.75 and 0.8, and increased at a rate dependent on the electrode thickness. These results from the simulations agree with the experimentally-found trends in capacitance with respect to sweep rate, as shown in Fig. 2-6A. As the thicker electrodes possessed higher resistances and benefitted most from the macro-pores, the bi-tortuous electrodes outperformed the unpatterned ones more easily, overtaking them in performance at lower sweep rates as thickness increased, as shown in Fig. 2-6A.

The current lines in Figs. 2-6B through 2-6E display the paths of ions moving through the electrolyte from one boundary of the domain to another, analogous to streamlines in fluid

dynamics. These curves were calculated using simulated outputs of concentration and electrostatic potential at each cell in the solution phase to calculate the components of current density in the in-plane and thru-plane directions, giving the vector for the ionic current density, $\vec{\imath}$:

$$\vec{\imath} = -\kappa_{eff}\left(\nabla\phi_{ES} - R_g T/F\,(2(1 - t_+) - 1)\nabla ln(c_e)\right) \qquad (2-3)$$

This expression is noted to use electrostatic potential rather than solution-phase potential (or reduced electrochemical potential of cations) that is commonly used in Li-ion batteries [16,33,57]. The calculated paths show the effect of macro-pores with increasing thickness: for the 50 μm electrodes in Fig. 2-6E, there are regions at the sides where the current density is aligned in the thru-plane direction. As the thickness of electrodes increases, the region affected by the macro-pore expands across more of the width and the thickness of the electrode. Another result of the effective resistance of the different regions is that, due to the higher resistance in the electrode compared to the macro-pore, at the boundary between them and the separator current flows around the electrode rather than through it. This effect can be seen in the current path lines near the center of the cell (Fig. 2-6B). As thickness and sweep rate increase, the paths of ionic current depart from the vertical orientation of unpatterned electrodes to a greater degree. Ions travel through the macro-pore and are adsorbed into the EDL of the electrode particles closer to the current collector, making use of more capacitive material.

2-9 Conclusions

Cyclic voltammetry and electrochemical impedance spectroscopy tests were performed on unpatterned and bi-tortuous electrodes of four different thicknesses, showing greater specific capacitance and rate capability for bi-tortuous electrodes. While the bi-tortuous electrodes showed

higher capacitance per unit mass in all cases, the total capacitance of unpatterned electrodes can remain higher when the sweep rate is low due to the presence of more capacitive material. In order to reap the benefits of these electrodes, it is best for them to function at high cycling rates.

Tortuosity values for electrodes immersed in electrolytes of varying concentrations were found, and they remained in a consistent range regardless of salt molarity, as expected from the tortuosity's sole dependence on electrode microstructure. For the unpatterned cases, the MacMullin number was, on average, 6.75 during experiments for varying thickness and 8.16 in the experiments at a single thickness with varying salt concentration. The addition of macro-pores reduced the MacMullin number to 2.95 when varying thickness and 4.98 when varying concentration, showing a reduction in tortuosity of between 40 and 60%.

Though the bi-tortuous electrodes show improved performance and rate capability over the unpatterned electrodes, these electrodes have not been yet tested in a real desalination device. The results of these experiments are encouraging and show the possibility of producing more conductive and capacitive carbon electrodes.

CHAPTER 3: EFFECTS OF CONSTITUENT PARTICLES ON ELECTRODE TRANSPORT PROPERTIES

3-1 Porous electrode structure

The finite ionic conductivity of porous electrodes in FDI cells leads to ohmic polarization and, consequently, irreversible energy consumption. The MacMullin number Mc, the ratio between the bulk ionic conductivity of the electrolyte κ_0 and its effective value κ_{eff}, is determined by the size, distribution, and topology of electrode pores. Previous research has found MacMullin number to depend on electrode porosity ε and particle shape, as these factors determine the number and length of paths available for ions to travel through the electrode [15,68]. The scaling of Mc with ε is generally nonlinear due to the combined effects of decreased throat-size of pores and the increasingly tortuous path along which ions travel when porosity decreases. These effects are captured by the Bruggeman relation $Mc = 1/\varepsilon^{1.5}$ [39,41], which is valid only for certain microstructures with spherical particles. Electrodes composed of non-spherical particles can have MacMullin number and porosity related by the function $Mc = 1/\varepsilon^{\alpha}$, where α is the Bruggeman exponent [15]. To circumvent this scaling, in Chapter 1 macroscopic pores were milled into microporous CDI electrodes to enhance ionic conduction and reduce charging times shown in Chapter 1, and such electrodes showed lower impedance, higher adsorption rate, and higher adsorption capacity than unmilled electrodes [69]. In this chapter the tradeoffs between Mc, σ_{eff}, and k_h were measured for various electrode processing conditions to maximize salt removal rate in FDI.

In capacitive deionization using EDLs performance has been quantified by relating specific energy consumption (SEC), defined as the energy required to remove one mole of salt, to the average salt adsorption rate (ASAR), defined as the average rate of salt removal per unit area of

the electrode. Due to decreasing ionic conductivity of effluent and re-salination time between adsorption and desorption steps, the faster salt is removed in CDI, the more energy is required [70,71]. Thus, CDI research has been motivated to increase ASAR without increasing SEC. Another method of quantifying performance is the Kim-Yoon (or CDI Ragone) plot, which compares deionization capacity to salt removal rate [72]. In contrast to these approaches wherein tradeoffs in performance metrics are quantified for a discrete set of materials, the *inverse problem* can be posed wherein a space of material properties is defined with corresponding performance contours. While such analyses have typically been relegated to mechanical problems using Ashby diagrams [73], electrochemical materials-selection maps have been constructed for redox flow batteries to minimize power losses due to ohmic resistance [74,75] and electrolyte cost [74]. Here, a materials selection problem is posed for flow-through FDI electrodes in the three-dimensional σ_{eff}-κ_{eff}-k_h space to maximize ASAR for fixed SEC.

While intercalation materials possess high capacity in comparison with activated carbons typically used in conventional capacitive deionization (CDI) [6,76], intercalation materials often suffer from low electronic conductivity causing high energy consumption and slow charge times. Recent work has also revealed the importance of balancing electron transport in solid electrodes [33,77] and ion transport in electrode pores [10,33,61,78,79] to facilitate desalination with high charge and energy efficiencies. Accordingly, efforts to overcome electronic conduction limitations have bonded $Na_3V_2(PO_4)_3$ nanowires with carbon [80], coated carbon onto $NaTi_2(PO_4)_3$ nanoparticles [81], supported TiS_2 nanoparticles on carbon nanotubes [82], and combined $NaTi_2(PO_4)_3$ [83] and $FePO_4$ [84] nanoparticles with reduced graphene oxide. In this work porous electrodes comprised of insulative particles and carbon blacks of various average radii to assess

the tradeoffs in their transport properties with loading, including effective electronic conductivity σ_{eff}.

The effect of calendering electrodes to increase electronic conductivity and volumetric charge storage was explored by increasing the density of active particles and the solid fraction of the porous structure [85]. Despite being a common practice in Li-ion battery manufacturing, calendering has downsides which can outweigh the expected improvements, such as reducing effective ionic conductivity [15], electroactive surface area [86], and electrolyte infiltration [87]. The change in electronic conductivity with calendering also depends on the initial mass fraction of carbon black, as even if the average volume fractions are similar due to the calendering of a low-carbon electrode, the conductivity will differ [88]. Thus, σ_{eff} was measured for various degrees of calendering and as a function of the size and loading of conductive and insulative particles.

In this chapter, reprinting Ref. [89] with permission from Water Research, the influence of conductive additives on the electronic conductivity, ionic conductivity, and hydraulic permeability of porous electrodes incorporating insulative particles. To study the effects of electrode composition and particle size, transport properties were measured for porous electrodes consisting of two insulative powders of different particle size and two carbon blacks with different specific surface areas. Alumina was selected as a "pseudo-active" surrogate material for insulative active particles because of its low conductivity and abundance, the use of which was ultimately validated by creating porous electrodes containing NiHCF PBA with an optimized electrode formulation. The varying sizes of particles are shown to influence how ions and fluid moved through the electrode microstructure.

3-2 Electrode preparation

Alumina (Al_2O_3) particles were used as a "pseudo-active" material in place of insulative intercalation particles with two different diameters: 1 μm (AdValue Technology) and 40 nm (SkySpring Nanomaterials, Inc.). Two different types of carbon black were combined with alumina to assess the impact of size and morphology on transport properties: C45 (MTI XTL) and Ketjen black EC-600JD (KB, Akzo Nobel). These two carbons show order of magnitude difference in specific surface area and particle radii: 960 nm, 45 m^2/g particles for C45 compared to 34 nm, 1270 m^2/g for KB. The various electrode slurries were prepared by mixing alumina and carbon black (CB) with alumina:CB mass ratios from 95:0 to 87.5:7.5, each with a 5 wt.% PVDF in all cases. It should be noted that previous CDI studies have used activated carbon electrodes with binder loading levels of approximately 10 wt.% [48,90,91]. The mass loading of binder was reduced here to produce a similar volume fraction to previous CDI experiments by accounting for alumina's two-fold higher density than carbon (3.95 g/cm^3 versus ~2 g/cm^3). Powder mixtures were dispersed in NMP solvent and mixed in a Thinky ARE-310 planetary mixer for 25 minutes, followed by 5 minutes of deaeration to remove air bubbles. The most significant source of experimental uncertainty in the transport property measurements was electrode thickness. Although the Elcometer film applicator can cast electrode slurry with an accuracy of microns, electrodes were observed to shrink to approximately half of their initial thickness after wet phase inversion and subsequent drying. An uncertainty of 5 μm in electrode thickness measurement (MTI thickness gauge) was assumed to create the error bars shown in all figures for the values of conductivity, MacMullin number, permeability, porosity, and carbon black volume fraction.

Due to electrode slurries containing nanoparticles being more viscous than slurries of microparticles, a larger amount of NMP was used during mixing to cast such slurries. For 1 μm

diameter alumina particles, only 1 mL of solvent was needed for each gram of the solid powder mixture, while 1.5 mL/g was needed to produce a castable slurry for 40 nm particles. After thorough mixing slurries were cast using an Elcometer film applicator onto either conducting (graphite foil, Ceramaterials) or non-conducting (PTFE, AST Industries, Inc.) substrates. Experiments measuring electronic and ionic conductivity used PTFE substrates to prevent the substrate from interfering with the measurements because PTFE has a conductivity of ~10^{-14} S/m. Measurements of hydraulic permeability were performed on electrodes supported on graphite foil to stabilize samples and to enable their precise arrangement in the testing apparatus. Once cast at a desired thickness level, the electrode and substrate were immersed in deionized water to remove NMP solvent by a wet-phase inversion process [48]. Solidified electrodes were then air-dried at room temperature for two hours to remove residual NMP. Electrodes were re-immersed in either deionized water or 100 mM aqueous NaCl for twelve hours prior to testing to enable thorough wetting and to remove air bubbles.

3-3. Electronic and ionic conductivity measurements

Electronic conductivity of the electrodes was measured using an inhouse-built four-point probe with gold-coated 0.5 mm diameter pins spaced 2 mm apart to contact electrodes. The small thickness of samples (~100 μm) compared to the probe spacing (2 mm) makes the thin-film approximation valid. Once dried, the electrodes were wetted in 100 mM aqueous NaCl for twelve hours to remove any air bubbles. A four-point probe method was used to measure effective electronic and ionic conductivity, the details of which are described in the Electronic Supplementary Material (ESM). Measured current between source probes $I(t)$ (A) was fitted to a

stretched exponential function with stretching factor β, as in a previous study of EDL formation and dissipation [92]:

$$I(t) = I_i e^{-\left(\frac{t}{\tau}\right)^{\beta}} + I_e \quad (3-1)$$

Fits showed an average error of 5% at most and <1% in the best cases when compared to experimental data. In the context of these experiments the initial I_i and final I_f currents are most important because ionic and electronic conductivity can be determined directly using their values. As charge builds up in the EDL on source probe tips, ionic current declines until current can only move through the solid matrix. The slope of the upper envelope of current versus potential in Fig. 3-2B is proportional to the sum of effective electronic σ_{eff} (S/m) and ionic κ_{eff} (S/m) conductivity, while the slope of the lower envelope of current versus potential is proportional to effective electronic conductivity σ_{eff} [93]:

$$\sigma_{final} = \frac{\ln(2)}{\pi}\frac{I_e}{wV} = \sigma_{eff} \quad (3-2)$$

$$\sigma_{initial} = \frac{\ln(2)}{\pi}\frac{(I_i + I_e)}{wV} = \sigma_{eff} + \kappa_{eff} \quad (3-3)$$

Here, w (m) is the thickness of a given electrode and V (V) is the potential difference between the inner leads of the apparatus. MacMullin number Mc was subsequently calculated as:

$$Mc = \frac{\kappa_0}{\kappa_{eff}}, \quad (3-4)$$

where κ_0 is the ionic conductivity of 100 mM aqueous NaCl at 298 K (1.067 S/m [63]).

In previous literature studying the tortuosity of porous electrodes and the work in Chapter 1, electrochemical impedance spectroscopy was used to determine the effective ionic conductivity by fitting real and imaginary impedance values to a transmission-line model [14,15,94]. For the present electrode samples this method was found to be impractical due to their low electric double-

layer (EDL) capacitance and high resistance. Measurements were thus performed with a method similar to the four-point or four-line probe technique [95,96]. This method approximates each sample as a semi-infinite medium upon the surface of which four probes are spaced co-linearly at a finite interval. The difference in voltage between the two interior probes ("sense" probes) is then measured while current is applied between the two external probes ("source" probes).

Unlike typical application of the four-point probe method, which measure the conductivity of a single phase, performing measurements on wetted electrodes allows measurement of the effective electronic conductivity of the solid electrode as well as effective ionic conductivity of electrolyte permeating the porous microstructure. The surface of the probe tips, when in contact with the electrolyte, function as a double-layer capacitor. Fig. 231 shows the transmission line model of a porous electrode, which can be simplified to a circuit consisting of one electronic resistor, one ionic resistor, and the probe capacitance. To prevent evaporation during experiments, the electrodes were covered with a layer of Parafilm (Bemis), and excess electrolyte was pressed out to ensure that the probes were only measuring conductivity of electrolyte within the electrode's porous structure. In typical uses of the four-point probe technique, current is the control variable and the potential difference across sense probes is measured to infer electronic conductivity. In the present application all probes were in contact with aqueous solution at near-neutral pH. To reduce the risk of water electrolysis the potential difference across sense leads was set to values ranging from 0.1-0.5 V at 0.1 V intervals by adjusting the current applied through source leads. As is shown subsequently, controlling potential also simplifies the analysis of measured data.

To apply four-point probe theory to measure the electronic/ionic conductivity of the present mixed-conducting samples requires that capacitive charging at porous electrode/solution interfaces is negligible in comparison with probe charging. The specific surface area and capacitance of

alumina particles, while low in comparison to active particles used in supercapacitors, is orders of magnitude higher than that of a metal probe's surface. In theory the effect of porous electrode capacitance could be described using a transmission-line model in Fig. 3-1. Accordingly, the simplified parallel circuit model used to derive Eqs. 3-1 and 3-3 was validated by including an additional lumped-capacitive element for porous electrode capacitance. The resulting current response approached that of the simplified circuit when the ratio of probe capacitance to particle capacitance approached zero, thus supporting use of the simplified circuit.

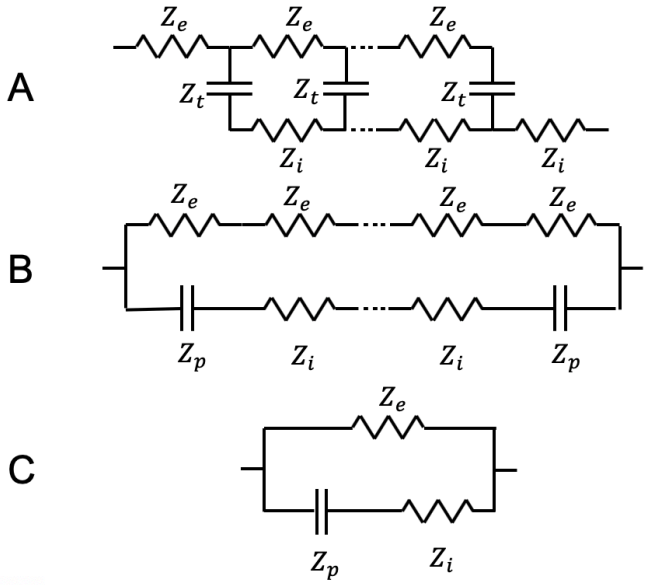

Figure 3-1: Circuit model of the system being measured by the four-point probe. A) The transmission line model of the electrode, consisting of electronic resistors, ionic resistors, and capacitors. B) The transmission line model when in contact with the probes via solid-solid and solid-liquid interfaces forms a different circuit, including the probe surface capacitance represented by Z_p. At the time scales of the experiments, the capacitance of the electrode particles Z_t can be ignored. C) These simplifications reduce the circuit to a simple model of two resistors and one capacitor.

A four-point probe device was designed and fabricated using four gold-coated pins and a 3D-printed stand to position them, shown in Figure 3-2C. A VMP-3 multi-channel potentiostat (Bio-logic) was used to apply current and measure potential using this device. This approach was

adopted because of the unique features of the samples tested, including the use of potential control to reduce the chance of electrolysis, the presence of both electrolyte and solid conductor, and the use of transient current measurements.

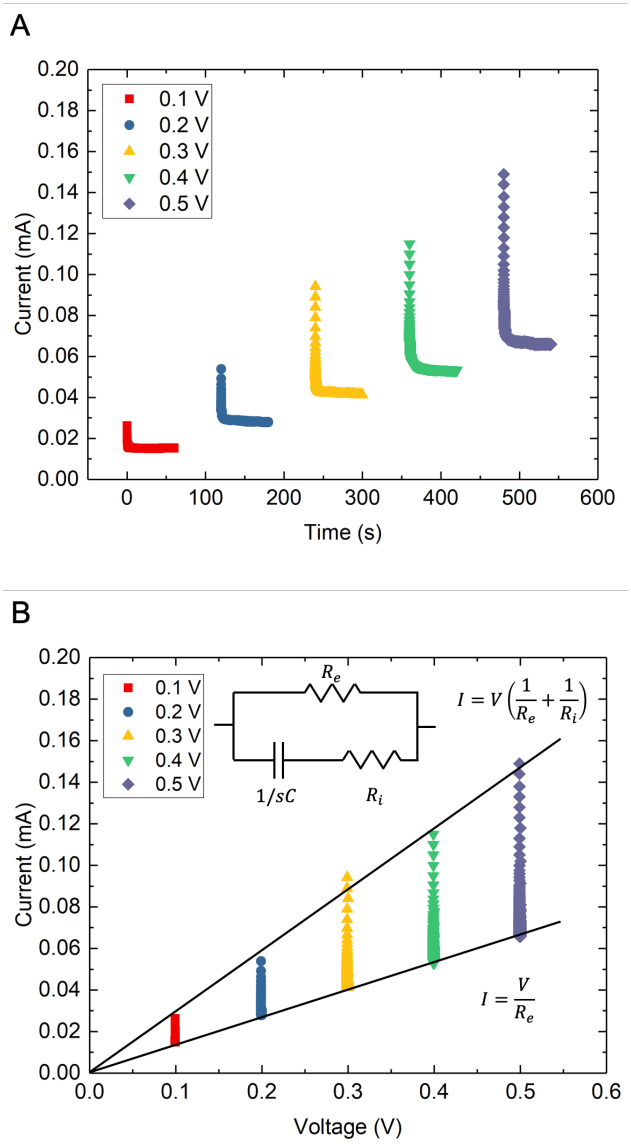

Figure 3-2

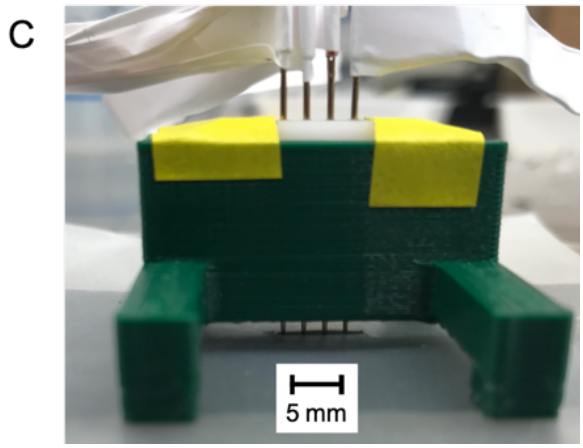

Figure 3-2 (cont.): Amperometry data obtained from a four-probe apparatus for a representative electrode containing 2.5 wt.% Ketjen black with 92.5 wt.% alumina microparticles. A) Current versus time shows an exponential decline of the ionic contribution to current. Time between steps in potential was included to allow the samples to equilibrate. B) Current as a function of potential for the five potential steps. Initially, the applied potential difference induces a current with contributions from electrons in the solid phase and ions in the electrolyte, and the difference between these contributions was used to find the conductivities of their respective phases. C) The custom-made four-point probe used to perform the experiments, sitting atop a layer of parafilm protecting the electrode sample beneath.

3-4 Hydraulic permeability

To measure the hydraulic permeability of porous electrodes, 1.25 x 1.25 cm^2 samples were cut from electrodes cast onto graphite foil and placed into a 0.5 mm deep channel through which deionized water was driven by a small hydraulic head Δp (Pa) shown in Fig. 3-3. The samples were wrapped in PTFE tape to seal them and force solution flow exclusively through the porous electrode. Hydraulic head was maintained by a reservoir to ensure a consistent water level as fluid flowed. Water flowed through the electrode over a period of one hour, after which the average fluid flow was calculated from the collected water mass.

To account for the no-slip condition at the edges of the porous electrodes (as in other work on redox flow batteries [97]) the Darcy-Brinkman equation was solved analytically for the flow rate $\dot{V}$ (m^3/s) through a rectangular cross-section of thickness w, width d (m), and flow-path length

l (m). Due to the 1.25 cm distance d being two orders larger than the electrode thickness, lateral edge effects were ignored. The effective viscosity term has been shown by simulation to increase as porosity decreases [98,99]. Here, it is assumed that effective viscosity is inversely proportional to porosity, $\mu_{eff} = \mu/\varepsilon$ (Pa-s). In Eq. 3-5, as porosity decreases, the flow rate approaches zero.

$$\dot{V} = -\Delta p \frac{k_h}{\mu} \frac{wd}{l} \left(1 - \sqrt{\frac{4k_h}{w^2 \varepsilon}} \tanh\left(\sqrt{\frac{w^2 \varepsilon}{4k_h}} \right) \right) \qquad (3-5)$$

Permeability k_h (m^2) was calculated by solving Eq. 2-5 numerically with measured flow rate and porosity using MATLAB. Porosity ε is dependent on the loading of each solid, and it was calculated as $\varepsilon = 1 - \rho_{total}/\rho_{solid}$, where ρ_{total} (g/cm^3) is the average dry electrode density and ρ_{solid} is the mass-averaged density of the electrode constituents (carbon black, pseudo-actives, and PVDF). A schematic of the permeability measurement apparatus used here is shown in Figure 3-3. Per Eq. 3-5, as the thickness and depth of the electrode increase, the edge effects become less significant due to the factor $\sqrt{4k_h/w^2\varepsilon}$ becoming smaller. The permeability determined from Eq. 5 was approximately 5-10% higher than if edge effects had been neglected.

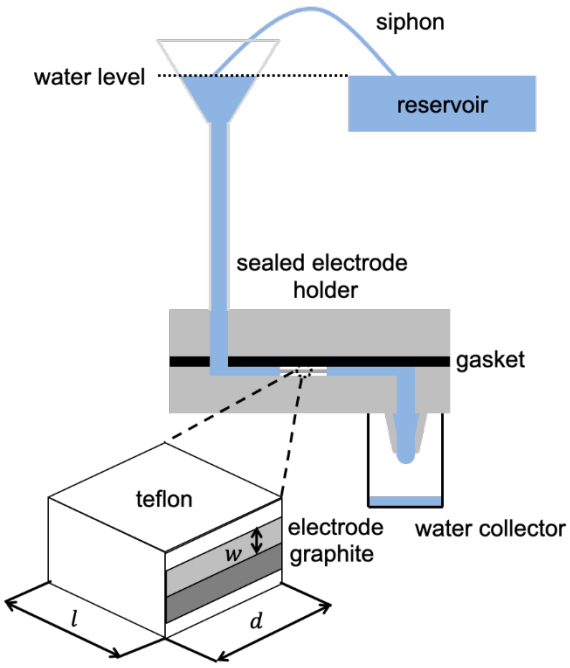

Figure 3-3: The experimental apparatus for measuring hydraulic permeability. A hydraulic head of 30 cm was applied to drive fluid through an electrode, and the volume of water which flowed through was used to find the flow rate and calculate permeability. Connecting the column of water to a reservoir via the siphon ensured that its height remained constant. Electrode samples of thickness w were cut into squares of $l = d$ =12.5 mm.

3-5 Electrode transport property results

Measurements of electronic conductivity, ionic conductivity, and hydraulic permeability were performed on electrodes combining different loading levels of carbon black and alumina powders with 5 wt.% PVDF content producing CB:alumina mass ratios equal to 0:95, 1:94, 2.5:92.5, 5:90, and 7.5:87.5. Electrodes containing greater quantities of carbon black were prone to cracking, even when cast at low thicknesses. Results are presented in terms of volume fraction, rather than mass fraction, to generalize these results to electrodes using active compounds with arbitrary mass density.

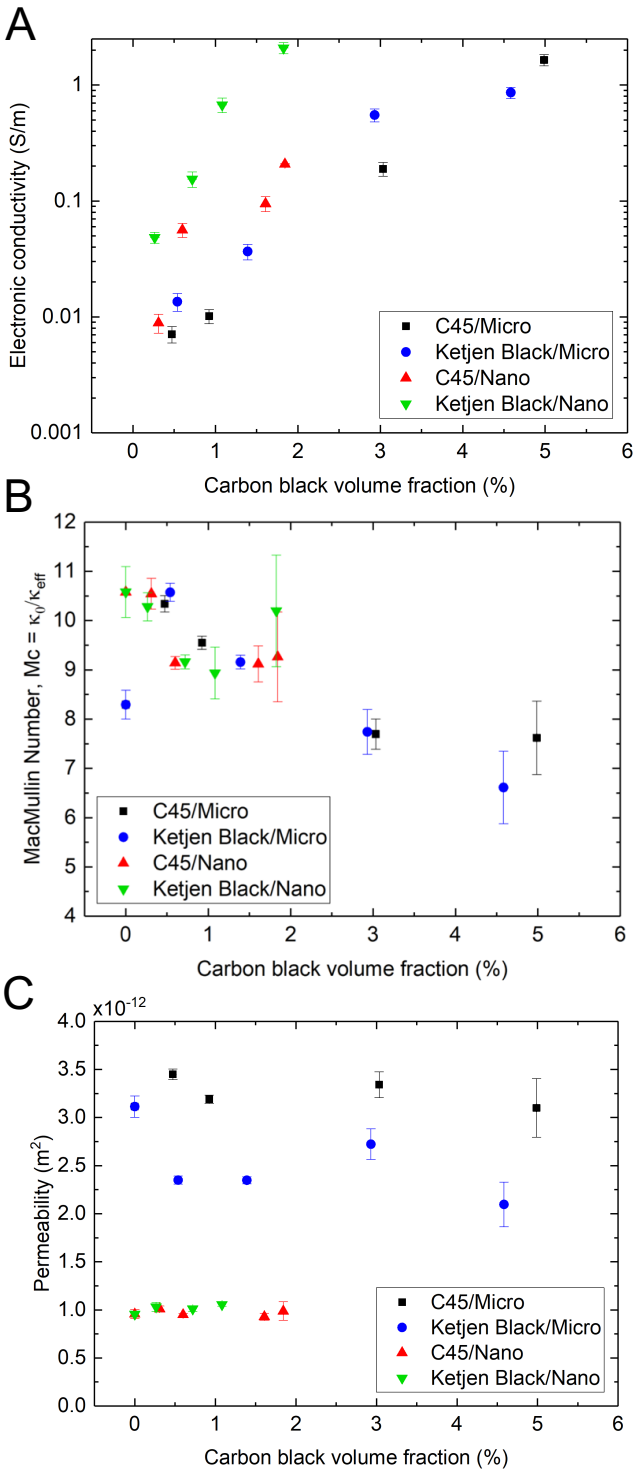

Figure 3-4: A) Electronic conductivity, B) MacMullin number, and C) permeability versus the carbon black volume fraction for the combinations of pseudo-active particle size and carbon black powders of interest.

Figure 3-4A shows effective electronic conductivity for the electrode samples tested. In addition to the previously-discussed error caused by variations in electrode thickness measurements, the possible presence of hydrogen evolution in the electrolyte required an additional 10% error. This is an overestimation of the error at higher conductivities, as the current produced by electrolysis would become less significant compared to electronic current as conductivity increases. The increasing volume fractions of carbon black in the case of electrodes using micro-scale pseudo-active and C45 particles show that additives do not significantly improve electronic conductivity until a certain threshold additive loading is reached. This effect is attributed to percolation of conductive additive networks that is required for electrons to access the high conductivity of carbon black at the macro-scale. In contrast, for electrodes comprised primarily of nano-scale pseudo-active and Ketjen black particles, a volume fraction of less than 0.5% Ketjen black caused an immediate increase in conductivity by an order of magnitude relative to an electrode without carbon black. These findings suggest that Ketjen black percolates more easily than C45, especially when nano-scale pseudo-active particles are mixed together with them. Electrodes with nano-scale pseudo-actives and Ketjen black consistently showed higher conductivity for similar carbon black loading, and Ketjen black proved superior to C45 at improving conductivity. Though higher electronic conductivity can be achieved at lower mass or volume fractions by using smaller pseudo-active particles, at higher loadings electronic conductivity saturates to 1-2 S/m. Furthermore, testing electrodes with higher carbon black loading was limited by electrode cracking. It should be noted that the porosities of the nanoparticulate electrodes were generally ~10% higher than the electrodes made with microparticles, resulting in a wider range of carbon black volume fractions despite identical mass fractions in the power mixture.

Electrode MacMullin number, which is an inverse measure of effective ionic conductivity normalized by bulk ionic conductivity, decreased with increasing volume fraction of carbon black, except when compared with the electrodes only containing pseudo-active particles (Fig. 3-4B). Thus, adding carbon black is observed to increase electronic conductivity also increases effective ionic conductivity. This trend contrasts with previous measurements of tortuosity for Li-ion battery electrodes with varying levels of conductive additives. This difference may be attributed to the fact that the pseudo-active particles used in the present work are less than 1 μm in diameter, compared to the spheroids and flakes with dimensions exceeding 5 μm [100]. Such large, anisometric particles are more likely to block more paths within pores and impede ion transport than the smaller isometric ones used here.

In addition to the electronic and ionic conductivities of electrodes, the hydraulic permeabilities of different electrode compositions are of interest for flow-through electrodes. From Fig. 3-4C is it observed that electrodes using C45 and Ketjen black with micro-scale pseudo-active particles possess different k_h. In contrast, for electrodes using nano-scale pseudo-active particles hydraulic permeability shows a much less varied range of values, remaining within 5% of each other. The lower permeability in the case of electrodes using nano-scale pseudo-active particles (relative to micron-scale particles) is attributed to the smaller pores produced by smaller particles. This effect is also noticeable when comparing electrodes made with Ketjen black and C45. When electrode particles pack together larger particles produce larger pores and higher permeability. Electrodes made using the micro-scale pseudo-active particles showed greater variation in permeability with carbon black content than electrodes made with nano-scale particles. Because pseudo-active nanoparticles and carbon black particles were similar in size, both being <50 nm, the addition of Ketjen black to those electrodes affected their average pore diameter to a

minimal extent. This conclusion is consistent with data showing smaller permeability for electrodes made with Ketjen black particles relative to those made with the larger C45 particles.

To validate use of alumina as an insulative pseudo-active compound, the transport properties of an electrode containing Prussian blue analogue (PBA) nanoparticles, carbon black, and PVDF were measured. The results are directly compared to those for electrodes using pseudo-active particles in Table 3-1. When PBA particles were combined with Ketjen black, the electronic conductivity of the PBA electrodes was fifty-fold larger than when combined with C45, while only a three-fold increase was observed in the case of the alumina. Permeability for the PBA and alumina electrodes was on the same order of magnitude, though the PBA electrodes were more resistant to flow. The MacMullin number of PBA/Ketjen black electrodes was 31% smaller than PBA/C45 electrodes, while the hydraulic permeability was 12% lower for PBA/Ketjen black. SEM images of the two PBA electrodes in Fig. 3-5 reveal that the electrode with Ketjen black appears significantly rougher than with C45. The C45 electrode has larger agglomerates and thus binder is spread over less area and obscures solid particles, while Ketjen black particles are visible and appear more distributed through the microstructure.

Table 3-1: Comparison of transport properties in PBA-containing electrodes consisting of approximately 10 wt% carbon black. PBA-containing electrodes were compared with alumina micro-scale electrodes composed of 5 wt.% carbon black to match their volumetric loading levels.

	Electronic conductivity (S/m)	MacMullin number (-)	Permeability (10^{-12} m^2)
PBA/C45	0.0067	10.47	1.45
PBA/Ketjen black	0.318	7.18	1.28
alumina/C45	0.189	7.69	3.34
alumina/Ketjen black	0.552	7.74	2.72

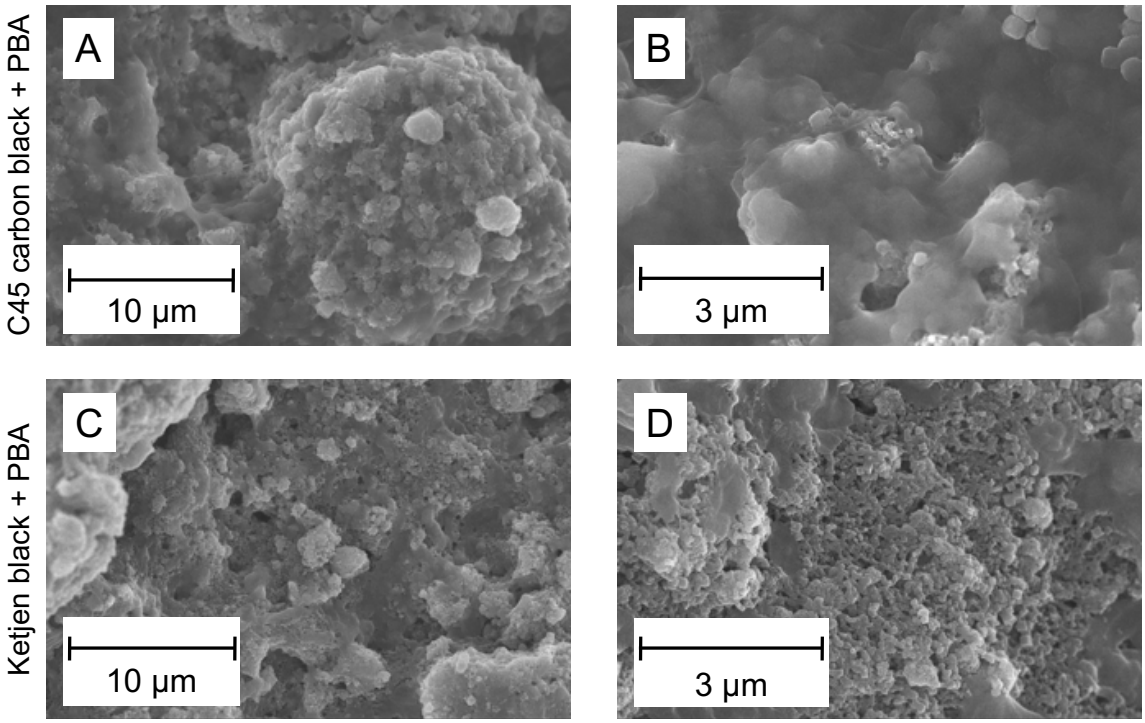

Figure 3-5: SEM images of PBA/C45 electrodes at A) 4,000x magnification and B) 15,000x magnification. Equivalent magnifications for PBA/Ketjen black electrodes are shown in C) and D).

3-6 Effects of calendering and binder content

In addition to the measurements of electronic and ionic conductivity of electrodes, a total of six electrode mixtures were tested using calendering. Three electrodes were calendered for each type of carbon black (Fig. 3-6): (i) 1 wt.% carbon black with micro-scale pseudo active particles, (ii) 1 wt.% carbon black with nano-scale pseudo-active particles, and (iii) 2.5 wt.% carbon black with nano-scale pseudo-active particles. The latter two cases were specifically chosen to investigate the effect of calendering before and after reaching the percolation threshold.

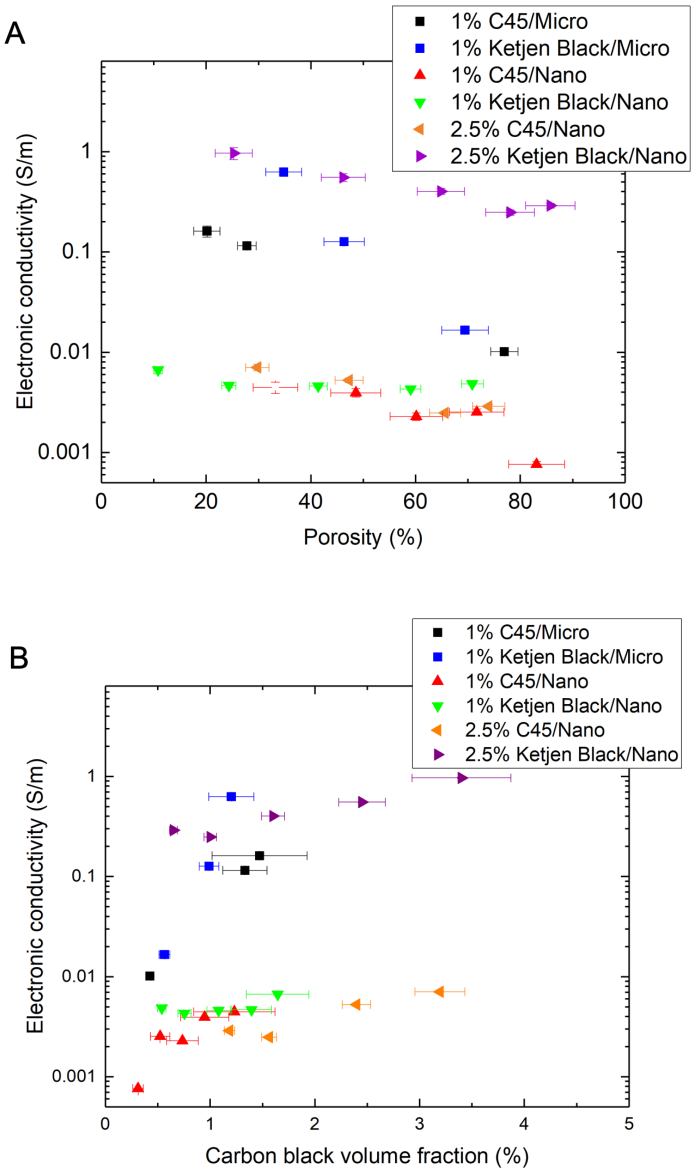

Figure 3-6: A) Electronic conductivity as a function of porosity for calendered electrodes. B) Conductivity data from the same experiments comparing the volume fractions of carbon black.

Among these cases it is observed that calendering electrodes made using micro-scale pseudo-active particles produced a greater increase in electronic conductivity than calendering electrodes made with nano-scale pseudo-active particles. However, the experiments also showed that, for a similar volume fraction of carbon black, the magnitude of electronic conductivity in the latter case is still substantially greater than that of micro-scale pseudo-active particles.

Despite the declining porosity engendered by calendering, the electrodes made with the nano-scale pseudo-active particles show only 40% improvement in electronic conductivity when porosity is reduced by 84%. In contrast, electrodes made with micro-scale pseudo-active particles demonstrate much greater electronic conductivity gains from a similar decrease in porosity. In particular, a 16-fold increase was observed when mixed with C45 and a 40-fold increase was observed when mixed with Ketjen black. Electrodes made with 2.5 wt.% carbon black and 92.5 wt.% nano-scale pseudo-active particles, while showing better conductivity, do not show as significant an improvement from calendering compared to electrodes with micro-scale pseudo-active particles.

The electronic conductivity was also characterized in the binder/carbon-black mixture that provides structural support and a conductive backbone to porous electrodes comprised of pseudo-active particles by fabricating and testing electrodes excluding pseudo-active particles (Fig. 3-7). In practice, the composition of these samples was varied by adjusting the mass fraction of PVDF relative to carbon black. While the experiments in the preceding section addressed understanding the effect of pseudo-active particle size on electrode properties, the present experiments provide insight into the effect of PVDF binder and carbon percolation on electronic conductivity.

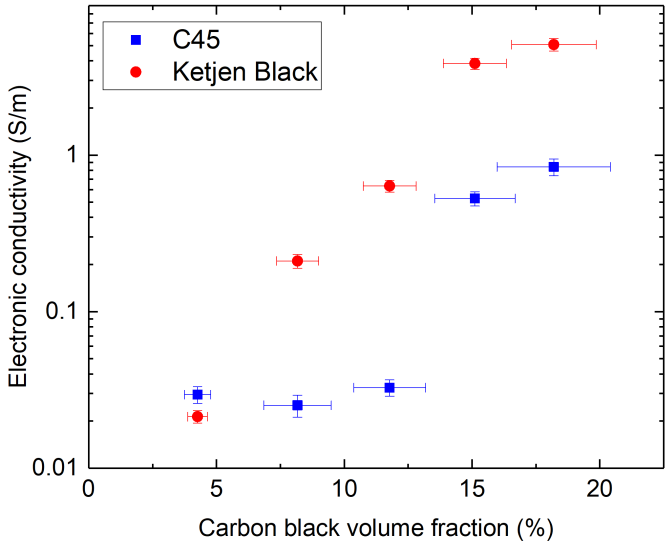

Figure 3-7: Electronic conductivity as a function of carbon black volume fraction for electrodes containing PDVF binder and either C45 or Ketjen black. From left to right, each corresponding sample is the result of mixing an additional 10 mg of carbon black with 50 mg of PVDF binder.

Without insulative particles occluding volume within electrode microstructures, these electrodes showed a range of electronic conductivity spanning 0.01-6.0 S/m. Here, Ketjen black samples consistently displayed higher conductivity than C45 samples for similar volume fractions. C45 samples showed little change in conductivity below a volume fraction of 14%, while Ketjen black samples showed continuously increasing conductivity from volume fractions as low as 8%. This result agrees with the experiments performed on electrodes composed primarily of pseudo-active particles, where Ketjen black particles showed a lower percolation threshold and improved the conductivity by orders of magnitude. Despite the carbon black volume fraction being approximately four times larger in these samples than in electrodes with pseudo-active particles, the electronic conductivities remain in a similar range, except for the highest volumes of Ketjen black that approach 10 S/m.

The most significant source of experimental uncertainty in the transport property measurements was electrode thickness. Although the Elcometer film applicator can cast electrode slurry with an accuracy of microns, electrodes were observed to shrink to approximately half of their initial thickness after wet phase inversion and subsequent drying. An uncertainty of 5 μm in electrode thickness measurement (MTI thickness gauge) was assumed to create the error bars shown in all figures for the values of conductivity, MacMullin number, permeability, porosity, and carbon black volume fraction.

3-7 Conclusions

Electrodes having different active particle and conductive additive size and mass fraction were fabricated here using a wet-phase inversion process with fixed amounts of polymer binder. To compensate for limited supplies of active material, insulative alumina particles were used in place of PBA for experiments. The effective transport properties of these electrodes were characterized using the four-point probe method and a gravity driven apparatus to measure hydraulic permeability. The different electrode formulations showed a complex interplay of effects that determine effective electronic conductivity, porosity, the MacMullin number for ion conduction/diffusion, and hydraulic permeability.

Smaller active particles showed better electronic and ionic conductivity with less carbon black loading, but such electrodes were also less permeable than those made with larger active particles. Making electrodes more electronically conductive thus comes at the cost of lower permeability, a tradeoff that will affect the relative contributions of electrical and pumping power requirements to total energy consumption in desalination.

CHAPTER 4: FARADAIC DEIONIZATION WITH PRUSSIAN BLUE ANALOGUES

4-1 Introduction to Faradaic deionization

To meet the growing demand for potable water, the cation intercalation materials often used in rechargeable batteries could enable the desalination of salt-rich water resources when paired with other cation intercalation electrodes [Prussian Blue analogues (PBAs) [10,12,26,101,102], $Na_{0.44}MnO_2$ (NMO) [33,102], and $NaTi_2(PO_4)_3$ (NTP) [33]], with conversion electrodes [NMO [34,103], NTP [81], and PBAs [104]], or with capacitive electrodes [NMO [34], $Na_3V_2(PO_4)_3$ [80], $FePO_4$ [84], TiS_2 [82,105], and V_2O_5 [106]]. Among such Faradaic deionization (FDI) cell architectures [7], cation intercalation desalination (CID) cells that use cation intercalation materials in both electrodes have shown promising energy consumption and specific salt removal [12,13,26] compared to capacitive deionization using electric double-layers. The predicted performance of CID [10,33,78,79] suggests that further improvements can be achieved, but mechanistic understanding of rate- and capacity-limiting processes [77] is needed to make CID competitive with reverse osmosis [107].

Recent modeling of coupled transport phenomena in FDI cells has shown that the flow of solution *through electrodes*, rather than the flow of solution *past electrodes*, can enhance desalination performance [78]. The development of flow-through electrode (FTE) CDI cells with fluid flow and current density aligned in the same direction has shown increased charging rates through the use of hierarchical [56] and laser-perforated [108] electrodes. Large volumes of electrolyte must permeate porous electrodes in FTE configurations to facilitate operation at high rate. Accordingly, pumping power and pressure, which are functions of electrode hydraulic permeability k_h and cell design, cannot be ignored when analyzing energy consumption [20,109].

In the related field of redox flow batteries, wherein electrolytes are often flowed through porous electrodes, few studies have measured k_h as a function of electrode composition, despite its influence on pressure drop when using different flow channel configurations, such as interdigitated, parallel, spiral, and serpentine [110–112]. For the electrodes that fabricated in this work k_h was measured and its influence on energy consumption in desalination was quantified.

After using theory to guide the selection of a particular electrode formulation on the basis of desalination energy consumption and rate, CID cycling performance was studied using optimized electrodes containing nickel hexacyanoferrate PBA in a flow-through CID cell. A framework was introduced for the selection of electrode materials based on these properties by modeling energy losses arising from viscous flow through electrodes and ionic/electronic ohmic polarization within electrodes at finite salt removal rate. Work in this chapter was reprinted from Ref. [89] with permission from Water Research.

4-2 Desalination cell apparatus

Based on the results of conductivity measurements in Chapter 2, Faradaic electrodes containing nickel hexacyanoferrate PBA as an active material were fabricated for desalination experiments. These new electrodes used nanoscopic Ketjen black particles as a conductive additive rather than the large C45 carbon black particles. PBA particles were prepared using the process developed previously [77]. Electrodes contained 85% active material, 5% Ketjen black, and 10% PVDF binder by mass, and slurries were prepared using 3 mL of NMP per gram of powder mixture. These slurries were cast, solidified, and dried using the same process as the alumina electrodes on a graphite foil substrate. A new cation intercalation desalination cell was designed and constructed for the desalination testing performed in this work (Fig. 4-1).

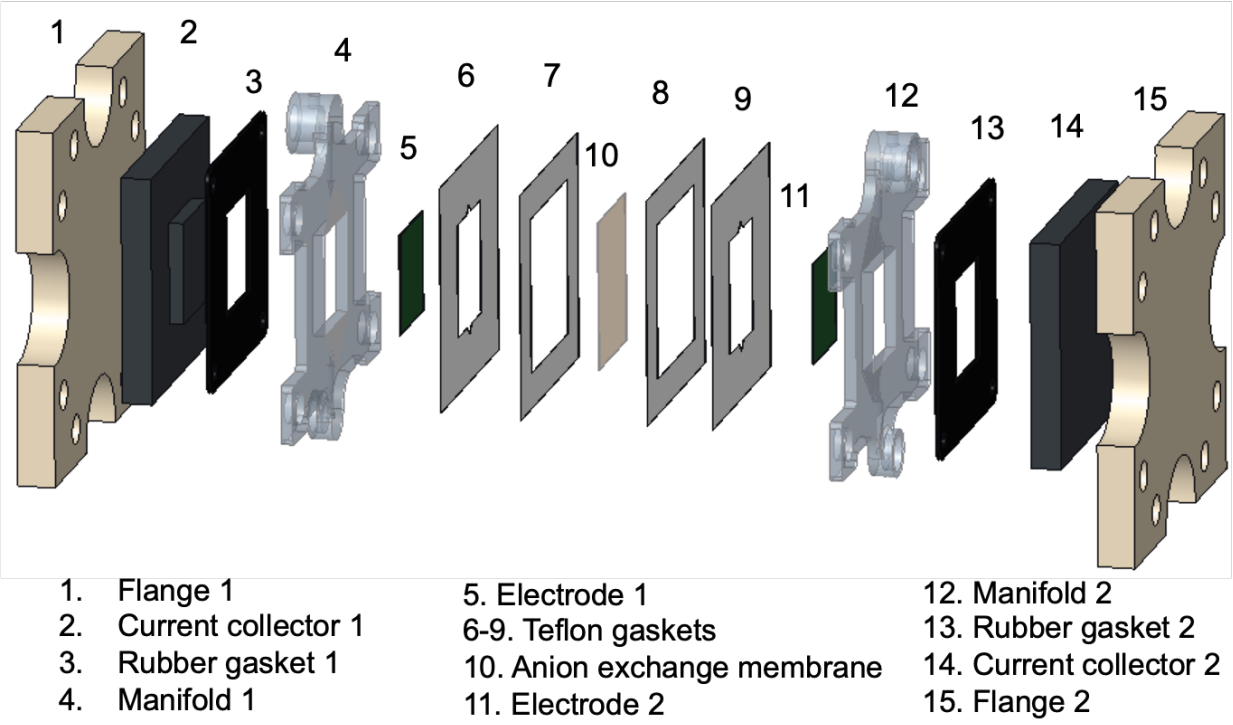

Figure 4-1: Exploded view of the flow-through FDI cell. Electrolyte is delivered into the system through two manifolds, passes through the anode and cathode during cycling, and effluent exits the system through two outlets of the manifolds. Electrodes are separated by an AEM, and gaskets prevent leakage and isolate the flows.

The desalination cell used a pair of machined graphite sheets as current collectors and a pair of manifolds 3D printed using a PolyJet Eden 350 printer, clamped together by a pair of laser-cut Delrin plates. The area of both anode and cathode was 2.5 cm^2 and approximately 150 μm thick, separated by an anion exchange membrane (Neosepta AMX). Influent was supplied to the cell from a single large reservoir with 100 mM NaCl concentration. Effluent concentration was measured using a pair of 17 μL flow-through conductivity probes (eDAQ). Flow was driven by a peristaltic pump (Masterflex L/S) to supply a flow rate of 0.25 mL/min.

Desalination tests were conducted by applying constant currents of 1, 2, 4, 6, and 8 mA/cm^2 to the electrodes using a VMP-3 potentiostat and measuring the effluent conductivity of the two

channels. Values for equivalent conductance were used to calibrate the conductivity sensors for 100 mM influent [63], and the differences in measured conductivity were proportional to differences in concentration. The difference in salt concentration between the influent and effluent was used to calculate each applied current's charge efficiency, the ratio between the number of charges from salt absorption and the applied current, and the average salt absorption rate. The energy consumed per mole of removed salt, or specific energy consumption, was found from the average power measured for that rate of salt removal.

4-3 Derivation of Electrochemical Desalination Ashby Plot Performance Contours

For each electron conducted through the solid matrix, a cationic charge must meet it at the solid-liquid interface, and a charge efficiency $0 < \Lambda < 1$ reduces the ratio of cationic charge to electronic charge compared with an ideally cation-selective intercalation material. For a saline water flow rate $\dot{V}$ which an FDI cell will desalinate, the charge of cations removed from the water must be matched by a corresponding electric charge. This condition requires the flow rate (m^3/s) to be proportional to the applied current density i (A/m^2) as $\dot{V} = ild/(zF\Lambda\Delta c_{e,L})$, where l and d are the length and width of the electrode, respectively. The current density i is proportional to the areal capacity of the electrode, divided by the cycle time. Increased electrode thickness w increases current density, while q and v_s are the volumetric capacity (C/m^3) and volume fraction of the active particles, thus requiring that $i = qv_s w/\tau$, where τ is the half-cycle time. Using these results, the flow rate required to sustain a degree of desalination $\Delta c_{e,L}$ (mM) for an electrode of specified dimensions and electrode properties is given as:

$$\dot{V} = \frac{qv_s w}{\tau}\frac{ld}{zF\Delta c_{e,L}\Lambda} \qquad (4-1)$$

In Eq. 4-1, z, Λ, μ, F, w, and l are cation valence, charge efficiency, viscosity, Faraday's constant, electrode thickness, and flow-path length.

Equation 4-1 reveals that, for a given half-cycle time τ, the flow rate of electrolyte into the electrode depends on the thickness w, length l, and depth d of the electrode. The difference in electrolyte concentration between the influent and effluent, $\Delta c_{e,L}$, determines what volume of electrolyte can be desalinated for a particular molarity. The effect of transport properties on desalination performance can be combined with operating conditions by accounting for ohmic and pumping power consumption within the FDI cell.

Assuming ionic and electronic current in series, power consumption P (W) is expressed in terms of total current I and flow rate $\dot{V}$ as:

$$P = I^2 \frac{w}{ld}\left(\frac{1}{\kappa_{eff}} + \frac{1}{\sigma_{eff}}\right) + \dot{V}^2 \frac{l}{wd}\frac{\mu}{k_h} \qquad (4-2)$$

Pumping power is proportional to the square of the flow rate. Substituting Eq. 4-1 into 4-2 and using the $I = ild = qv_s wld/\tau$ power was expressed:

$$P = \left(\frac{qv_s w}{\tau}\right)^2 \left(\left(\frac{wld}{\kappa_{eff}} + \frac{wld}{\sigma_{eff}}\right) + \left(\frac{1}{zF\Delta c_{e,L}\Lambda}\right)^2 \frac{\mu}{k_h}\frac{l^3 d}{w}\right) \qquad (4-3)$$

Specific energy consumption (SEC), or the amount of energy needed to remove one mole of salt from feedwater, is a commonly used metric to quantify these effects in CDI. Furthermore, SEC is inherently a function of the average salt adsorption rate (ASAR), defined as the average salt absorbed for a unit electrode area [70]. By expressing the energy consumption due to pumping power also a function of current (rather than pressure difference), SEC (kJ/mol) can be directly related to the ASAR (μmol/cm^2-min). Eq. 4-3 reflects that, in order to remove salt more quickly, proportionally more energy must be invested for a given set of material properties and design

parameters. Although power consumption is proportional to the square of current, the power per volume of water increases linearly with flow rate due to the connection between the flow of electrolyte and electrons:

$$\frac{P}{\dot{\forall}} = \left(\frac{q v_s w}{\tau}\right)\left(zF\Delta c_{e,L}\Lambda\left(\frac{w}{\kappa_{eff}} + \frac{w}{\sigma_{eff}}\right) + \frac{\mu}{k_h}\frac{l^2}{w}\left(\frac{1}{zF\Delta c_{e,L}\Lambda}\right)\right) \qquad (4-4)$$

SEC is then found by dividing the energy per volume of water by the degree of desalination $\Delta c_{e,L}$, giving the energy per mole of salt removed:

$$SEC = \frac{E}{V\Delta c} = \left(\frac{q v_s w}{\tau}\right)\left(zF\Lambda\left(\frac{w}{\kappa_{eff}} + \frac{w}{\sigma_{eff}}\right) + \frac{\mu}{k_h}\frac{l^2}{w}\left(\frac{1}{zF\Lambda\left(\Delta c_{e,L}\right)^2}\right)\right) \qquad (4-5)$$

ASAR can also be expressed as a function of the current density, because the rate of cations being adsorbed per unit area is directly proportional to the electronic current:

$$ASAR = \frac{\dot{\forall}\Delta c_{e,L}}{ld} = \frac{1}{ld}\frac{q v_s w}{\tau}\frac{ld}{zF\Lambda} \qquad (4-6)$$

where Faraday's constant F and charge efficiency Λ are used to express the molar removal flux of cations. Substituting Eq. 4-6 into 4-5, the following analytical expression for SEC is found:

$$SEC = ASAR\left((zF\Lambda)^2\left(\frac{w}{\kappa_{eff}} + \frac{w}{\sigma_{eff}}\right) + \frac{\mu}{k_h}\frac{l^2}{w}\frac{1}{\left(\Delta c_{e,L}\right)^2}\right) \qquad (4-7)$$

4-4 Analysis of energy consumption in porous electrodes

The electronic conductivity σ_{eff}, ionic conductivity κ_{eff}, and hydraulic permeability k_h of porous electrodes will influence how an FDI device consumes energy. Specifically, energy losses arise from electronic resistance, ionic resistance, and pumping power, in addition to baseline energy consumption due to the Gibbs free energy of separation. To put the transport properties measured in context for FDI applications, an Ashby diagram was constructed to project their

impact on ASAR for a specified SEC level. Each point in this "materials selection map" is defined by a transport property triplet $(\sigma_{eff}, \kappa_{eff}, k_h)$. Analytical modeling was used to construct contours of constant SEC and ASAR, so as to define guidelines for materials selection.

For certain $(\sigma_{eff}, \kappa_{eff}, k_h)$ operating flow rate was selected in terms of applied current density by using a balance of charges when salt concentration is reduced from a feed stream with concentration c_e^{in} (mM) by a desired amount $\Delta c_{e,L} = c_e^{in} - \bar{c}_e^{out}$, where the mean effluent concentration is $\bar{c}_e^{out}$ and the subscript L denotes a "longitudinal" concentration difference. Using Eq. 4-7, ASAR contours were constructed for a given SEC with varying κ_{eff}, σ_{eff}, and k_h to show the combinations of electrode properties that are necessary to reach a desired ASAR, as shown in Fig. 4-2. Concave surfaces comprise these contours because increasing one of the three transport properties reduces a portion of energy consumption enough that only the other two contributions remain significant. The further out a point is along all three axes, the higher an ASAR that is attainable.

Figure 4-2 shows that electronic conductivity, ionic conductivity, and permeability can all be increased to reduce the overall SEC of an electrode if a particular ASAR is required. However, the energy demands of the three transport properties are each independent of the others, and even if one could be increased by orders of magnitude, the energy demands would become dominated by the others. Ionic conductivity is particularly difficult to control, which motivated the research in Chapter 1 aiming to reduce MacMullin number for the purpose of making CDI a viable technology. Permeability has also been the subject of efforts to improve the performance of CDI via the addition of macroscopic pores to reduce flow resistance [108]. Numerous examples of work with various carbon black additives have attempted to improve electronic conductivity [113–115]. The materials tested show permeability an order of magnitude above what is necessary, however

the varying MacMullin numbers order-of-magnitude variations in electronic conductivity limit the possible ASAR.

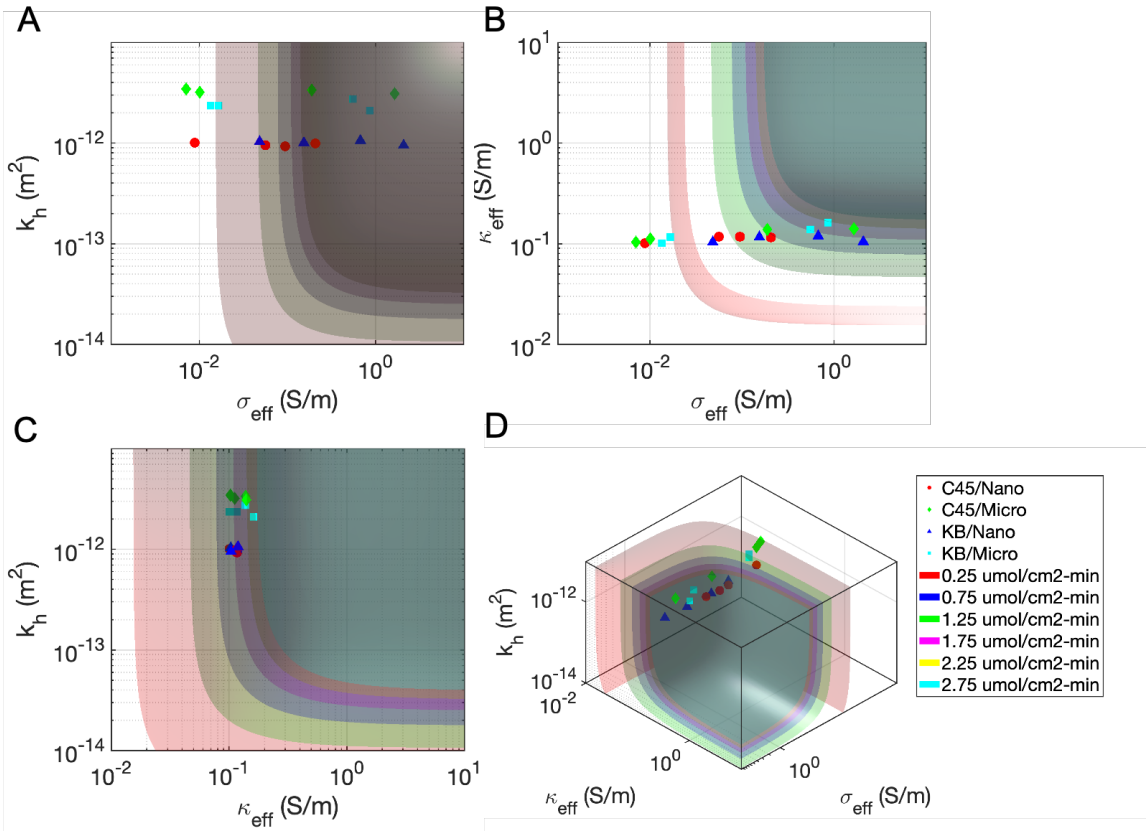

Figure 4-2: Curves of average salt adsorption rate for varying transport properties of the electrodes. Sub-figures A-C depict the contours of D projected onto individual planes. Specific energy consumption is set to be 1.5 times the thermodynamic minimum for 100 mM aqueous NaCl, or 8.2 kJ/mol, with 10 mM effluent and 50% water recovery. Overlaid in this space are the transport property data for the various electrodes characterized in Chapter 3.

4-5 Desalination Experiments

After completing experiments varying the carbon black content of the electrodes, PBA electrodes were fabricated using 5 wt% Ketjen black rather than C45 due to the former carbon black's demonstrated superiority as a conductive additive. Electrode samples with 2.5 cm^2 area were then used in a symmetric CID cell with flow of electrolyte through electrodes. Galvanostatic

cycling of the electrodes was performed at current densities of 1 to 8 mA/cm^2 with a flow rate of 0.25 mL/min and 100 mM NaCl influent.

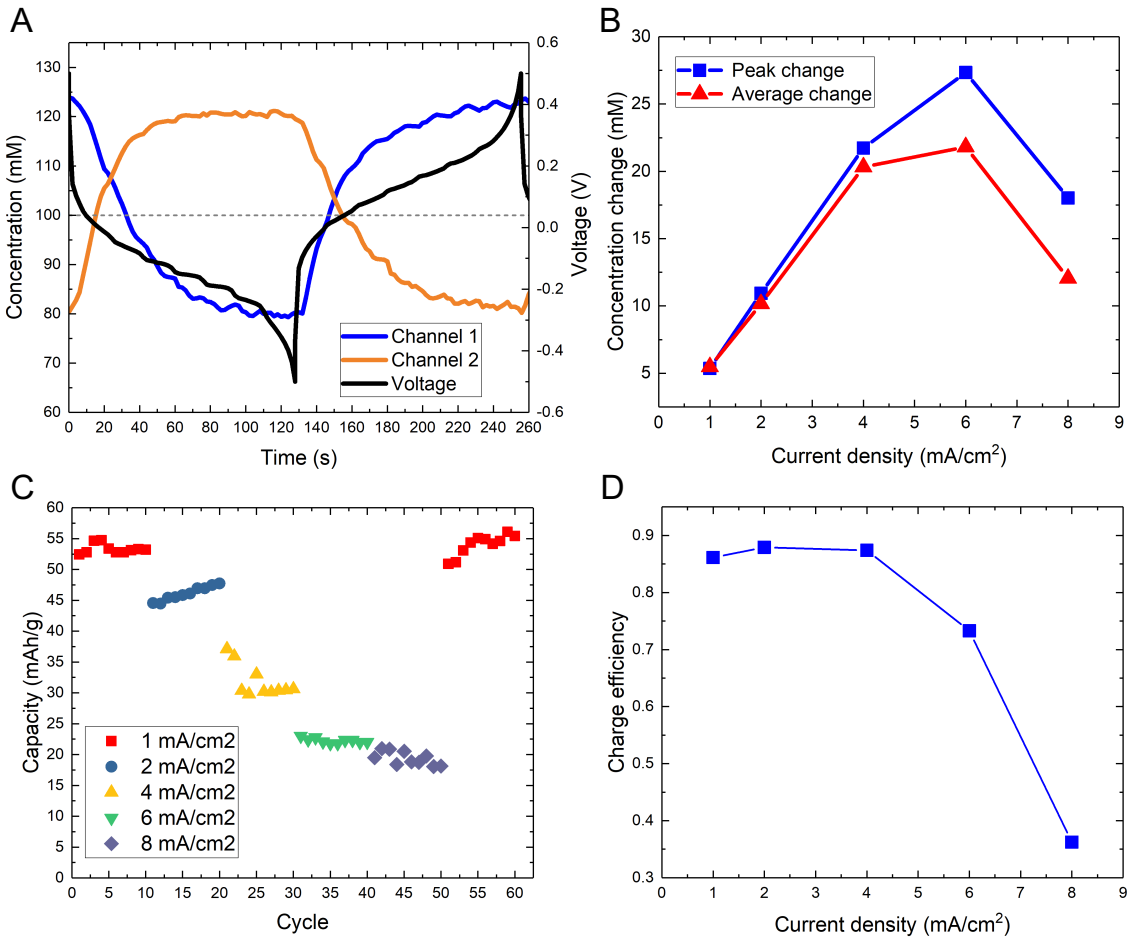

Figure 4-3: A) Desalination performance and voltage profile for one complete charge/discharge cycle at 6 mA/cm^2. B) Peak and average concentration changes for tested current densities. C) Capacity versus cycle for tested current densities. D) Charge efficiency versus current density.

The desalinating electrode intercalated sodium ions from influent while chlorine passed through the AEM into the counter-electrode, resulting in the inlet-to-outlet concentration differences and voltage variations shown in Fig. 4A for a current density of 6 mA/cm^2. The change in concentration is approximately linearly dependent on current density, as increasing the current removing salt at a certain flow rate ideally removes a proportional amount of salt (Fig. 4-3B). At

1 mA/cm^2, the PBA particles show a specific capacity of 50-55 mAh/g that decreases with increasing current, though the values at each current density remain stable across the ten cycles performed. Subsequent tests showed capacity at 1 mA/cm^2 returned to over 50 mAh/g, and the average over ten cycles was 1.2% greater than the average for the forty cycles prior. (Fig. 4-3C). Charge efficiency (CE) was highest at low current densities, and the decline of CE caused a drop in the measured concentration difference (Fig. 4-3D).

At 8 mA/cm^2 the performance of the cell declines significantly, likely an effect due to poor flow efficiency and short residence times in the cell [71]. A certain volume of effluent must flow out of the electrode during cycle time and reach the conductivity meter to be measured, however the high current and lowered capacity causes a given half-cycle to complete too quickly. At 8 mA/cm^2 half-cycle time is less than 60 seconds. With an electrode volume of approximately 36 µL, the volume of fluid in the electrode flows less than seven times during each half-cycle. Reliable conductivity measurement also becomes more difficult due to the time the fluid exiting the electrode needs to reach the conductivity sensor being close to that of the half-cycle time. In Sec. 3-2 the theoretical estimation of power consumption for a given salt removal level assumes an infinite charge capacity and constant effluent salt concentrations, however experimental data shows the charging time limits reliable measurement and calculation of salt removal.

To confirm the superiority of the Ketjen black over the C45 shown in tests with alumina electrodes, PBA electrodes containing 5 wt% C45 were also prepared and tested in the FDI cell under identical conditions. Direct property comparisons between the different electrodes are shown in Table 3-1. At a current density of 1 mA/cm^2, their capacity was less than 5% of that measured for the PBA/Ketjen-black electrodes, with a maximum concentration change of less than

2 mM. At current densities of 2 mA/cm^2 and above, PBA/C45 electrodes did not function reliably and could not produce useable experimental data.

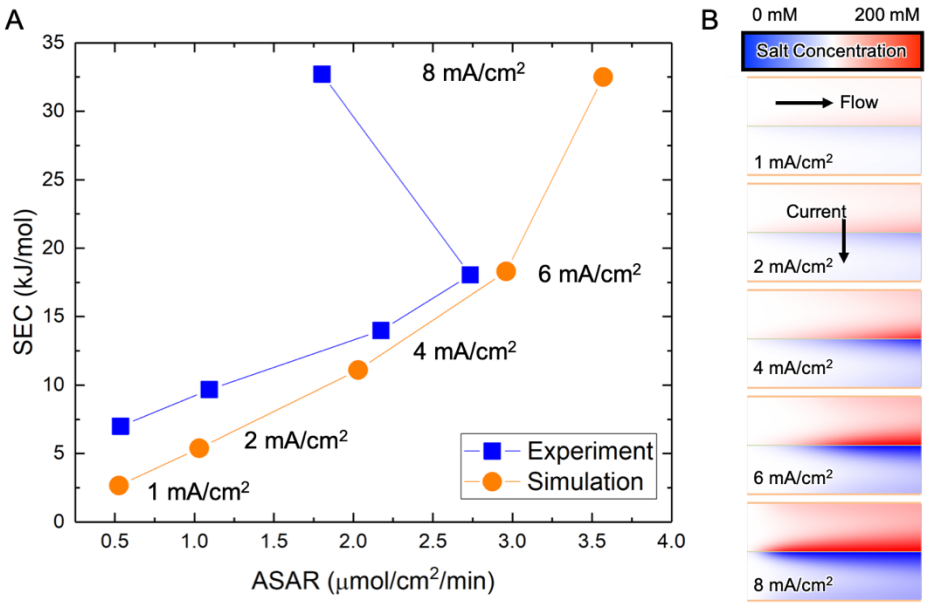

Figure 4-4: A) Specific energy consumption versus average salt absorption rate for both experimental and simulated cases. With the exception of the 8 mA/cm^2 case, ASAR increases with current density. B) Simulated salt concentration at the end of the second half-cycle for each current density.

Analysis of net electrical energy input showed relatively low SEC for the ASAR values observed, showing substantial improvements in specific energy consumption and current density. Previous CID cells using multiple intervening ion-exchanges membranes reported values of 14.7 kJ/mol for 50 mM influent and 0.57 mA/cm^2 [13], while the present experiments using optimized electrodes produce lower SEC for current densities as high as 4 mA/cm^2. The initial demonstration of CID using flow behind PBA electrodes decreased salt concentration from 20 mM NaCl influent by only 0.5 mM at 0.14 mA/cm^2, while consuming 15 kJ/mol [12]. Other work using dissimilar PBAs in a CID configuration reported an SEC of 5.0 kJ/mol for 500 mM influent at 0.5 mA/cm^2 [26]. Symmetric anion-selective electrodes separated by a cation exchange membrane desalinated

20 mM saltwater with both lower current density and lower ASAR with an SEC of 3.6 kJ/mol and a concentration change of <3 mM at current densities of 0.75 mA/cm^2 or less [22]. It must be noted that differing influent concentrations used in these experiments would impact the expected correlation between SEC and ASAR compared to this work.

Desalination performance was simulated using a two-dimensional, time-dependent model presented previously [10] that assumes thin, ideally permselective membranes, and equal isotropic effective transport properties. The increased SEC relative to simulations shown in experiments (Fig. 4-4A) can thus be attributed to ohmic polarization, agglomerate-scale transport, and transport anisotropy within porous electrodes. In addition to these factors, simulations suggest that the transport of ions transverse to the flow direction has a significant impact on energy consumption. Substantially lower ASAR was achieved in experiments at the highest current density tested (8 mA/cm^2, top-most point in Fig. 4-4A). This discrepancy is primarily attributable to electron transport limitations in PBA agglomerates as the present experiments produced approximately 30% charge capacity utilization relative to theoretical, consistent with previous work characterizing and modeling agglomerate-scale transport at similar C-rates [77].

Figure 4-4B shows the simulated distribution of salt concentration within the CID flow cell at the end of one half-cycle with transverse coordinate y and streamwise coordinate x. Near the outlet of the cell, salt concentration variations transverse to the flow direction are evident, resulting in a minimum concentration within the desalinating electrode $c_{e,min}^{out}$ that is substantially smaller than the mean effluent concentration $\bar{c}_e^{out}$ in that electrode. Further, this transverse concentration difference $\Delta c_{e,T} = \bar{c}_e^{out} - c_{e,min}^{out}$ increases as the applied current density increases. Previous modeling [10,33,78,116] revealed similar effects that result from the cation transference number t_+ in aqueous NaCl ($t_{e,+} \approx 0.39$) exceeding that of anion-exchange membranes ($t_{m,+} \approx 0$). By

solving the salt transport equation (see ESM), a closed form expression was found for the transverse concentration difference $\Delta c_{e,T}$: $\Delta c_{e,T} = \bar{c}_e^{out} - c_e(x = l, y = w) = it_+ w/\left(3\widetilde{D}_{eff}F\right)$, where $\widetilde{D}_{eff}$ (m^2/s) is the effective chemical diffusion coefficient of salt. Among the current densities tested, this expression predicts $\Delta c_{e,T}$ within 10% of the higher fidelity numerical simulations, enabling its use in identifying conditions that prevent local salt depletion (i.e., when $\Delta c_{e,T} > 0$) when flow-through cation intercalation electrodes are used.

4-6 Conclusions

A simplified analytical model of cell polarization was used to quantify the contributions to specific energy consumption through electronic conduction, ionic conduction, and feedwater pumping. In so doing, an electrochemical Ashby diagram was constructed in which different electrode formulations are represented by their corresponding transport property triplet $(\sigma_{eff}, \kappa_{eff}, k_h)$ and contours in that space quantify salt removal rate (ASAR) at fixed specific energy consumption (SEC). It was found that increasing any one of these properties (electronic conductivity, ionic conductivity, and permeability) increases ASAR at fixed SEC, but for the electrode formulations tested electronic conductivity had the most significant influence on ASAR. Such methods can be used in the optimization of electrode formulations for other Faradaic deionization systems. Note, however, that in addition to energy consumption material selection should also consider the constraints imposed by the limited pressure that can be sustained by seals within a given desalination flow cell.

Using the results for electrodes fabricated with pseudo-active particles, high-conductivity nickel hexacyanoferrate PBA electrodes were fabricated using Ketjen black conductive additive and were tested in a symmetric cation intercalation desalination (CID) device at varying current

densities with 100 mM NaCl feedwater. These electrodes were able to reduce salt concentration over 25 mM at current densities several times higher (up to 8 mA/cm^2) and at higher salt absorption rates (up to 2.7 μmol/cm^2-min) than previous CID studies. Thus, understanding the interplay between transport properties and their variation with conductive additive loading can lead to superior performance in porous electrodes used for Faradaic deionization. Comparison of numerical modeling results with this experimental data suggests that solution phase mass transfer transverse to the flow direction could be enhanced to increase rate capability and decrease energy consumption.

While the present experiments demonstrate substantial salt removal, engineering of desalination cells and systems are needed to produce effluent salt concentrations to the levels needed for practical application (e.g., drinking water production). The present experiments showed that the electrodes fabricated are robust over the cycles tested, but targeted investigation of capacity fade and electrode degradation processes are needed together with analysis of the impact of potential degradation products on water quality. Improvements can be made to the materials selection analysis to incorporate the effects of the finite charge capacity and local ion transport effects. Furthermore, understanding the impact of electrode properties on selective electrochemical separations deserves attention, in addition to their impact on the treatment of feedwaters containing mixtures of different cations.

CHAPTER 5: COLLOID-INSPIRED FABRICATION OF CONDUCTIVE ELECTRODES

5-1 Fabricating electrodes for greater conductivity

To produce thicker electrodes, a wet-phase inversion (WPI) process is used that eliminates the capillary-bridge induced cracking that arises during solidification by drying. While others [48] have used WPI to fabricate electrodes for FDI and capacitive deionization using a room temperature pure water bath, here a heated, alkaline WPI process inspired by the Derjaguin-Landau-Verwey-Overbeek (DLVO) theory of inter-particle forces in colloids [117] is introduced. The DLVO theory has previously predicted percolation thresholds in simulated dispersions [118] and is applied here towards slurry constituents to induce solidification of thick, high-conductivity electrodes that are subsequently calendered. While past simulations based on Brownian dynamics of conductive particles in electrode slurries predicted that larger particles form conductive paths more easily [119], previous experiments on slurries containing PBA nanoparticles and carbon black showed trends opposite those simulations. Rather than expecting particles to pack together randomly as in Brownian dynamics, per DLVO theory van der Waals and electrostatic forces are posited to influence their dynamics to a degree dependent on particle radii, zeta potential, and Hamaker constants of the associated particles and on the dielectric properties of intervening fluid.

Applications of colloidal forces between electrode particles include forming mechanically-stable electrodes without additional binder [120], carbon coating in $LiFePO_4$ batteries for better electronic conductivity [121], and preparation of $LiFe_{0.5}Mn_{0.5}PO_4/C$ nanocomposite electrode materials [122]. Self-assembly in lithium-ion batteries by applying these forces to create complex interpenetrating anode and cathode networks has also been proposed [123]. Understanding inter-

particle forces can also be related to rheological behavior of an electrode slurry with different constituent particle radii and volume fractions [124]. The interplay between such forces has been simulated for Li-ion battery electrodes, showing variations in electrode microstructure dependent on the mass fraction, particle size, and temperature of both CIM and additive particles [17,18], such forces' effects were not previously exploited in practical electrode fabrication until now. In doing so, the colloid-inspired electrode fabrication process results in more electronically conductive and mechanically stable electrodes that do not crack at high cast thicknesses.

Calendering, the process of compressing electrodes between two rollers, is known to increase electronic conductivity and improve rate capability [19], but decreased porosity and increased tortuosity are known to reduce ionic conductivity [14,15,37]. While these competing effects may result in a certain degree of calendering that maximizes FDI performance, the fabrication of thick electrodes with the areal capacity levels needed to create low-porosity electrodes using calendering is a challenge in itself. The reduction of cost and inactive mass in Li-ion batteries [125] has motivated development of alternative electrode fabrication processes to yield high areal capacity [126] due to the tendency of conventionally-prepared electrodes to crack during drying after slurry casting. Calendering of these electrodes increases their density and electronic conductivity, which is shown to enhance salt removal and thermodynamic efficiency in FDI.

In this chapter, theories of colloidal interactions were applied towards electrode slurries to understand how the dispersed particles aggregate during solidification. Based on the interparticle forces, new fabrication techniques were developed to increase electronic conductivity of electrodes, which were experimentally tested using alumina pseudo-particle electrodes. Results showed that despite electrodes containing the same mass fractions of constituent particles,

electronic conductivity could vary by two orders of magnitude. These techniques were then combined with calendering to produce dense, high-conductivity electrodes for use in the FDI cell.

5-2 DLVO theory applied to electrode slurry

To develop useful guidelines in electrode fabrication, it is necessary to find physical explanations for why certain particles aggregate together more easily than others. One explanation for the effect of particle size on the final properties of the electrode comes from treating the initial slurry as a colloid. Rather than expecting particles to randomly pack together entirely due to Brownian motion, their dynamics are influenced by van der Waals and electrostatic forces, the strength of which depend on particle composition, radii, and their volume fraction in the slurry. The interplay between such forces has been simulated in previous research on Li-ion battery electrodes, showing variations in electrode microstructure depending on the mass fraction of active and conductive particles, particle size, and temperature [17,18]. In a case with ideal, spherical particles, attractive force is determined by the Hamaker constant A, the distance between particles d, and their respective radii R [127]. The DLVO theory can be used to predict the interparticle potential E_{ij} acting between two particles i and j separated by a distance x, including competing contributions from van der Waals and electrostatic forces [117]:

$$E_{ij} = \left(64\pi\varepsilon D\left(\frac{k_B T}{e}\right)^2 tanh\left(\frac{e\zeta_i}{4k_B T}\right) tanh\left(\frac{e\zeta_j}{4k_B T}\right) e^{-x/\lambda_D} - \frac{A_{ij}}{6x}\right)\frac{R_i R_j}{R_i + R_j} \qquad (5-1)$$

When both particles are immersed in a fluid with their own Hamaker constant, in this case a mixture of NMP and dissolved PVDF, the fluid reduces the overall attractive force between particles, an effect which can be approximated using the following equation [127]:

$$A_{ij} = \left(\sqrt{A_{ii}} - \sqrt{A_{solvent}}\right)\left(\sqrt{A_{jj}} - \sqrt{A_{solvent}}\right) \quad (5-2)$$

The alumina particles used as pseudo-active material here possess a Hamaker constant of 1.45×10^{-19} J in vacuum [128], while carbon black particles possess a value of 2.53×10^{-19} J [129], and the NMP solvent's constant is 8.21×10^{-20} J [17]. It should be noted the latter value does not take the presence of the polymer binder into account and only gives an approximation. The presence of solvent results in a Hamaker constant between the carbon black particles equal to 4.69×10^{-20} J and only 2.04×10^{-20} J between the carbon black and the alumina. The preferential attraction between carbon black particles enables the percolation of the carbon black network, rather than random Brownian motion which acts to disperse them, because carbon black particles are more attracted to each other than to the pseudo-active particles. Such an effect is likely less significant for larger carbon black particles because of the weakening of van der Waals forces in such systems, and explains adding C45 improves electronic conductivity less than smaller Ketjen black particles [100].

The distance d between the carbon particles can also be used to explain the percolation of smaller particles. Knowing the average particle radii and their volume fraction in the slurry makes the average spacing between the particles calculable. Assuming the slurry is thoroughly mixed, smaller particles will be closer together, increasing the attractive forces between them. Larger active particles are better able to attract smaller particles at the same distance, allowing these larger particles to cling to large numbers of carbon black particles rather than to allow conductive additives to form a conductive path through the electrode. Decreasing the radii of both particles, as shown in Eq. 5-1, reduces the attractive forces between them if they both remain at the same distance, and experimental results demonstrate that smaller pseudo-active and conductive particles form electrodes with greater electronic conductivity. As particles become smaller for a specified

volume fraction, their number density increases and they become closer together on average, lowering the distance d. However, as the particles become smaller, the average distance between particle decreases, diffusivity increases, and the time between interactions becomes proportional to R^3. Treating the particles as static becomes a less realistic approximation as the particles move across that distance hundreds or thousands of times each second. Finding the volume fraction at which this "backbone" of carbon black forms, or the percolation threshold, is of interest in fabricating conductive electrodes without sacrificing energy density. Past work into percolation includes simulations of particles packing together taking into account the relative sizes and number densities of the conductive particles [130], however van der Waals forces were not explicitly taken into account. Simulations using Brownian dynamics have been performed to optimize conductivity, however they showed larger particles form conductive paths more easily, results opposite to what has been found experimentally in the present research [131].

Particle size plays a significant role in how particles aggregate. Due to the differences in how electrostatic and van der Waals forces depend on distance, there is a distance x_0 at which the forces are equal and opposite, causing total inter-particle force F_{ij} to become zero. As both forces are similarly dependent on particle radii, x_0 is independent of particle size. If particles come closer together, they will become attracted to each other.

$$F_{ij} = \left(64\pi\varepsilon_0\varepsilon_r\left(\frac{k_BT}{e}\right)^2 tanh^2\left(\frac{e\zeta}{4k_BT}\right)e^{-\frac{x_0}{D}} - \frac{A_{ij}}{6{x_0}^2}\right)\frac{R_iR_j}{R_i+R_j} \qquad (5-3)$$

The region in which particles are attracted to each other extends out from the surface of the particle surface, forming a volume around the particle. The size of this volume compared to the volume of solvent the particles are suspended in can be calculated assuming the particles are perfect spheres.

$$v = \frac{V_c}{V_{NMP}}\left(\left(1+\frac{x_0}{R}\right)^3 - 1\right) \qquad (5-4)$$

Smaller particles will have a larger "attractive volume" within which other particles will become trapped, resulting in more contact between conductive particles. This is supported by the demonstrated superiority of Ketjen black over larger C45 particles for increasing conductivity of PBA electrodes.

5-3 Modified wet-phase inversion

The alumina particles used in initial tests were purchased from AdValue Technology and were previously used as insulative "pseudo-active" particles in place of intercalation compounds to test the effect of conductive additives in Chapter 3. By making the comparison between a colloid and the electrode slurry, it was possible to use the DLVO theory of inter-particle forces to estimate the effect of modifying the DI water bath properties on the electrode microstructure. The conductive and active particles in a slurry exert electrostatic and van der Waals forces on each other in manners which can be manipulated. When developing the modified WPI process, DLVO theory was employed to guide experimental parameters based on how inter-particle forces were expected to change with bath properties

In Eq. 5-1, E_{ij} is recognized to depend on particle radius R_i, particle zeta potential ζ_i, interparticle Hamaker constant A_{ij}, Debye length λ_D, dielectric permittivity ε of intervening solution, diffusivity of ions in solution D, and the thermal voltage $k_B T/e$. Within the electrode slurry, interactions between particles are governed by van der Waals and electrostatic forces, illustrated in Fig. 5-1A, in which active and conductive particles are suspended in a slurry surrounded by NMP solvent. These forces remain active during the solidification process as NMP is removed and replaced by water from the bath. The van der Waals force is always attractive, determined by the Hamaker constant A, the distance between particles x, and their respective radii

R [127]. When both particles are immersed in a fluid with its own Hamaker constant (in this case a mixture of NMP and dissolved PVDF) the fluid reduces the overall attractive force between particles, an effect which can be approximated using Eq. 5-2. The Al_2O_3 particles used as a surrogate material possess a Hamaker constant of 1.45×10^{-19} J in vacuum [128], while carbon black particles possess a value of 2.53×10^{-19} J [129], and the NMP solvent's Hamaker constant is 8.21×10^{-20} J [17]. It must be noted the latter value does not take the presence of the PVDF binder into account. The presence of solvent results in a Hamaker constant between the carbon black particles equal to 4.69×10^{-20} J and only 2.04×10^{-20} J between the carbon black and Al_2O_3. The preferential van der Waals attraction between carbon black particles enables the aggregation of the carbon black network, rather than random Brownian motion which acts to disperse them, because carbon black particles are more attracted to each other than to the pseudo-active particles. However, electrostatic repulsion acts against this aggregation.

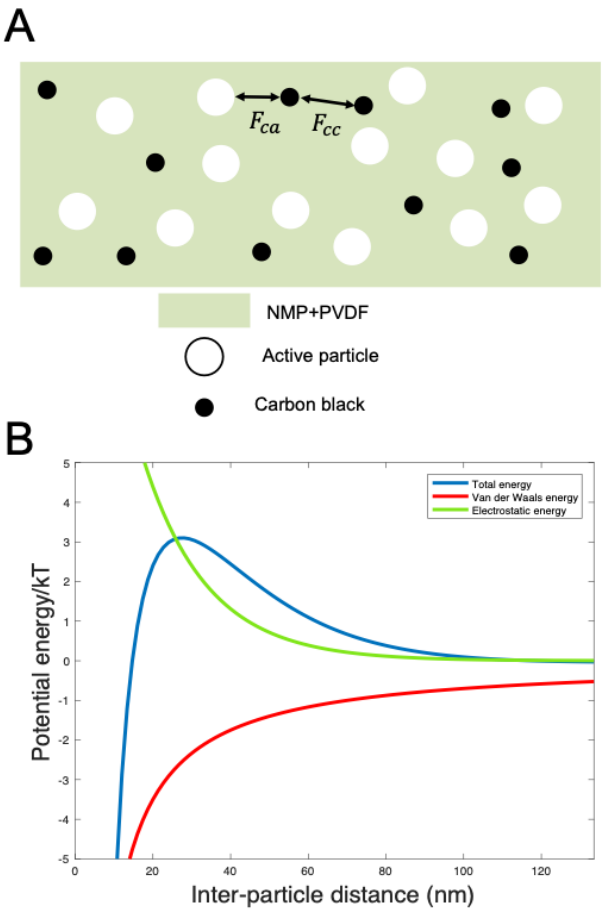

Figure 5-1: (A) Simplified depiction of active and conductive particles in a colloid where they are subjected to inter-particle forces. (B) Potential energy versus separation distance of two Al_2O_3 particles in NMP, normalized by thermal energy, based on the DLVO theory. This total potential energy is the sum of attractive van der Waals interactions and repulsive electrostatic energy shown as separate curves.

There were three techniques tested to improve electronic conductivity of electrodes: increasing temperature, increasing salt concentration, and increasing pH of the deionized water bath used for wet-phase inversion. The water bath was heated from room temperature up to 85°C at 20°C intervals. Ionic strength of the bath was increased through the addition of NaCl. The bath pH was increased from 7 to 12 by incrementally adding sodium hydroxide which had been diluted in DI water.

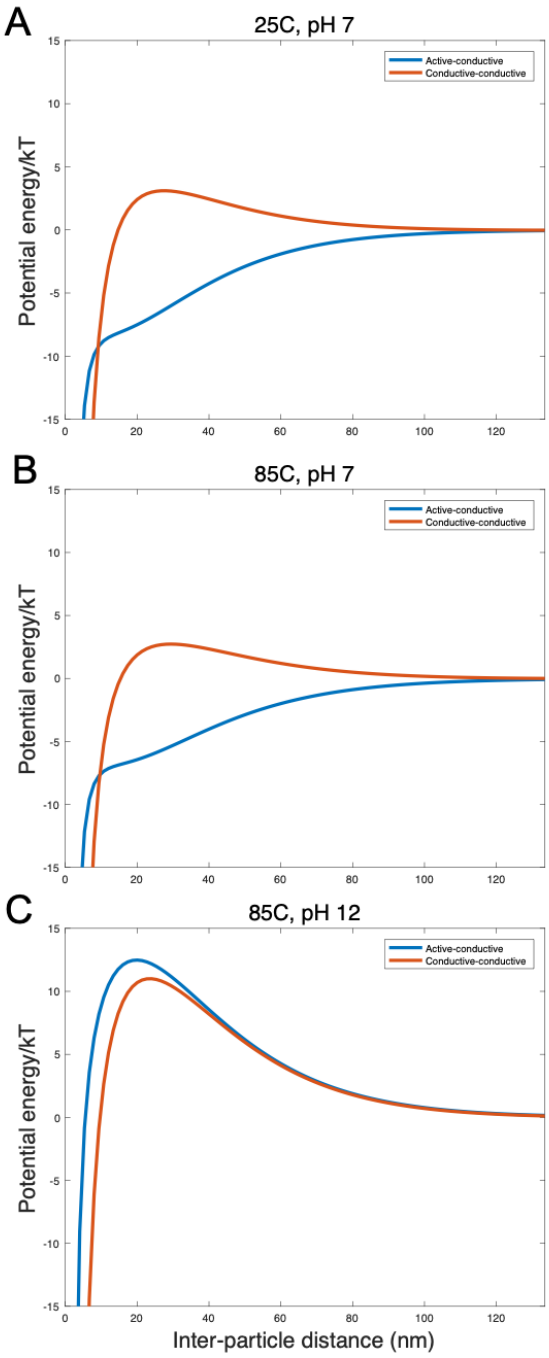

Figure 5-2: Curves of force versus distance for carbon and alumina particles in water baths with different properties during wet-phase inversion.

The potential energy curves of three different baths are shown in Fig. 5-2, illustrating how increasing bath temperature and pH leads to the increase in conductivity of alumina pseudo-particle electrodes. By increasing bath temperature, the repulsive energy between conductive carbon particles expected by the DLVO theory increases by only 8%, but the thermal energy of the particles in the slurry increases 28%, giving them more energy to overcome that repulsion to induce their aggregation. Then, when increasing pH, the zeta potential's magnitude increases, causing strengthened repulsion between carbon. However, the zeta potential of Al_2O_3 changes signs, repelling the carbon, and the repulsive energy between carbon and Al_2O_3 is greater than between two carbon particles. As a result, carbon particles prefer to aggregate with each other, rather than to aggregate with the other Al_2O_3 particles.

These modifications to the wet-phase-inversion process alter the inter-particle energies in different ways. As two particles with zeta potentials of the same sign approach each other, they will be electrostatically repelled. If the water bath is at a higher temperature, the particles will have more energy with which to overcome the electrostatic repulsion. Zeta potential can be changed by increasing or decreasing pH of the bath. At higher pH, the zeta potential of the alumina particles crosses its isoelectric point and changes from positive to negative, becoming repulsive to carbon black. While the electrostatic repulsion between carbon particles has also increased in magnitude, the repulsion between the carbon and alumina becomes even greater.

5-4 Colloid-inspired fabrication

Increasing the ionic strength of the bath also showed improvement, however after a certain point the conductivity declined from a maximum value. This is hypothesized to be the result of flocculation of the carbon particles. Continuously increasing salt concentration

decreases the strength of the electrostatic repulsion between like particles and encourages aggregation, however if that force is removed completely the particles can form large agglomerates instead of a dispersed network.

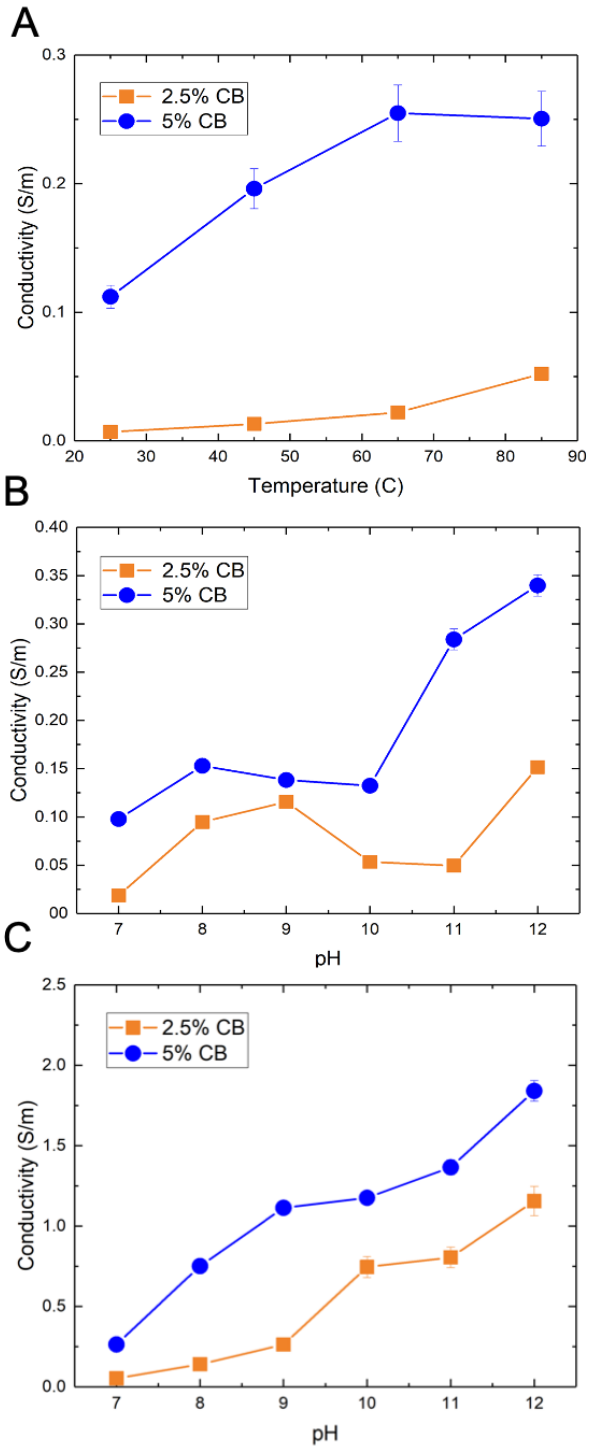

Figure 5-3: Electronic conductivity for electrodes with 2.5 and 5 wt% C45 carbon black made using (A) increasing bath temperature and (B) increasing bath pH. Error bars are found from the 5 µm variability in electrode thickness which determines how conductivity is calculated using a four-point probe. (C) Electronic conductivity for electrodes made at 85ºC using an alkaline bath.

The greatest enhancements were achieved through a combination of heating the DI water and increasing its pH. Making the electrostatic repulsive force between conductive and pseudo-active particles strong while supplying more energy for conductive particles to overcome their mutual repulsion increased electronic conductivity by orders of magnitude. The benefits of increasing rather than decreasing pH is believed to be the result of how the particles' zeta potential varies with pH of an aqueous solution and the value of their isoelectric points. When pH increases, the positively charged alumina particles become negatively charged, repelling the carbon black, decreasing aggregative between active and conductive particles and both zeta potentials decrease [132,133].

Because the third condition for the WPI bath, dissolution of inert salt, produced mild effects on electrode formulation, the potential for synergistic interactions of increased temperature and pH to enhance electrode formulation was next explored. Figure 5-2C shows that the resulting electronic conductivity, obtained for a bath heated at 85ºC using different levels of alkaline pH, increases to a greater degree than when using modified temperature or pH conditions separately. In electrodes containing 2.5 wt% carbon black, conductivity increased by up to 167 times compared to electrodes immersed in room-temperature DI water.

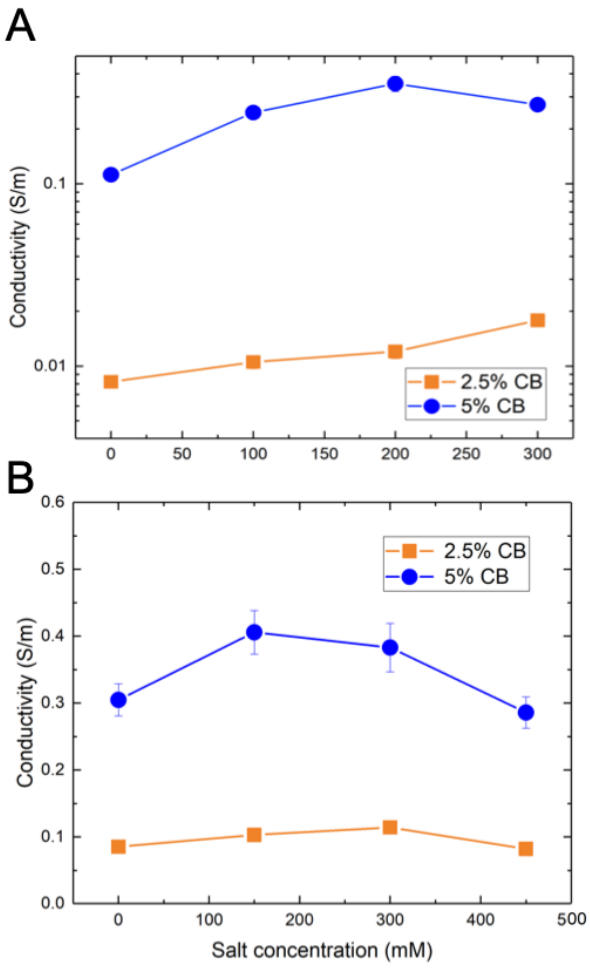

Figure 5-4: Electronic conductivity of alumina electrodes immersed in an 85°C DI water bath with increasing A) salt concentration and B) pH.

After increasing the conductivity of alumina films, the process was applied towards NVTP particles. Electronic conductivity of NVTP electrodes made with 5 wt% Ketjen black was 1.98 S/m. To obtain a slight increase in active particle loading without sacrificing conductivity, samples were made using 2.5 wt% Ketjen black and underwent wet-phase inversion in an 85°C at varying pH values, as this method showed the greatest improvement. The electronic conductivity of the electrodes was able to achieve 87% of the electronic conductivity with half the carbon content. In addition to the experiments with increasing bath temperature and pH reported in the main text, salt

concentration of inversion baths was also increased with the expectation that the Debye length would be shortened, weakening electrostatic repulsion between carbon particles. Conductivity was shown to increase over its value for electrodes in DI water, though too much salt caused conductivity to begin declining. This result is likely caused by carbon becoming so mutually attractive that it flocculates, rather than forming a branching network. Experiments combining high salt concentration and high pH were not attempted because their intended effects were thought to counteract each other based on DLVO theory: salt weakens electrostatic force while increasing pH strengthens it in a beneficial manner.

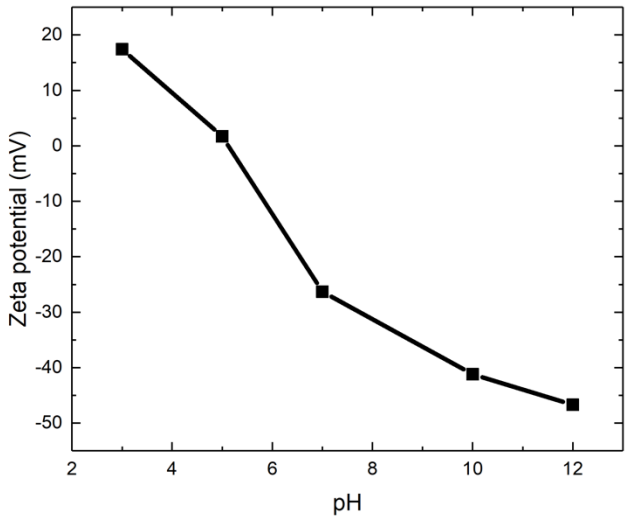

Figure 5-5: Zeta potential measurements for PBA particles dispersed in water at pH controlled by the addition of HCl or NaOH.

Figure 5-5 shows the variation of zeta potential with pH for PBA nanoparticles dispersed in water, measured using a Malvern zetasizer. Compared to carbon black zeta potential that decreases from to -24.5 to -40 mV over this pH range [132], the zeta potential of PBA nanoparticles decreased from -26.3 to -46.7 mV. In an alkaline bath, the PBA nanoparticles therefore repel the carbon 2.7x more strongly than at neutral pH, compared to the carbon particles repelling each other

2.5x as strongly, a slight advantage which causes preferential aggregation and increased conductivity.

5-5 Benefits of modified WPI and calendering

Following experiments were aimed at fabricating high conductivity, high areal-capacity PBA electrodes, predicated on the hypothesis that their use in FDI will increase salt removal. To fabricate PBA electrodes with high areal loading and low porosity I initially used my past WPI procedure from Chapters 1 and 2 (using a room temperature deionized (DI) water bath for phase inversion) to fabricate 250 μm thick electrodes that were subsequently calendered to lower thicknesses, yielding electrodes of varied porosity. Figure 5-6A shows the results for cycling of an electrode with different degrees of calendering using a 1M NaCl flooded cell with a graphite counter electrode and a Ag/AgCl reference electrode. These results indicate that as electrode thickness and porosity decrease, the rate capability of the electrode increases. Between rates of 2.6C and 10.3C, an uncalendered 250 μm electrode's utilization reduced 64%, while the same electrode calendered down to 72 μm showed only an 18% reduction in utilization and 34% greater capacity at 2.6C relative to 250 μm electrodes at the same rate. Returning to the lowest C-rate after cycling each sample at 10.3C confirmed that the capacity drops observed at high rate were not due to electrode degradation. Despite the concern of low porosity's correlation with increasing ionic resistance in porous electrodes [15,37], calendered electrodes showed no rate capability decrease due to lost pore volume. However, electrodes cast at thickness greater than 250 μm readily cracked when using conventional WPI, motivating search for improved electrode fabrication conditions.

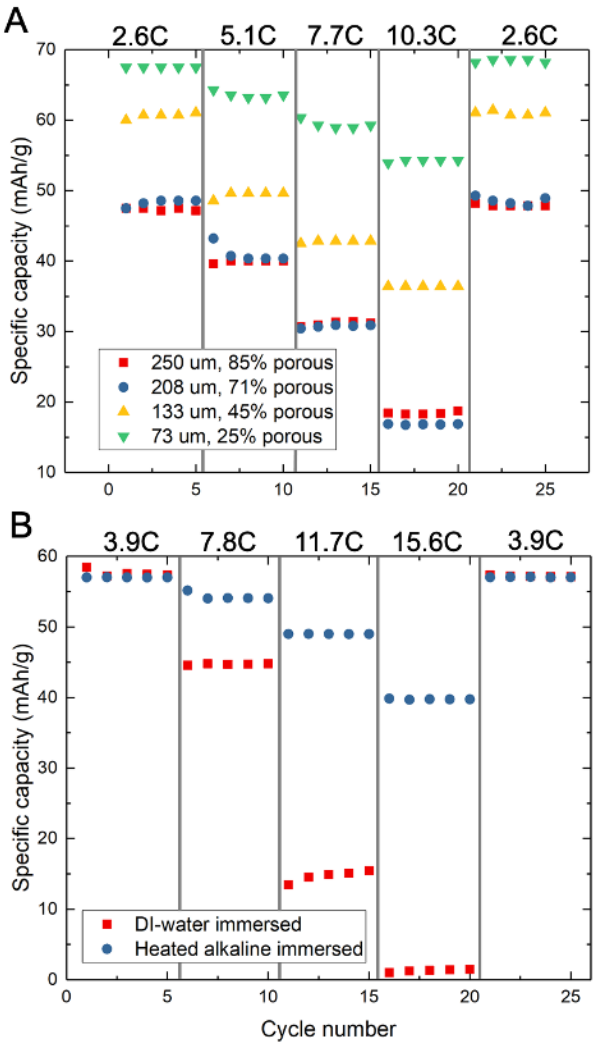

Figure 5-6: (A) Specific capacity for a PBA electrode fabricated with conventional WPI at different degrees of calendering at different C-rates. (B) Capacities of uncalendered electrodes fabricated with conventional WPI and 85ºC, pH 12 water immersed electrodes. All cycling experiments were performed in a 1M NaCl flooded cell.

To overcome areal loading limitations and increase electrode performance overall, colloidal interactions between particles in electrode slurry occurring during WPI processes were analyzed. The forces between active (PBA) and conductive (carbon black) particles during the formation of an electrode's microstructure are postulated to be controllable for the promotion of conductive particle aggregation and increase effective electronic conductivity. DLVO theory suggests that decreased conductor-active particle aggregation is achievable by conductors and

active particles having like-signed zeta potential, making them mutually. Furthermore, DLVO theory suggests that temperature affects electrostatic interactions. By altering the properties of the bath, it is shown that repulsive energy between carbon particles can be decreased while increasing the repulsion between carbon and active particles, causing more carbon to aggregate into a conductive backbone.

Accordingly, modified WPI experiments were performed on cast electrode slurries to characterize the effects of the temperature and pH of inversion baths on electronic conductivity, so as to modulate electrostatic colloidal interactions respectively via Debye length and zeta potential. To do this, slurries comprised of conductive particles (C45 carbon black) and surrogate particles replacing low-conductivity PBA (Al_2O_3) were formulated, as done in Chapter 2. Figures 5-2A and 5-2B show variations of electronic conductivity respectively with temperature and pH, where temperatures of 80-90ºC and pH 12 are shown to produce 2-3 times higher conductivity than the baseline case at room temperature and neutral pH when 5 wt.% carbon black is used. The changes in electronic conductivity observed among the different WPI conditions, despite containing the same constituent mass fractions, are reconcilable using DLVO theory of colloidal physics. Increasing pH causes zeta potential to decline for both particle phases, and a sufficient increase thereof can cause surrogate active particles to become negatively charged [133]. However, carbon black particles have been found to possess negative zeta potential at pH 7 [132], indicating that surrogate active particles and carbon black experience strong electrostatic attraction at pH 7. Because increasing pH beyond 7 cause carbon black particles to have increasingly negative zeta potential, carbon and surrogate active particles repel each other in alkaline solution. Additionally, increasing bath temperature gives carbon particles more kinetic energy to overcome

potential energy barriers, increasing the likelihood of carbon particle aggregation. Variations of the corresponding potential energy curves are presented to illustrate these concepts.

Informed by findings obtained with surrogative active material and C45 carbon black, WPI bath conditions that yielded highest electronic conductivity (85ºC and pH 12) were subsequently used to fabricate PBA electrodes containing Ketjen black conductor, for which previous work in Chapter 3 demonstrated improved electronic conductivity relative to C45 carbon black. Flooded cell cycling comparing WPI processes was performed, shown in Fig. 5-6B. The electrode immersed in a heated, alkaline bath showed superior rate capability compared to electrodes prepared using standard conditions, which is consistent with the results obtained with surrogate material that showed increased electronic conductivity under such conditions. In addition, the modified WPI conditions were shown to prevent cracking of electrodes with thicknesses as large as 320 μm, despite an electrode immersed in 85ºC, neutral pH water cracking at 320 μm. This finding confirms the critical role of bath pH in preserving the thick electrodes' mechanical integrity. Binder-solution interactions, such as the Hofmeister effect [134], are postulated to increase binder uniformity within electrodes and consequently increase mechanical strength.

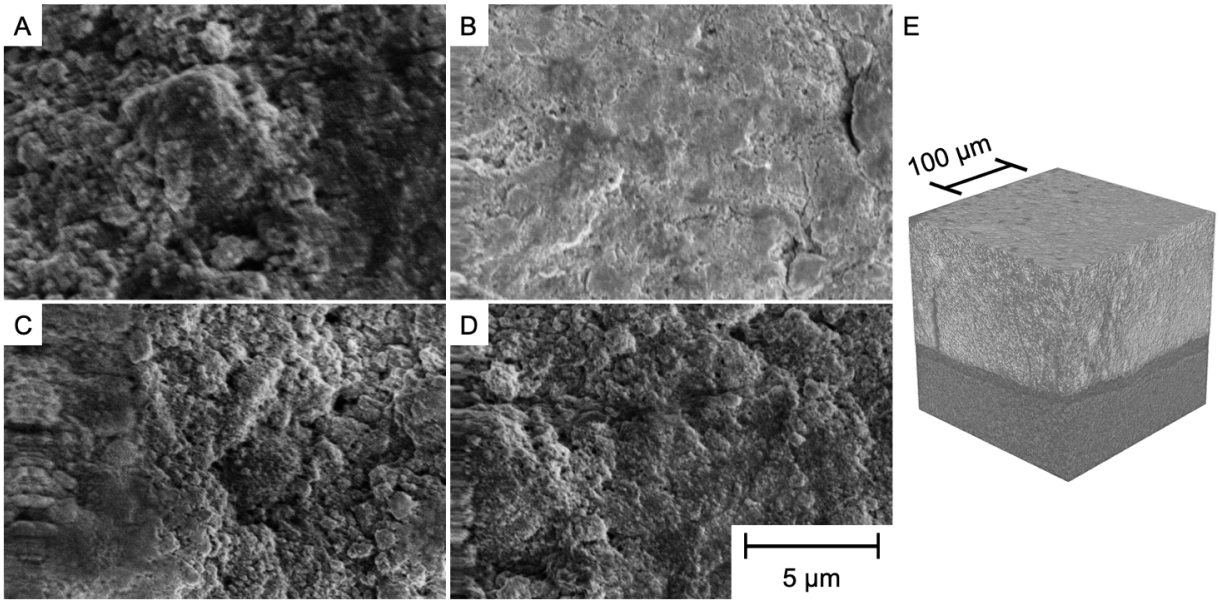

Figure 5-7: SEM Images of a conventional PBA electrode (A) before calendering and (B) after calendering. Images (C) and (D) show a heated, alkaline-bathed electrode before and after calendering, respectively. All four images use the same scale bar. (E) X-ray CT image of a calendered PBA electrode (light gray) prepared using the modified WPI process supported on graphite foil (dark gray).

To acquire visual evidence for the effect of electrode fabrication conditions on their microstructure, SEM images of DI water-immersed and heated alkaline-immersed electrodes were obtained (Fig. 5-7), including images taken before and after calendering to 50% of their initial thickness. While the microstructures of uncalendered electrodes prepared using conventional and modified WPI processes were indistinguishable (Figs. 5-7A and C), WPI conditions were shown to affect the texture of calendered electrodes substantially (Fig. 5-7B and D). Specifically, the conventional WPI process produced a relatively smooth and occluded calendered surface compared with the modified WPI process, consistent with the postulate that increased pH and temperature during WPI increases binder uniformity throughout electrodes. This observation is also consistent with the results of flooded-cell cycling which showed improved rate capability for electrodes prepared using the modified WPI process. Fig 5-7E shows an X-ray computed

tomography (CT) scan of a calendered electrode prepared by modified WPI, confirming the process yields a homogeneous distribution of PBA particles within the microstructure over a 200 μm by 200 μm area. However, a larger area of 620 μm by 790 μm reveals defective fissures constituting approximately 5% to 10% of the porous electrode's overall volume. To understand the impact of such fissures, these electrodes' hydraulic permeabilities were measured using a simple gravity-driven apparatus described in Chapter 3. The densest calendered electrodes had a permeability of 0.23 μm^2 compared with the uncalendered electrodes' 1.38 μm^2 due to their decreased porosity and average micropore radius. This finding indicates that flow is forced through the microporous regions of these electrodes and is therefore not "short-circuited" through defective fissures. These results for electrode microstructure, flooded cell cycling, and electronic conductivity motivated use of the modified WPI process and electrode calendering with CIMs in an FDI cell.

5-6 Conclusions

It was discovered that principles of colloidal physics, particularly the DLVO theory of inter-particle forces, are applicable to battery electrode slurries and can be used to improve performance through increasing electrode conductivity. Modifications to the WPI technique of solidifying electrodes were tested, including heating the bath, increasing bath pH, and increasing bath ionic strength. Using DLVO theory, it could be inferred what kind of changes would occur, including the strength of inter-particle forces and the likelihood of two carbon particles becoming strongly attracted to each other. Tests with slurries containing alumina pseudo-active particles showed up to two orders of magnitude increase in electronic conductivity through the use of modified wet-phase inversion baths combining heated water with increases in pH.

PBA electrodes immersed in a heated alkaline bath were cycled in a flooded cell to compare performance with electrodes immersed in room-temperature DI water. Compared to the latter electrodes, the electrodes immersed in the heated alkaline bath displayed greater utilization at higher current densities. Calendered PBA electrodes were also tested in a flooded cell to confirm their improved rate capability compared with uncalendered electrodes. Like the electrodes immersed in a heated alkaline bath, this process was not shown to damage the electrodes, motivating the combination of these techniques in subsequent desalination experiments. This performance combined with excellent mechanical stability of heated alkaline-immersed electrodes led to them being used in subsequent desalination experiments.

CHAPTER 6: FARADAIC DEIONIZATION WITH RECIRCULATING FLOW

6-1 Improving desalination performance with recirculation

Prussian blue analogues (PBAs) show great potential for low-energy Faradaic deionization (FDI) with reversible Na-ion capacity exceeding 4 mol/L in the solid-state. However, past continuous-flow demonstrations using PBAs in FDI were unable to desalinate brackish water to potable levels using single-pass architectures. Here, recirculation of effluent from a symmetric cation intercalation desalination cell into brine/diluate reservoirs is shown to enable salt removal exceeding 80% at thermodynamic efficiency as high as 80% when cycled with 100 mM NaCl influent and when controlled by a low-volume, automated fluid circuit. This exceptional performance is achieved using a novel heated, alkaline wet phase inversion process that modulates colloidal forces to increase carbon black aggregation within electrode slurries to solidify crack-free, high areal-capacity PBA electrodes that are calendered to minimize cell impedance and electrode porosity. The results obtained demonstrate the need for co-design of auxiliary fluid-control systems together with electrode materials to advance FDI beyond brackish salinity.

The configuration of electrolyte flow through porous electrodes [10,11,23] and charge transport within porous electrodes [77] are known to affect rate capability and energy consumption in FDI using symmetric CIM electrodes, but past results suggest that unknown mechanisms remain and prevent salt removal potential of CIMs from being accessed in FDI. In FDI, saltwater can flow through a gap between electrodes in a flow-by configuration, or directly through the porous structure of electrodes sandwiched within a cell in a flow-through configuration. Flow-through electrodes incorporating Prussian blue analogue (PBA) CIMs, demonstrate in Chapter 3, have shown improved salt removal [10] charge utilization, [10,11,23], and specific energy consumption

[10,23] compared to flow-by PBA electrodes due to charge-efficiency loss at electrode/channel interfaces in flow-by [10,11] and smaller ohmic drop in flow-through [23]. Further, experiments introducing flow-through FDI achieved rapid salt removal with one order of magnitude lower specific energy consumption provided by judicious choice of electronically conductive additives inspired by experiments in Chapter 3 demonstrating that nanoparticle agglomeration limits transport in electrodes containing PBA CIMs [77]. However, charge efficiency diminished at higher C-rates due to low utilization shortening cycle time, an effect that complementary modeling indicated was likely a result of strong salt concentration gradients in both the streamwise and transverse directions within porous electrodes.

Along those lines, past modeling in Chapter 3 revealed that streamwise salt concentration gradients in feedwater result in streamwise state-of-charge gradients in CIMs within the porous electrodes through which feedwater flows [11]. While such state-of-charge gradients lead to efficiency loss and decreased CIM capacity utilization, it was predicted that recirculation of feedwater can minimize such deleterious effects [11]. While recirculation eliminates the coupling between flow rate and salt removal which constrained single-pass architectures, past studies [24,25,135] provided limited detail concerning the approaches used to repeatedly cycle feedwater through a single two-electrode FDI cell, and such studies only demonstrated a cumulative salt removal as high as 40 mM[135]. Along similar lines, others have flowed feedwater in series through flow compartments in an electrodialysis (ED) stack, while only reducing the salinity of 25 mM influent by 30% [13]. The development of novel high-capacity electrode materials for electrochemical desalination including CDI and ED has been regarded as unable to significantly reduce energy consumption compared to RO [136]. However, improvements achieved in FDI through reduction of concentration gradients, increasing electrode conductivity, and development

of control systems optimizing salt removal are shown here in conjunction. Accordingly, an automated multi-pass FDI architecture using recirculation from brine and diluate reservoirs is demonstrated and detailed for the first time, enabled by custom, low-volume valves and a low-cost Arduino control system. Beyond such effects, the porosity of flow-through FDI electrodes can be engineered to increase degree-of-desalination in flow-through FDI cells. Mass balance on a representative volume element of a porous electrode with porosity ε and CIM volumetric loading ν suggests that decreasing porosity from as-cast values of 85% to 67% could increase degree-of-desalination by over three-fold,[1] which is conceivable by calendering electrodes.

A brief outline of this chapter follows. The novel wet phase inversion process and the effects of electrode calendering discussed in Chapter 4 were used in conjunction to fabricate electrodes with low porosity, high areal capacity, and high rate capability. Results for the cycling of such electrodes in FDI desalination experiments are then presented. In such experiments a custom lab-scale recirculating FDI cell is employed to alternate flow paths such that feedwater in one reservoir continuously desalinates while another reservoir simultaneously concentrates. After several cycles using the densest electrodes, the diluate reservoir reached 90% salt removal from 100 mM NaCl influent before reaching a limit caused by desalinated and concentrated effluent mixing reducing charge efficiency. The use of denser electrodes is further shown to decrease energy consumption, achieving 80% thermodynamic energy efficiency (TEE) at 80% salt removal.

[1] Neglecting volume within electrodes comprised by conductive additives and binder and assuming perfect transmission of solution through porous electrodes, the maximum cation concentration change within solution $(\Delta c)_{soln}$ that could be effected by transferring such cations into a CIM with a reversible cation concentration $(\Delta c)_{solid}$ is given by $(\Delta c)_{soln}/(\Delta c)_{solid} = (1-\varepsilon)/\varepsilon$.

6-2 Electrode fabrication, conductivity measurements, and flooded cell characterization:

PBA nanoparticles and associated slurries were prepared as in previous work [77] with electrodes composed of 85 wt% nickel hexacyanoferrate (NiHCF) PBA, 5 wt% EC-600JD Ketjen black, and 10 wt% Solef polyvinylidene fluoride (PVDF) binder. The first electrodes were cast at 150 μm thick onto 100 μm thick 2010A high-purity graphite foil current collector (Ceramaterials), and subsequent electrodes were cast at higher thicknesses of 250 μm and 320 μm as described in the Results and Discussion Section. After being cast and solidified using wet phase inversion (WPI, as described subsequently), the electrodes were calendered using an MTI roll press to a targeted thickness of 150 μm, as measured by an MTI thickness gauge. Porosity was then calculated from the densities of the total electrode and its solid constituents, $\varepsilon = 1 - \rho_{electrode}/\rho_{solid}$. Electrochemical cycling of these electrodes was performed at several C-rates in a 1M NaCl flooded cell versus a Ag/AgCl reference electrode with a graphite counter electrode.

WPI is used to solidify electrodes after casting. Here, an as-cast slurry film supported on a current collector is immersed in a water bath to displace n-methyl-2-pyrrolidone (NMP) solvent and solidify the PVDF binder dissolved therein to form a mechanically stable electrode. While previous WPI processes used room temperature deionized water baths for phase inversion, modified bath conditions to improve electrode performance were explored. Initial tests were done using 1 μm Al_2O_3 particles (AdValue Technology) as a surrogate for PBA material due to supply limitations for the latter material, as in previous work optimizing electrode conductivity without calendering. As Timcal Super C45 carbon black (MTI) had previously been shown to be an inferior conductive additive compared to Ketjen black, C45 was used in initial studies with the expectation that improvements in conductivity would be more obvious than with Ketjen black. To

measure the electronic conductivity of electrodes, slurries were cast onto an insulative PTFE substrate, and conductivity was measured using an in-house built four-point probe discussed in Chapter 2.

To influence the inter-particle forces in slurries, a 200 mL WPI water bath was used to explore the effects of three different experimental parameters: (1) using a hot plate to heat the water between 25°C and 85°C, (2) increasing pH of the bath from 7 to 12 by adding NaOH, and (3) increasing salt concentration by dissolving NaCl up to 450 mM. PBA electrodes immersed in the high pH bath also displayed structural stability when cast at high thickness, solidifying at 320 μm when an electrode that thick would normally crack during drying if phase inverted using a room temperature, neutral pH water bath.

6-3 FDI system design and control:

The custom built FDI cell used in Chapter 3 was employed for desalination experiments in conjunction with a custom fluid circuit built around it to recirculate flow (see Fig. 6-1). The FDI cell used a PBA anode and cathode separated by a Neosepta AMX anion exchange membrane (Astom Corp). In all desalination experiments two test tubes were filled with 5 mL of saltwater to be converted to brine and diluate during cycling, with initial concentrations of 100 mM, or 200 mM in the final experiment. To direct flow, an Arduino controller actuated four servos to pinch branching paths of rubber tubing, ensuring that feedwater from only one reservoir flowed through either side of the FDI cell. Flow rates of both effluent streams were kept constant and equal by using a Masterflex peristaltic pump, and all experiments used a flow rate of 1 mL/min. This flow rate is 4x higher than previous experiments with a single-pass system to take advantage of the recirculation, keeping concentration gradients low, as complete desalination over one pass is

unnecessary. With the diluate and brine flow rates being equal, the water recovery rate in all experiments was 50%. Images of the cell's complete design, details of its fluid circuit. Salt concentration at the two inlets and two outlets was measured using four custom-built flow-through conductivity sensors connected to an eDAQ Quad Multi Function isoPod which recorded conductivity using the program PodVu.

6-4 Desalination experiments

All desalination experiments used a current density of 1 mA/cm^2 applied to 2.5 cm^2 electrodes by a Biologic VMP-3 potentiostat over a voltage window of +/- 0.45V. Based on the measured values of hydraulic permeability, pressure drops across the FDI cell of 71.6 kPa and 430 kPa, respectively, for cycling with the least and highest areal-capacity electrodes tested here at a 1 mL/min flow rate. The time delay between OC starting and IV actuation was set to 20 seconds in all FDI experiments, roughly twice the duration of the time delay between IV and OV actuation, to uniformize concentration on the respective sides of the cell. During the OC period before IV actuation, electrochemical impedance spectroscopy (EIS) tests were performed with frequencies ranging from 100 kHz to 100 mHz to study how impedance changes from cycle to cycle. Lower frequencies were not tested because doing so would excessively prolong experiments. The time delay between actuation of IVs and OVs was different for each electrode pair and was calculated using a calibration process described in section 6-4. Prior to each experiment, the conductivity probes used were calibrated with the initial 100 and 200 mM influent, known to respectively have a conductivities of 1.067 and 2.034 S/m at 298K [63].

Two 'pause periods' were introduced during the open circuit phase of FDI cell cycling in order to independently time the valve actuation events for inlet and outlet valves, so as to minimize

mixing of the diluate and brine streams. The first pause occurs between the start of the open-circuit period at the end of a given half-cycle and the switching of the inlet valves, allowing time for effluents to move from within the electrode to their appropriate reservoir. The second pause occurs between the events for switching of the inlet and outlet valves, and this pause provides time for brine and diluate streams to flow into the opposing side of the FDI cell from the previous half cycle. It was found that, if all valves are switched simultaneously upon a given half-cycle's end, charge efficiency is reduced in proportion to the internal volume of the cell as a result of the brine and diluate within the electrodes and connective tubing flowing into their opposing reservoirs, undoing desalination progress. With electrode porosity and the internal dimensions of the fluidic circuit known, an effective internal volume of 87 µL was calculated for uncalendered 150 µm electrodes, resulting in that volume of fluid flowing into the wrong reservoir if such valve-actuation conditions were naively utilized.

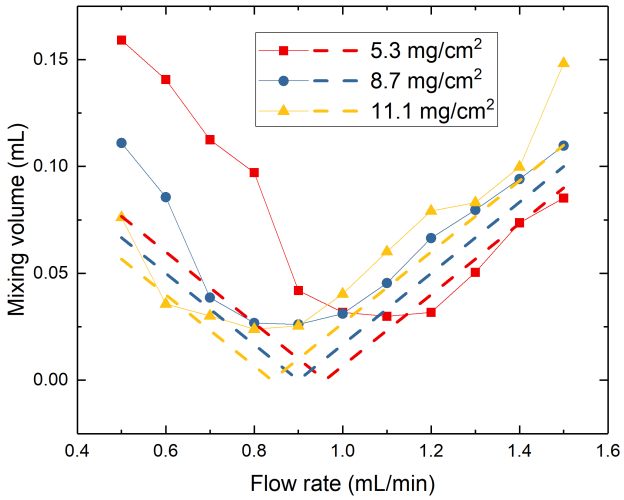

Figure 6-1: Curves used for calibrating the pause period in the three pairs of electrodes used in experiments, showing a minimum value for mixing volume. Dashed lines indicate ideal theoretical mixing in each pair of electrodes.

To overcome such limitations, the timing of valve actuation events was calibrated in the following way. The durations of the second pause were calculated for each electrode pair by fixing

the associated time delay to 10 s and subsequently calculating the apparent mixing volume when flowed at rates ranging between 0.5 to 1.5 mL/min, beginning with a reservoir containing 100 mM salt water and a second containing deionized water. The apparent mixing volume V_{mix} was calculated according to measured changes in reservoir 1's concentration Δc before and after switching events, $(c_1 - c_2)V_{mix} = \Delta c V_{res}$. The flow rate that showed the least mixing was used to find the pause period for 1 mL/min. For example, in Fig. 6-1, for the 5.3 mg/cm^2 electrode with a 10 second pause the flow rate with the least mixing was 1.1 mL/min, then in an experiment with a flow rate of 1 mL/min the pause period should be 11 seconds. The dashed lines in Fig. 6-1 represent ideal theoretical mixing in which the boundary between the brine and diluate is discrete, ignoring any dispersion or diffusion effects, which qualitatively agree with experimental measurements. Due to the reduction in porous volume, denser electrodes require shorter pause periods for a 1 mL/min flow and had lower mixing volumes, with deviations above or below the optimal choice increase the mixing volume.

6-5 Recirculating FDI desalination performance

FDI experiments were conducted using an in-house custom-built flow cell and integrated fluid recirculation system (Figs. 6-2A through 6-2D). Valves at the outlets (OVs) and inlets (IVs) of both electrodes direct salt water respectively to and from the reservoirs for brine (BR) or diluate (DR), as shown in Figs. 6-2B and 6-2C. Figure 6-1E shows the corresponding variations of cell voltage and influent salt concentrations with time, the latter measured by conductivity probes at the inlet regions of both electrodes when the cell is subjected to galvanostatic cycling with either positive (PC) or negative (NC) current, followed by a brief open-circuit (OC) period. In addition to constructing the cell with the lowest internal volume possible using narrow inner diameter

tubing and custom parts dimensioned to minimize volume, experiments were conducted to optimize valve timing to reduce mixing between diluate and brine streams. Pause periods were added at the end of each PC/NC period, minimizing mixing by taking evacuation time of the system's internal volume into account. Hence, Figure 6-2E shows a finite-time delay between switching events of electrical current and both IVs and OVs, denoted as 'IVs switch' and 'OVs switch.' After calibrating such events, salt concentration was observed varying linearly with time during initial cycles, and salt removal per cycle declines during successive cycles due to diluate and brine effluent streams mixing.

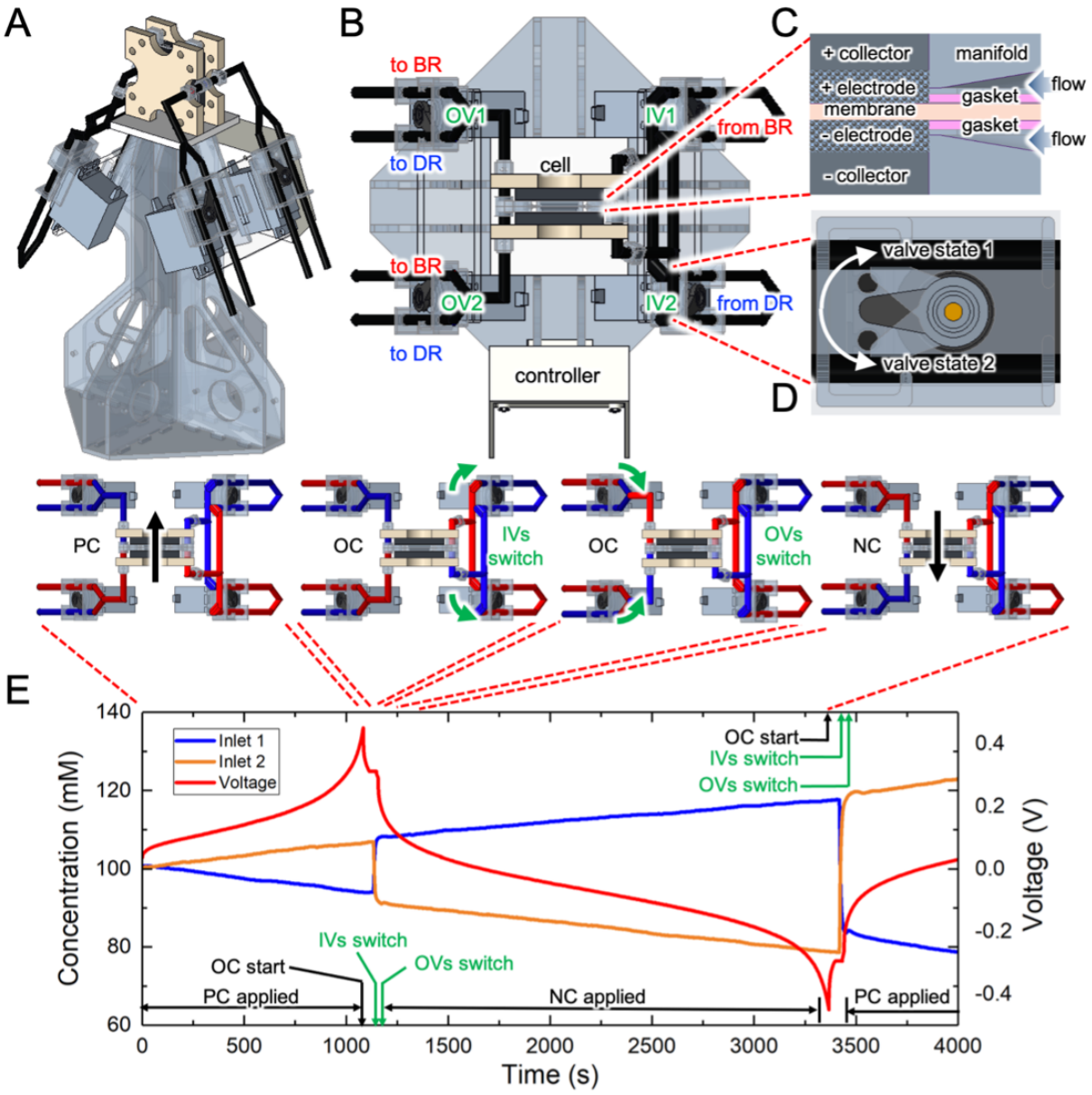

Figure 6-2: (A) Trimetric and (B) top views of the present recirculating FDI system incorporating inlet valves (IVs) and outlet valves (OVs) that direct fluid to/from electrodes from/to a brine reservoir (BR) and a diluate reservoir (DR). Detailed views (C) of the cell's inlet region showing PBA symmetric electrodes sandwiching an anion exchange membrane (AEM) and (D) of valve switching actions. The time sequence of cell voltage and salt concentration used to conduct one complete cycle is shown using inset diagrams together with the timing of valve and current switching events controlled automatically. PC, OC, and NC respectively denote positive current, open circuit, and negative current.

Using this apparatus with the electrical/fluidic cycling sequences already described, of PBA electrode formulation on FDI performance was explored. As a point of reference, use of this recirculating FDI apparatus with electrodes having the same formulation, porosity (85%), and areal loading (5.3 mg-PBA/cm^2) as in Chapter 4 yielded 65% salt removal from 100 mM NaCl solution, in contrast with <27% salt removal in the previous single-pass experiments. Electrodes cast at 250 μm thick were then tested, solidified with WPI using room-temperature DI water, and calendered to 150 μm thick, yielding 8.7 mg-PBA/cm^2 and 75% porosity. The corresponding experiments produced 80% salt removal, owing to the increased capacity and reduced mixing volume between brine and diluate effluent in the denser electrode. The third pair of electrodes was first cast and solidified by WPI in 85°C water with pH 12, resulting in a 320 μm electrode that was subsequently calendered down to 150 μm, yielding 11.1 mg-PBA/cm^2 and 67% porosity. This further increase of areal loading and decrease of porosity produced a maximum salt removal of 90% from 100 mM influent, corresponding to a productivity of 3.3 L/hour-m^2. A final test using 200 mM influent with the 11.1 mg-PBA/cm^2 electrodes was performed, expecting the higher sodium ion availability and increased ionic conductivity would lead to higher active material utilization. Because the electrodes removed more salt per half-cycle, 104 mM was removed from the 200 mM influent before becoming limited by mixing.

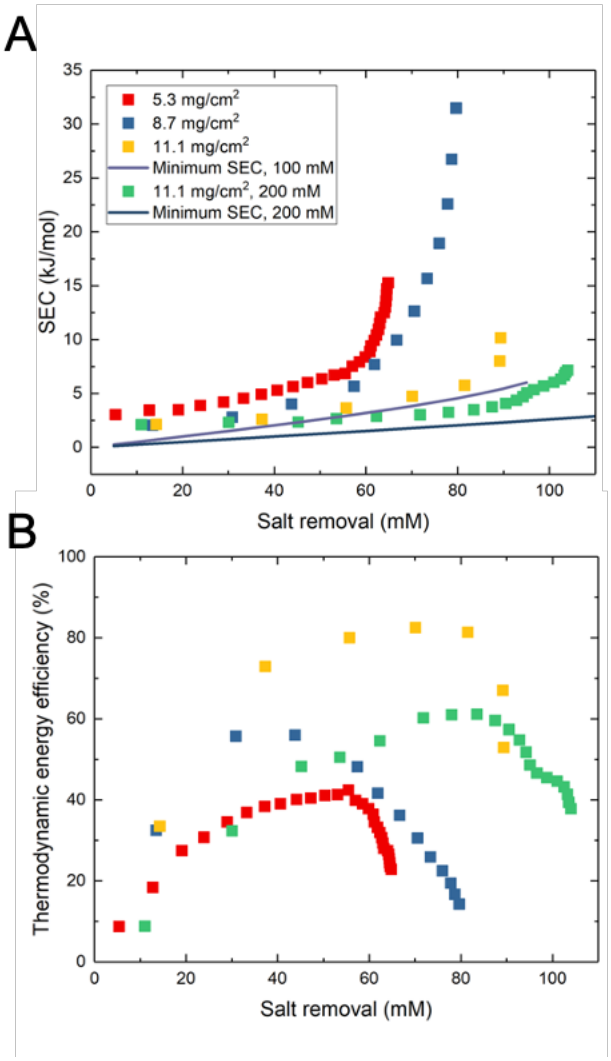

Figure 6-3: (A) SEC versus salt removed from the diluate reservoir. The thicker the electrodes are, the greater the concentration change after each cycle due to the extended desalination time and fewer mixing opportunities during switching. (B) Thermodynamic energy efficiency for the three electrode pairs.

These high salt removals, achieved using different electrode densities, yielded different levels of specific energy consumption (SEC) to reduce influent concentration c_i to diluate concentration c_d, as shown in Fig. 6-3A, calculated by the equation $SEC = E_{total}/(c_{i-}c_d)\forall_{resevoir}$. These SEC values are calculated based on the cumulative energy invested and the cumulative salt removal achieved, rather than using the energy invested and salt removed per cycle. Due to the high electronic conductivity and active particle loading of electrodes produced

by the modified WPI process, the FDI system achieved excellent salt removal at an SEC that approaches the thermodynamic minimum separation energy, $SEC_{minimum} = 2RT\left(c_d ln(c_d) + \left(\frac{1}{\gamma} - 1\right)c_b ln(c_b) - \frac{c_i}{\gamma} ln(c_i)\right)/(c_i - c_d)$ where γ is the water recovery rate of 0.5 and c_b is brine concentration. As shown later, decreased energy consumption with increased electrode density is supported by its low ohmic resistance (see Fig. 6-5A and discussion thereof). Previous work using the same cell operating at the same current density (1 mA/cm^2) in single-pass mode in Chapter 3 showed a simulated SEC of 2.7 kJ/mol, while the 5.3 mg/cm^2 electrodes sharing the same composition have an initial SEC of 3.04 kJ/mol. As the present system reached the limit of salt removal due to the mixing of diluate and brine, further cycling consumed significantly more energy, causing SEC to rise steeply while salt removal stagnated. Because all experiments used the same flow rate and current density, the average salt absorption rate (ASAR) was initially 0.55-0.6 μmol/cm^2-min for all three experiments. ASAR declines with the mixing effect decreasing removal each cycle, becoming 0.51 μmol/cm^2-min on average when the experiment with 11.1 mg/cm^2 electrodes concluded.

At the highest salt removal with 100 mM influent, the thermodynamic energy efficiency (TEE) of the recirculating cell, defined as $TEE = SEC_{minimum}/SEC$, was 50%, but TEE reached as high as 80% for the densest electrodes before mixing outweighed the electrodes' ability to remove salt in a single cycle (Fig. 6-3B). One reason for the high TEE is the high salt removal shown in Fig. 6-3A, where SEC for all three electrodes increases linearly with salt removal during early cycles. At low salt removal, the thermodynamic minimum is low compared to the experimental SECs, but as both experimental and theoretical SECs increase the ratio between them increases as well. The present 100 mM influent is more ionically conductive than the 20-50 mM

influents used in other studies, and the denser, highly conductive electrodes created here consume less energy likely due to smaller ohmic losses shown subsequently. It should also be noted that the cell operated at only 1 mA/cm^2, and SEC for similar electrodes increased approximately linearly with current density seen in Figure 4-4A.

While such results demonstrate the practical benefits of high areal loading for increased desalination performance, inspecting specific capacity attained cycle-to-cycle revealed trends that suggest further room for improvement. Fig. 6-4A shows that utilization of charge capacity declined with increasing salt removal, though high areal capacity electrodes retain the most capacity. When comparing the 8.7 mg/cm^2 and 11.1 mg/cm^2 electrodes, the former electrodes only utilize 45% of their capacity at 80% salt removal, while at the same salt removal the latter electrodes retained 87% utilization. This outcome is likely a result of high areal-capacity electrodes producing greater *flow efficiency*, the ratio between time for the electrodes' porous volume to be replaced and the charging time [71]. Because denser electrodes have smaller pore volume, feedwater is removed fast enough to supply fresh sodium ions for intercalation into PBA particles, and between the lowest and highest areal loadings, flow efficiency increases by a factor of 2.6. The specific capacity of electrodes during experiments with 200 mM remained high even when the cell reached the limits of its salt removal due to the abundant sodium ions. Though the flow rate was four times higher than what previous single-pass experiments used in Chapter 3 (0.25 mL/min), decreasing charge capacity at high salt removal suggests that gradients of salt concentration and PBA state-of-charge decrease utilization. However, the disparate concentrations of salt in diluate and brine streams near the end of FDI process are also expected to produce concentration polarization and ohmic polarization limiting capacity when performing galvanostatic cycling within a finite cell voltage window. The system's inability to continue removing salt also causes charge efficiency to

decline, shown in Fig 6-4B, eventually reaching zero. During a single half-cycle, charge efficiency remains 80-95% as salt is continuously removed, but cumulative charge efficiency becomes zero due to mixing counteracting salt removal.

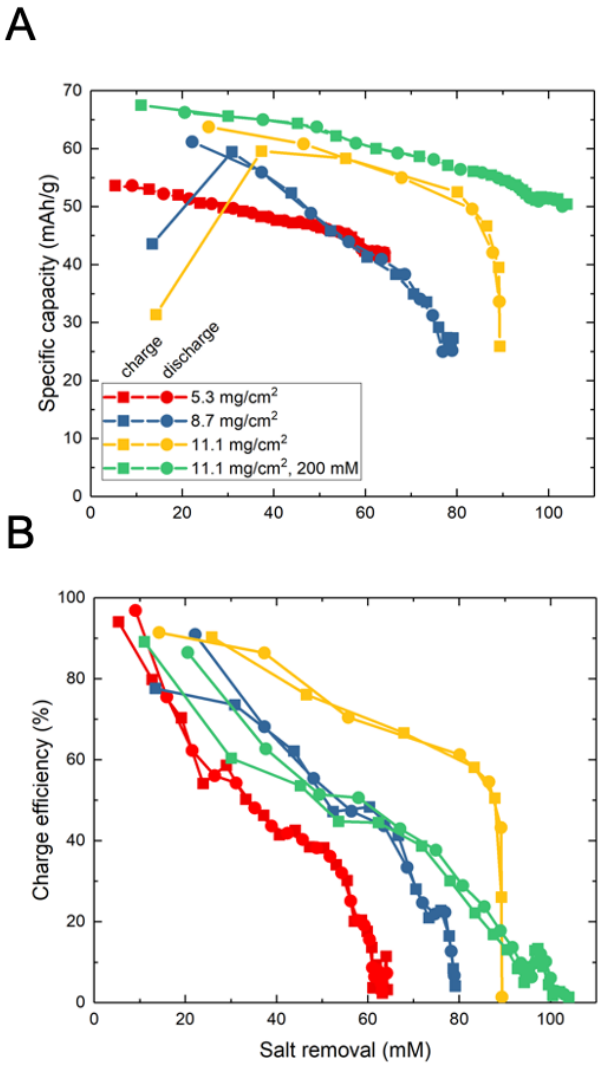

Figure 6-4: (A) Specific capacity during charging and discharging versus the salt removed from the diluate stream. Initial data points for charging appear low because the electrodes were already partially charged before the experiment began. (B) Charge efficiency versus salt removed from the diluate stream for the same experiments.

To analyze the influence of cell impedance on desalination performance, electrochemical impedance spectroscopy (EIS) was conducted during the open circuit (OC) periods of each cycle

(Fig. 6-5A). These spectra showed that real impedance at high frequency gradually increases from cycle-to-cycle, as a result of one side of the cell becoming less ionically conductive during salt removal. This effect is evidenced by the voltage versus capacity curves measured during PC and NC cycling (Fig. 6-5B), where increased polarization pushes average cell voltage nearer to the edges of the voltage window within which cycling occurs. From the initial cycle to the final cycle, the degree of polarization increase differs with each type of electrode and the final salt removal attained. However, polarization is largest during cycles with the highest salt removals, and when real impedance at high frequency is largest.

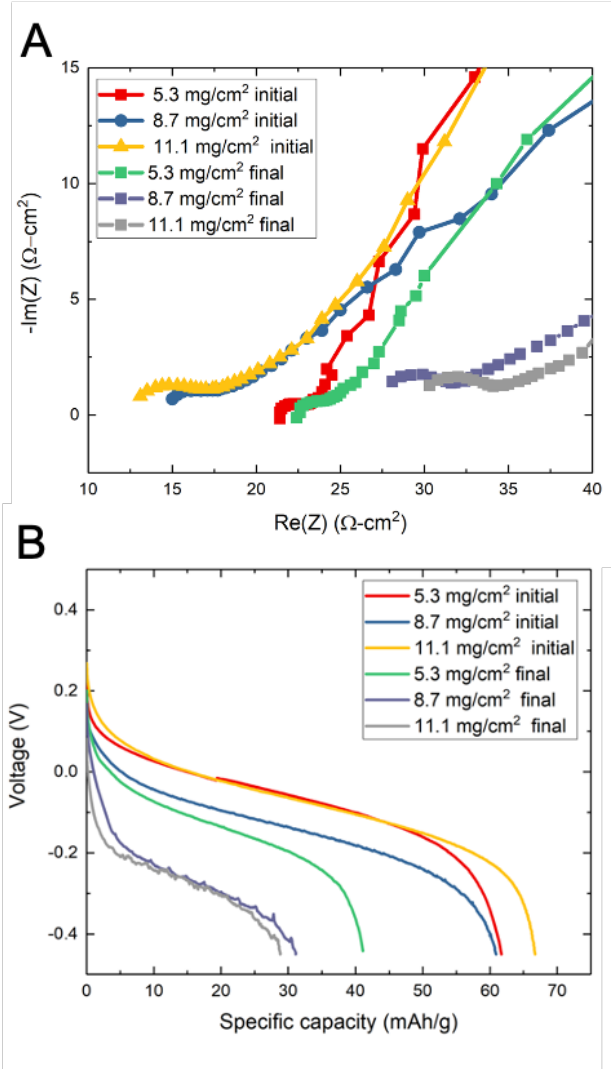

Figure 6-5: (A) EIS curves for the three pairs of electrodes following the initial and final half-cycles of each experiment. The more densely calendered electrodes are noted to show lower real impedance at high frequencies. (B) Voltage versus specific capacity curves for the initial discharging and the final charging half-cycles of the three electrode pairs, showing diminishing utilization and increasing polarization at high salt removal. For ease of viewing the polarization differences, the final charging curves were made to have a negative sign.

In Fig. 6-5A electrodes with 5.3 mg/cm^2 show little change in real impedance between the first and final cycles, despite attaining 65% salt removal. However, real impedance at high-frequency in the denser electrodes increased more than two-fold. This limited change of impedance for electrodes with lower areal capacity can be understood by assuming that ionic conductivity is

directly proportional to salt concentration. Equation 6-1 shows the theoretical ratio between ionic resistance at a certain concentration difference $R_{ion}(\Delta c)$ and the initial resistance when both anode and cathode contain influent of the same concentration, neglecting the intervening AEM.

$$\frac{R_{ion}(\Delta c)}{R_{ion}(t=0)} = \frac{1}{2}\left(\frac{1}{1-\frac{\Delta c}{c_0}} + \frac{1}{1+\frac{\Delta c}{c_0}}\right) \qquad (6-1)$$

This simple relation reveals that only at 71 mM of salt removal from 100 mM does the theoretical ionic resistance double. Furthermore, ionic resistance within electrodes is only one source of impedance, including electronic resistance, Warburg impedance, AEM impedance, and contact resistances in external circuitry. In any case, the increasing impedance with increasing salt removal is visible in Fig. 6-5B's cell voltage curves. Average voltage during the first and final half-cycles increased from 0.07V to 0.29V as the 11.1 mg-PBA/cm^2 achieved 90% salt removal, lowering utilization and limiting maximum salt removal. Calendering electrodes increased electronic conductivity and reduced ohmic energy losses, keeping energy consumption low for a high salt removal.

Finally, Table 6-1 compares energy consumption achieved recently in FDI using symmetric electrode architectures. As each work tested an FDI system at different current densities and flow rates, the particular values shown are for the highest salt removal achieved. The present work operated at a slightly higher ASAR than most cases and achieved an excellent 90% salt removal, a higher fraction than any other listed. The final SEC of 10.9 kJ/mol is also high due to the mixing effect. However, at 80% salt removal an SEC of 5.7 kJ/mol was achieved, approaching the thermodynamic minimum energy of 4.5 kJ/mol for that salt removal level and reaching record level of thermodynamic energy efficiency of 80%.

Table 6-1: Comparison of performance among symmetric FDI systems, including SEC, ASAR, and the percent salt removed from each study's initial concentration. MHCF compounds denote different Prussian blue analogue materials using a certain inactive transition metal M in its lattice, while AEM and CEM denote anion and cation exchange membranes, respectively. Values in parentheses indicate those obtained at optimal thermodynamic energy efficiency (TEE), whereas the remaining values are shown for those obtained at maximum salt removal.

SEC (kJ/mol)	ASAR (μmol/cm^2-min)	Influent salinity (mM)	Diluate salinity (mM)	% Salt Removal	Active material and separator	Other comments	Ref. no.
10.9 (5.7)	0.51	100	10 (20)	90 (80)	NiHCF/AEM /NiHCF	parallel flow-through; recirculating	this work
7.16	0.46	200	96	52	NiHCF/AEM /NiHCF	parallel flow-through; recirculating	this work
18.0	2.73	100	73	27	NiHCF/AEM /NiHCF	parallel flow-through	Chapter 3
10.1	0.45	20	17.5	12.5	carbon/CEM /carbon	transverse flow-through; carbon cloth modified with silane groups	[22]
6.44	0.31	477	286.2	40	NiHCF/AEM /FeHCF	no flow	[26]
2.4	0.34	25	17.5	30	CuHCF/AEM/ CuHCF	flow-by	[13]
5.6	0.25	500	400	20	NiHCF/CEM/ AEM /CEM/FeHCF	Nafion-coated particles, flow-by divided by membranes	[137]
27.0	6.2	500	100	80	Ag/CEM /AgCl	no flow	[27]
13.76	0.534	50	35	30	CuHCF/AEM/ CuHCF	parallel flow-through	[23]
21.1	3.85	50	41.7	16.7	BiOCl/CEM /BiO	parallel flow-through	[24]
23.04	0.104	20	15	25	NiHCF/AEM /NiHCF	recirculating	[25]

The electrical energy consumption is exceptional for the amount of salt removed, but it must be noted that the calculated TEE does not take pumping into account. Pumping power remains significant, approximately 0.12 kWh/m^3 for the lowest permeability electrodes. However, this is the energy consumed for each pass of water, and over the course of the desalination process, this energy consumption is multiplied by over 50x due to the same volume of fluid being continuously recirculated, causing the pumping to expend an order of magnitude more energy than the applied current. Thus, pumping power should be targeted as another area for improving FDI performance. These results motivate other approaches to minimize losses that arise due to such effects, including scale-up of the FDI cell.

6-6 Conclusions

A recirculating flow-through Faradaic deionization apparatus was demonstrated and shown to produce 90% salt removed from one reservoir of 100 mM aqueous NaCl, transferring the salt into a second reservoir of brine with 50% water recovery rate. In the same experiment, 80% salt removal was achieved with a TEE of 80%. It was shown that the recirculating cell's performance is limited by the diluate and brine mixing during the switching process, the effects of which were minimized through the use of an open-circuit period during which valves at the inlets and outlets of electrodes were switched at different times. Such pause periods improved performance relative to preliminary tests, however they could not totally eliminate mixing effects, resulting in an upper limit for salt removal and a lower limit for specific energy consumption that is highest for porous cation intercalation electrodes with high areal capacity and low porosity.

Electrodes were fabricated using a novel wet phase inversion process incorporating a heated, alkaline water bath to solidify electrodes with high areal capacity that were subsequently

calendered to achieve simultaneously low porosity. Impedance spectra measured during the open-circuit periods of FDI cycling showed that the electronic resistance of electrodes was reduced by their calendering, and flooded cell experiments showed better utilization. Despite the significant improvements demonstrated relative to prior work, limitations other than electrode areal capacity make further increases in salt removal unattainable for the current cell even with the present recirculating apparatus. For example, reducing the ratio of internal fluid volume to the pore volume of electrodes is likely to lead to further improvements in desalination performance, so as to further decrease the effect of mixing between brine and diluate streams.

The current FDI cell possesses pore volume, when incorporating the lowest porosity electrodes tested (67%), that is 70% of the total volume within tubing and manifold supplying influent to the electrodes. An FDI cell with increased capacity – constructed using more electrode area with similar areal capacity – would increase total electrode pore volume in proportion to cell capacity, while holding tube volume constant. However, the degree of apparent mixing is likely to include the effects of diffusion and dispersion at interfaces between diluate and brine streams. Pumping energy with the densely calendered electrodes is also excessive compared to the electrical energy, a problem which will be studied in Chapter 7.

CHAPTER 7: SCALED-UP RECIRCULATING FDI CELL WITH INTERDIGITATED MACRO-PORES

7-1 Interdigitated patterning of electrodes

As demonstrated in Chapter 2, it is possible to increase ionic conductivity and utilization of active material in electrodes through the addition of macroscopic pores, a technique which could further enhance performance in FDI. However, macro-pores which extend through the entire length of the electrode provide a path for fluid with orders of magnitude higher permeability compared to the electrode microstructure. Such a macro-pore would cause the majority of influent to bypass the electrodes, and the system to no longer be "flow-through", limiting the salt ions supplied to the active particles. To direct the fluid through the electrode microstructure, an interdigitated pattern was designed for the electrodes, similar to those etched into graphite current collectors in redox flow batteries (RFBs) [138,139]. This interdigitated pattern, unlike spiral, serpentine, or parallel patterns used in RFBs, ensures that the path of the fluid goes through the electrode microstructure, rather than entirely through a macro-pore. Experiments with different patterns in RFBs aim to evenly distribute electrolyte to the electrode while reducing pumping power [140], developments which electrochemical desalination systems could learn from due to the significant pumping power needed to move large volumes of water [141]. The use of 3D-printing complex redox flow battery electrodes also has applications in battery heat management [142] and combining additive manufacturing methods to reduce pressure drops has motivated the simulation of more complex, 3-dimensionally tapering channels [143].

The FDI energy analysis from the Chapter 5 shows that even though electronic conductivity of the calendered PBA electrodes may reduce electrical energy consumption, the pumping power

is not reduced by increasing electronic conductivity and cannot be neglected. Other studies of electrochemical desalination have explicitly not taken pumping into account[144] or use flow-by electrodes where pumping power is small enough to be considered negligible[20,21], preferring to focus on electrical energy. In the context of electrochemical desalination, pumping is more often considered when studying flow electrode technology [145,146] where a viscous flow electrode is being pumped, without consideration of pumping water. Use of a recirculating FDI cell with dense flow-through electrodes has demonstrated exceptionally low electrical energy consumption, however pumping power remains a significant drawback, consuming an order of magnitude more energy than the applied current. From Darcy's law, the flow rate and pumping power depend on the hydraulic permeability of the electrodes, and this permeability depends on the average pore size. In the recirculating cell studied in Chapter 6, the densely calendered electrodes are less permeable than uncalendered electrodes, the flow rate was increased by a factor of four from the single-pass system in Chapter 4, and recirculating water means that only the reservoir volume is desalinated, not the total volume flowed through the electrodes. Inclusion of macroscopic pores, laser-milled to produce an interdigitated pattern in the PBA electrode surface, results in both higher ionic conductivity and higher hydraulic permeability, improving utilization and diminishing pumping power by multiple orders of magnitude.

Unlike patterns tested in RFBs, the proposed interdigitated patterns are milled into the electrode microstructure, rather than being milled into the current collector. While early macropore-patterned electrodes in Chapter 2 were fabricated using a 100 μm diameter end mill, the proposed pattern's increased complexity and the greater electrode size motivated the use of laser cutting to create the pores. Laser cutting has previously been used to increase utilization of active material in lithium-ion batteries [147] and increase hydraulic permeability in CDI by several

orders of magnitude [108], and is here applied for both purposes. In this chapter, results from a scaled-up FDI cell stemming from the design in Chapter 6 will be discussed, this time with both interdigitated macropores and a new desalination cell containing an eight-fold larger electrode area. With the newly constructed cell, the majority of salt could be extracted from larger volumes of water with salinity comparable to seawater, with the peak thermodynamic energy efficiency remaining over 40% when pumping losses are included.

7-2 Selection of pattern dimensions

One of the goals in adding interdigitated macro-pores was to reduce gradients in concentration and state-of-charge in the electrode, the same motivation which drove the development of the recirculating cell in Chapter 6. When designing the interdigitation pattern, there were three dimensions which could be varied: macro-pore channel width, channel spacing, and channel length. The last of these dimensions determines the gap between the end of the channel and the edge of the electrode. The objective of choosing the correct dimensions is to ensure even distribution of flow through the electrode microstructure while reducing the path length to less than 0.5 mm compared to the unpatterned electrode's 17 mm path length.

COMSOL Multiphysics was used to simulate water flowing within a single interdigitation, using symmetric boundary conditions to represent the model as one of numerous channel pairs and applying a uniform pressure at the inlet region. Within the macro-pore regions, the flow field $\vec{u}$ was found from the Navier-Stokes equation.

$$\rho \frac{\partial \vec{u}}{\partial t} + \rho(\vec{u} \cdot \nabla)\vec{u} = \nabla \cdot [-p + \mu(\nabla \vec{u} + (\nabla \vec{u})^T)] \qquad 7-1$$

The flow of water was assumed to be incompressible.

$$\rho \nabla \cdot \vec{u} = 0 \qquad 7-2$$

In the porous electrode region, the Darcy-Brinkman equation was used with porosity and permeability taken from experimental measurements.

$$\frac{\rho}{\varepsilon}\left(\frac{\partial \vec{u}}{\partial t} + (\vec{u}\cdot\nabla)\frac{\vec{u}}{\varepsilon}\right) = \nabla\cdot\left[-p + \mu(\nabla\vec{u} + (\nabla\vec{u})^T) - \frac{2\mu}{3\varepsilon}(\nabla\cdot\vec{u})\right] - \frac{\mu}{\kappa}\vec{u} \qquad 7-3$$

The goal of these simulations was to find combinations of dimensions which would produce as uniform a flow as possible through the electrode microstructure, without sacrificing a large amount of electrode material during patterning. To quantitatively evaluate the uniformity, residence time distribution $E(t)$ was found from adding a step function of 1 mM concentration at the inlet, and recording the outlet concentration over time.

$$E(t) = \frac{c(t)}{\int_0^\infty c(t)dt} \qquad 7-4$$

As the concentrated influent flows into the simulated electrode, concentration increases from 0 to 1 mM as fluid from the inlet reaches the outlet.

The channel width was less significant for keeping flow evenly distributed than it was for analyzing whether the increase in ionic conductivity and reduction in concentration gradients compensated for the loss of active material. For the channel spacing, as the path length needed to be <0.5 mm, the dimensions of 0.5 and 0.25 mm were selected. The channel length was the last dimension to determine, and particle tracking of fluid moving through the simulated flow paths indicated that flow was best kept uniform by making the distance from the channel's end to the electrode edge 1.5x the channel spacing. To illustrate the simulation outputs, Fig. 7-1 shows views of the simulation model, including pathlines of fluid flow for electrodes with varying dimensions.

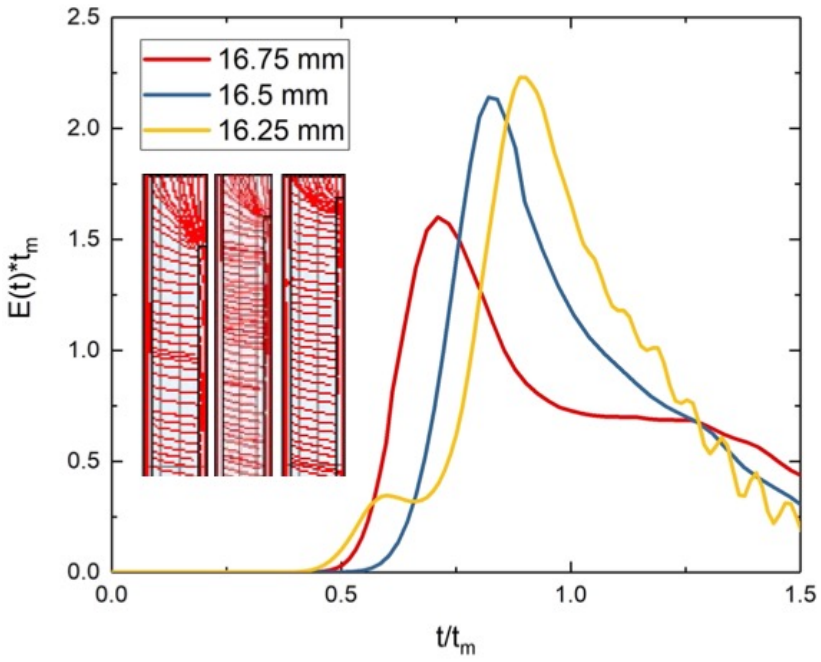

Figure 7-1: Residence time distribution functions for macro-pore channels of different lengths, illustrating how different lengths results in more uniform flow shown by the peak becoming narrower. The RTD and time are respectively normalized by multiplying and dividing by a "median time" t_m when the outlet concentration becomes half the inflowing concentration. Streamlines for electrode patterns with the three dimensions are inlaid, showing how longer channels provides a shorter path from the channel to the electrode's edge.

7-3 Laser-patterning of electrodes

The first set of laser-cut electrodes was provided by collaborators at Southern Methodist University, cut into four pairs of 15x17 mm electrodes for testing in the desalination cell. To confirm the quality of the patterns prior to testing, the patterns were examined using an SEM, images of which are shown in Fig. 7-2. The dimensions of the channels and their spacing are approximately the targeted dimensions, though there appears to be a heat-affected zone bordering the channel which became visibly rougher during the patterning process.

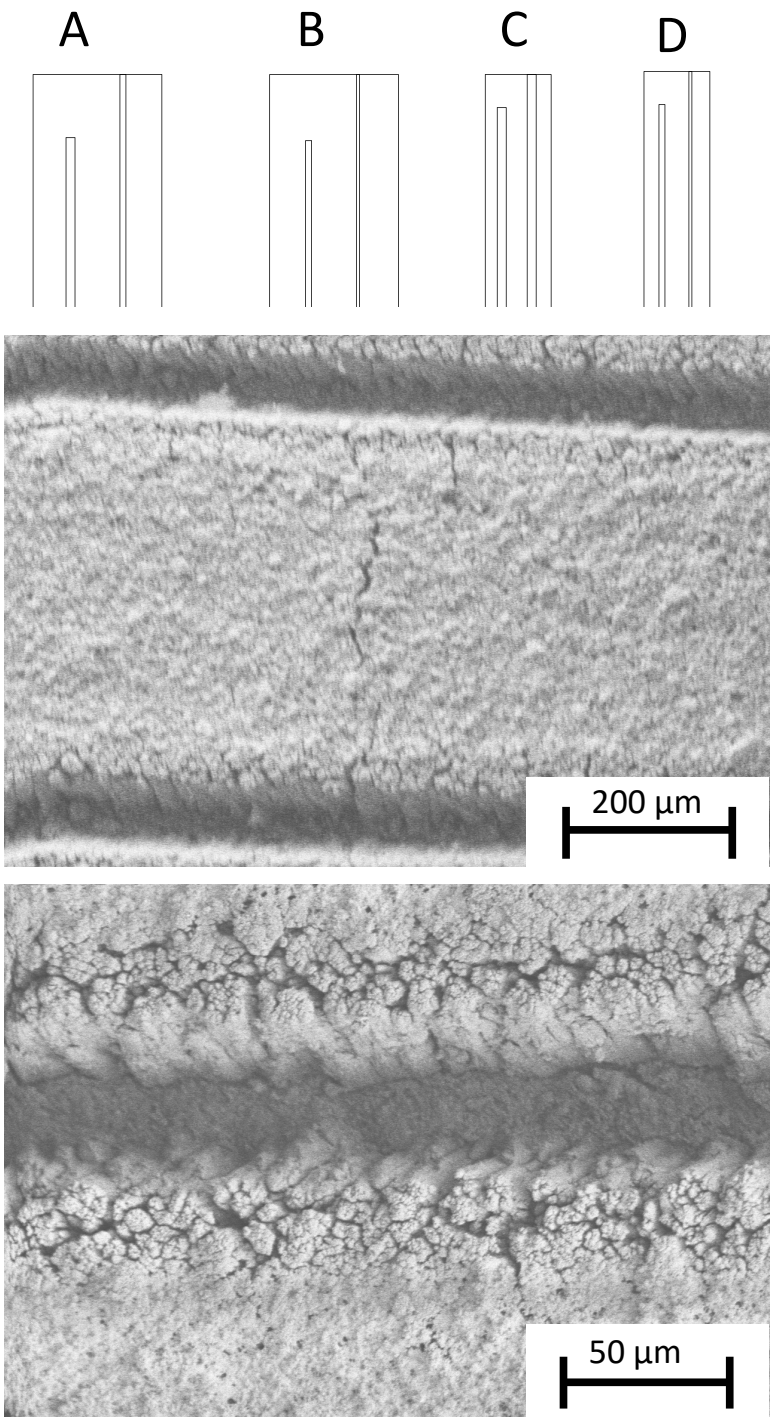

Figure 7-2: The top diagrams show renditions of the four patterns used, consisting of two macro-pore spacings with two macro-pore widths, and pore lengths dependent on their spacing. Below are SEM images of Pattern B, confirming the final dimensions and spacing of the macro-pores are what was desired.

Pattern	Channel width, w_c (μm)	Channel spacing, g (μm)	Channel length, l_c (mm)
A	100	500	16.25
B	50	500	16.25
C	100	250	16.625
D	50	250	16.625

Table 7-1: Key dimensions for the four patterns, assuming an electrode length of 17 mm.

For comparison with electrode performance in the single-pass system, the four patterns were tested under the same conditions described in Chapter 4. The flow rate was a constant 0.25 mL/min, influent concentration was 100 mM of aqueous NaCl, and current density varied between 1 to 8 mA/cm^2. Results for the electrodes' specific capacity is shown in Fig. 7-3, where all four patterns show a higher utilization than unpatterned electrodes at 1 mA/cm^2. Pattern A, though not showing capacity as high as other patterns at low current density, did show the lowest loss in utilization as current increased from 1 to 8 mA/cm^2. Of the other patterns, Pattern B showed no improvement over the unpatterned electrodes at high current density, Patterns C and D showed similar values while C sacrificed roughly 25% of its electrode material, leaving Pattern A the choice for further study.

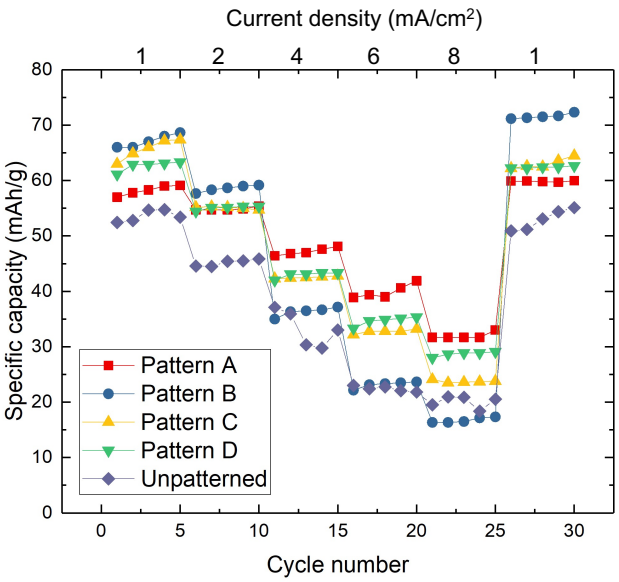

Figure 7-3: Specific capacity versus cycle number for the four patterns and unpatterned electrodes at varying current densities.

7-4 Testing of small-scale patterned electrodes

After determining that Pattern A would yield the best utilization, an electrode with that pattern was used in the scaled-up recirculating cell. This new electrode was calendered, containing approximately 11.1 mg/cm^2 of PBA at casting, and was then patterned with 100 µm wide channels spaced 500 µm apart. The experiment was conducted in the recirculating system, also using 100 mM influent, a flow rate of 1 mL/min, and a current density of 1 mA/cm^2 for comparison with the results in Chapter 6.

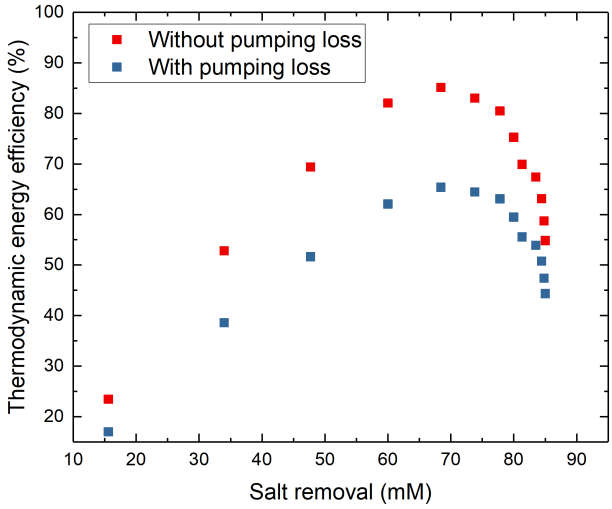

Figure 7-4: TEE versus salt removal for the desalination cell, including a comparison of efficiency with and without taking pumping losses into account.

With the addition of patterning, the FDI cell was able to achieve a TEE of 84% when reducing concentration of 100 mM influent by 70 mM, slightly more efficient than the unpatterned electrodes while achieving less salt removal. The loss of salt removal is attributable to the decrease in total electrode capacity, as 16% of the electrode mass was removed, and salt removal in the recirculating cell depends on how much salt can be removed before switching events. With the addition of pumping power, the peak TEE is reduced to 63%. This performance remains high, however it demonstrates the significance of pumping power losses. With the patterned electrodes' viability proven, the next step was to construct a scaled-up cell to desalinate larger volumes of water to greater degrees.

7-5 Scaling-up of the FDI cell

For the densest electrodes, over half the cell's internal volume was contained in the tubing supplying and removing the saltwater. If the electrode area increased, the tubing volume would

become less significant and the mixing volume per unit electrode capacity would be expected to decrease. This motivated increasing the total capacity of the cell, expecting there would be a greater increase in capacity than mixing volume. When developing a larger desalination cell, the majority of the design aspects remained the same as the cell described in Chapters 4 and 6, the only difference being an increase in electrode area from 2.5 cm^2 to 20.25 cm^2. With the greater electrode area, applying the same current density would remove salt from the flow eight times as rapidly, demanding the flow rate increase to provide sufficient salt.

During pause period calibration tests to minimize mixing volume, it was found that there was a trade-off between the flow rate and the maximum salt removal achieved. If the flow rate is too high, the mixing effect becomes more significant due to greater dispersion, resulting in a lack of a clear minimum mixing volume found for the experiment of Chapter 6. However, if the flow rate is too low, the electrode is not being provided enough sodium ions and the capacity is not being fully utilized, decreasing the salt removed in a single cycle. The best results were achieved using a flow rate of 5 mL/min, and potable water was produced despite the increasing impedance of the desalinated water.

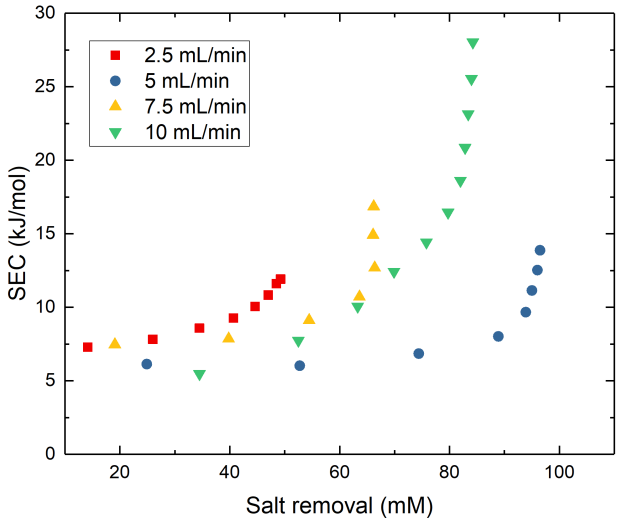

Figure 7-5: SEC versus salt removal for different flow rates.

After completing the study of flow rates, a new electrode was fabricated with an active material loading of 15.5 mg/cm^2, the highest areal loading tested yet, calendered from 400 μm to a thickness of 180 μm. The final thickness was 180 μm rather than 150 μm due to any further compression potentially destroying the electrode, and the added thickness was accounted for in the cell's assembly with a slightly thicker set of gaskets. This electrode was laser-patterned as the first pair was, and subsequently used in a study of increasing current density with 500 mM salt water. As in the previous experiments, the first current density used was 1 mA/cm^2 applied to the 20.25 cm^2 electrode. At a flow rate of 5 mL/min, the recirculating desalination cell was able to decrease salt concentration of a 500 mM, 25 mL reservoir by 340 mM. As increasing current density was expected to increase salt removal rate and energy consumption while decreasing utilization, it was known that greater desalination would not be achieved, however the increased removal rate of salt could make the tradeoff worth the disadvantages.

7-6 Energy consumption and salt removal with increased current density

To study the effect of increased salt removal and its relationship with SEC in the recirculating cell, current density was increased from 1 to 2, 3, and 4 mA/cm^2. The SEC of the cell showed a trend roughly proportional to the current density, as expected from the results in Chapter 4. Though the salt was removed more rapidly from the system, the increased polarization during charging and discharging decreased the active material utilization. With the electrodes removing less salt with each half-cycle, the effect of mixing became more prominent as current density increased, causing maximum salt removal to lower from 340 mM for 1 mA/cm^2 to 247 mM for 4 mA/cm^2.

It can be approximated from Darcy's law that when using the hydraulic permeability measured in Chapter 3 for 85% porous PBA electrode (1.28 μm^2), channels as small as 50 μm wide showed orders of magnitude lower resistance to fluid flow, making pressure drops negligible along the channel length. This effective permeability $k_{h,eff}$ of the patterned electrodes is expected to increase by up to three orders of magnitude compared with the unpatterned electrode permeability k_h, depending on the dimensions of the pattern listed in Table 7-1 and electrode length l_e.

$$k_{h,eff} = k_h \frac{l_e}{g} \frac{2l_c}{2g + w_c} \qquad (7-5)$$

Due to the patterns directing flow over a shorter path length and through a larger cross-sectional area, the effective permeability becomes higher, theoretically being over three orders of magnitude higher in the case of Pattern A. Tests flowing water through the system to calculate permeability showed the permeability to increase by a factor of 790, not as high as predicted but reducing the pumping power to a manageable level.

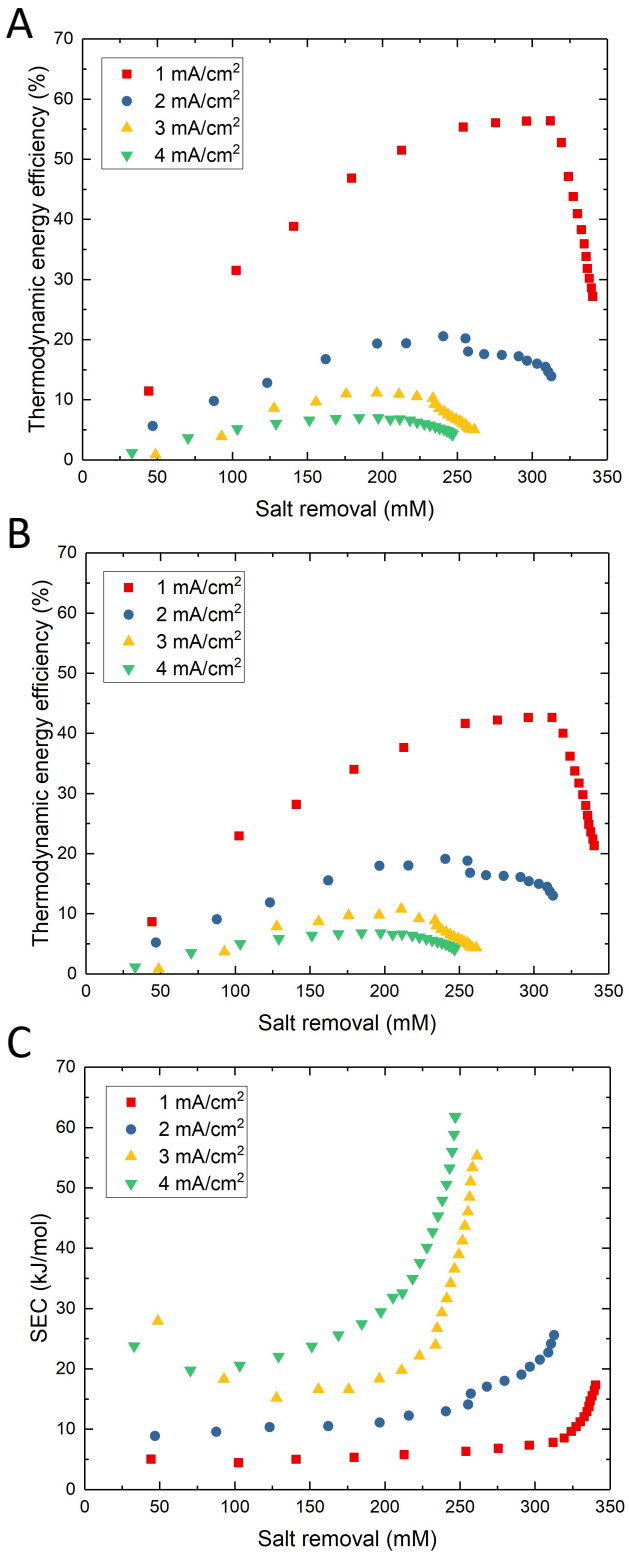

Figure 7-6: TEE versus salt removal for the scaled-up cell (A) without taking pumping energy into account and (B) with the pumping losses. Subfigure (C) shows SEC, including pumping power, versus salt removal.

The recirculating cell, when using calendered electrodes with macroscopic patterns, removed up to 68% of the salt from 500 mM influent, moving the use of FDI with seawater closer to practicality. The increased hydraulic permeability also reduces pumping losses by multiple orders of magnitude, and the contribution of pumping energy became less significant as current density increased. With the same electrode pair used and the flow rate kept constant, pumping power was constant during all four experiments, while electrical power increased with current density. Increasing current density lowered charging times, reducing the pumping energy further. Compared with the results in Chapter 6, the enlarged cell shows the feasibility of the cell's increased scale, achieving higher salt removal from higher salinity influent.

Despite the increase in ionic conductivity due to both the patterning and the high salt concentration, TEE was limited to less than 56%, believed to be due to high concentration gradients. Though ionic conductivity is high with 500 mM influent, the concentration gradient between anode and cathode become greater with the increased desalination performance.

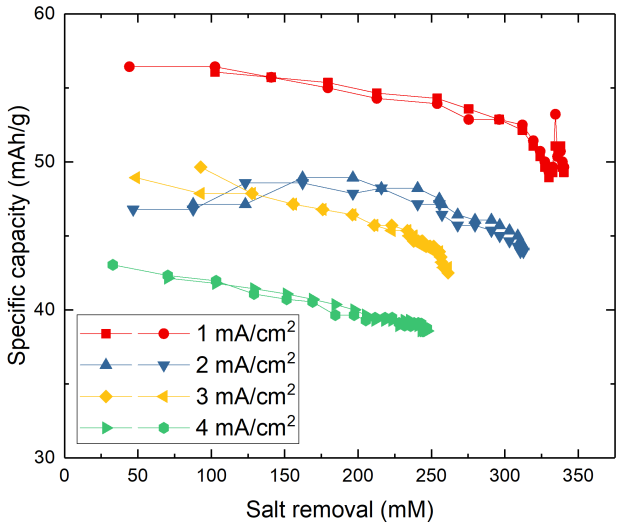

Figure 7-7: Specific capacity of the scaled-up cell at different current densities.

Applying higher current densities led to decreased utilization of the PBA, reducing the salt that could be removed over a single half-cycle. With the changing salt concentration in the two sides of the cell, the cell impedance gradually increases, as it did during the experiments with 100 mM influent in Chapter 6. Due to the abundance of ions in the 500 mM influent, the effect is less pronounced, and utilization only decreases by ~10% at most compared with >50% capacity reductions when using 100 mM influent. The loss in utilization can also be explained by increasing polarization from higher current density, as sodium ions in the solid particles can't diffuse quickly enough for the total capacity to be utilized.

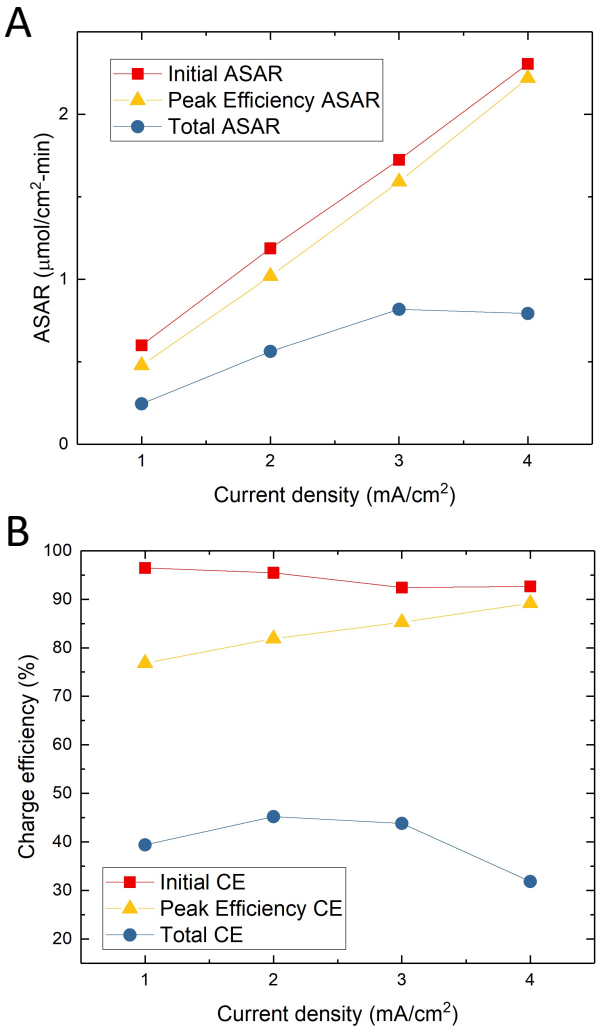

Figure 7-8: A) ASARs and B) charge efficiencies versus current density of the cell.

Average salt absorption rate (ASAR) is comparable to that in the small cell, as expected from using the same current density in the first test. Charge efficiency (CE) was also calculated to compare how efficiently the applied current was used to remove salt from influent. Three different CEs were calculated: the initial CE, or the efficiency during the first half cycle before switching occurs, the CE at peak TEE, and the total CE over the full duration of the experiment. Initial CE remains over 90% with increasing current, though there is a decline from 97% to 92% visible in Fig. 7-8A. The CE at peak TEE shows a gradual increase with current density, which can be explained by the curves in Fig. 7-6A, which show the experiment reaching peak TEE after fewer cycles. Because there are fewer switching events, less mixing occurs, and the CE is higher. Total ASAR and CE are by far the lowest due to the numerous switching events during the experiment mixing brine and dilute, reducing the total salt removed.

7-7 Conclusions

It was demonstrated that the addition of interdigitated macro-pores increased utilization in PBA electrodes, with a degree of improvement dependent on macro-pore dimensions. Use of these macro-pores also caused an increase in hydraulic permeability, which had previously made the system's total energy consumption impractically high. Flow rate through the system also determines performance due to trade-offs between mixing and capacity. If flow rate is too low, the electrodes are not supplied Na^+ ions to intercalate and their capacity is not fully utilized, however higher flow rates increase dispersion and mixing between brine and effluent.

The use of patterned electrodes increased energy efficiency in the FDI cell, leading to the development of an enlarged cell which removed 340 mM of salt from 500 mM influent. TEE was

lower compared with the small-scale cell, which is attributable to the higher concentration polarization that came with the greater difference in concentration between the two sides of the cell. Increasing current density increased polarization, decreasing TEE, utilization, and salt removal. An increase from 1 to 4 mA/cm^2 reduced the peak TEE from 56% to 8%, and maximum salt removal from 340 to 247 mM. ASAR increased in proportion to current density, reaching peak TEE while maintaining a high charge efficiency.

CHAPTER 8: CONCLUSIONS AND FUTURE WORK

8-1 Final remarks

This work comprises a wide range of experiments and developments in electrochemical desalination aiming to solve the challenges preventing practical application on a large scale. Limitations in active material utilization, ohmic energy losses from high electrode resistance, supply of sodium ions to active material, pumping energy, and the inability to fully desalinate saltwater over a single pass have all been addressed through combinations of modifications to the system at many length scales.

Experimentation with different conductive additives at differing mass fractions revealed how the additives' effects can vary depending on particle size, resulting in electronic conductivity varying by multiple orders of magnitude between electrodes containing the same mass fraction of carbon black. Recognizing the role size plays in the formulation of electrodes led to the application of colloidal physics to further increase electronic conductivity, attempting to encourage carbon particle aggregation into a conductive network. These efforts succeeded in not only producing more electronically conductive electrodes, but thicker, mechanically stable electrodes as well. These thick, high-areal loading electrodes were calendered to further increase their electronic conductivity, and subsequent desalination experiments yielded the highest TEE yet obtained.

Increasing ionic conductivity was an early effort to improve active material utilization, and machining of linear macroscopic pores into a capacitive electrode's surface was demonstrated to reduce impedance and improve capacity, and was shown to improve performance in CDI experiments[69]. Applying this method in an FDI cell required a more complex interdigitated pattern to evenly distribute influent saltwater through the electrode, leading to the laser-patterning

of PBA electrodes for use in the desalination cell. This interdigitated pattern had the dual benefit of increasing ionic conductivity and hydraulic permeability, as the patterning caused the fluid to move across wide cross-sectional area over a shorter path in the electrode, reducing otherwise exorbitant pumping power losses by over two orders of magnitude.

To achieve high salt removal, the first FDI cell was tested at increasing current densities to extract salt from inflowing water more quickly, however the increasing energy demands and declining utilization with fast charging rates made single-pass desalination unviable. An automated recirculating fluid circuit was designs to flow water to and from two reservoirs, alternating between charging and discharging cycles such that one reservoir would be continuously concentrated while the other would be desalinated. This removed the need for single-pass desalination, and optimization of the system by removing internal volume and calibrating switching periods led to superior desalination performance compared to the single-pass system. Ultimately, the first FDI cell was limited by its small size, requiring the construction of a new cell with larger electrodes to remove larger amounts of salt during a single cycle.

Upon completion of the scaled-up cell, new electrodes combining the previously studied colloidal fabrication, calendering, and laser-patterning were made with an eightfold larger surface area and tested in the recirculating system. From 100 mM influent, 96% of the salt could be removed from one reservoir, and 68% of the salt could be removed from 500 mM influent, showing that FDI can remove the majority of salt from seawater. The system remains limited by desalinate and brine mixing between cycles, however the system achieved excellent thermodynamic energy efficiencies of up to 46% while removing 300 mM of saltwater.

The work in this thesis represents a significant step forward in the development of practical, energy-efficient cation-intercalation desalination technology. Thermodynamic energy efficiency

was found to be superior to any previous electrochemical desalination system, achieved due to a combination of novel cell design and advanced fabrication techniques targeting reduction of energy losses while improving electrode capacity. The work in this dissertation demonstrates multiple leaps forward in understanding energy losses in FDI systems and how to overcome them.

8-2 Recommendation for future work

Based on the research presented in this thesis, future work in the field of electrochemical desalination may pursue several different directions. The application of colloidal physics to electrode fabrication processes could further increases electronic conductivity and active particle loading, improving electrode capacity while decreasing energy losses due to internal resistance. Colloidal fabrication experiments with both PBA and inert pseudo-active particles significantly varied in electronic conductivity, and the same techniques could be applied to other battery materials. Work has been done using colloidal forces to model rheological properties in Li-ion electrode slurries [124] but using those forces to target electrode properties has not been thoroughly studied elsewhere.

Considering the improvements demonstrated by the interdigitated flow field, experimenting with more complex flow fields or changing the macro-pore dimensions could optimize the ratio between electrical and pumping power. Cell design is another area of improvement, especially the use of influent moving through electrodes in a multi-cell stack. Similar designs have been proposed in electrodialysis[60], removing water from multiple streams running in parallel. The FDI cell could be modified to do the same with the addition of multiple electrode pairs.

With the most significant energy losses reduced, the next step in making FDI practical and cost effective on a larger scale would be the increase of removal rate and electrode longevity without increasing energy consumption. Modifications to the PBA nanoparticles could improve utilization of electrode materials at high charging rates, such as the use of yolk-shell nanostructures[148] or more highly crystalline particles[149] improving solid-state Na-ion diffusion. Utilizing sodium super-ionic conductor (NASICON) particles[150,151], which have a higher volumetric capacity for sodium ions than PBA, is another option for increasing the capacity of electrodes. The selection of new conductive additives in place of Ketjen black could also further enhance electronic conductivity and reduce ohmic losses during charging.

Ongoing work should continue to increase the scale, removal rate, and efficiency of the electrodes to eventually create FDI cells able to meet the growing demand for potable water. Continuing to develop and combine existing technologies and methods with new developments could make FDI commercially viable in the near future.

REFERENCES

[1] M.M. Mekonnen, A.Y. Hoekstra, Four billion people facing severe water scarcity, Sci. Adv. 2 (2016) e1500323. doi:10.1126/sciadv.1500323.

[2] M. Elimelech, W.A. Phillip, The future of seawater desalination: energy, technology, and the environment, Science (80-.). 333 (2011) 712–717. doi:10.1126/science.1200488.

[3] E. Jones, M. Qadir, M.T.H. van Vliet, V. Smakhtin, S. mu Kang, The state of desalination and brine production: A global outlook, Sci. Total Environ. 657 (2019) 1343–1356. doi:10.1016/j.scitotenv.2018.12.076.

[4] A. Subramani, J.G. Jacangelo, Treatment technologies for reverse osmosis concentrate volume minimization: A review, Sep. Purif. Technol. 122 (2014) 472–489. doi:10.1016/j.seppur.2013.12.004.

[5] M.S. Mauter, P.S. Fiske, Desalination for a circular water economy, Energy Environ. Sci. 13 (2020) 3180–3184. doi:10.1039/d0ee01653e.

[6] M.E. Suss, S. Porada, X. Sun, P.M. Biesheuvel, J. Yoon, V. Presser, Water desalination via capacitive deionization: what is it and what can we expect from it?, Energy Environ. Sci. 8 (2015) 2296–2319. doi:10.1039/C5EE00519A.

[7] W. Tang, J. Liang, D. He, J. Gong, L. Tang, Z. Liu, Various cell architectures of capacitive deionization : Recent advances and future trends, Water Res. 150 (2019) 225–251. doi:10.1016/j.watres.2018.11.064.

[8] M. Metzger, M.M. Besli, S. Kuppan, S. Hellstrom, S. Kim, E. Sebti, C. V. Subban, J. Christensen, Techno-economic analysis of capacitive and intercalative water deionization, Energy Environ. Sci. 13 (2020) 1544–1560. doi:10.1039/d0ee00725k.

[9] K.C. Smith, R.D. Dmello, Na-Ion Desalination (NID) Enabled by Na-Blocking Membranes and Symmetric Na-Intercalation: Porous-Electrode Modeling, J. Electrochem. Soc. 163 (2016) A530–A539. doi:10.1149/2.0761603jes.

[10] K.C. Smith, Theoretical evaluation of electrochemical cell architectures using cation intercalation electrodes for desalination, Electrochim. Acta. 230 (2017) 333–341. doi:10.1016/j.electacta.2017.02.006.

[11] S. Liu, K.C. Smith, Quantifying the Trade-offs between Energy Consumption and Salt Removal Rate in Membrane-free Cation Intercalation Desalination, Electrochim. Acta. 271 (2018) 652–665. doi:10.1016/j.electacta.2018.03.065.

[12] S. Porada, A. Shrivastava, P. Bukowska, P.M. Biesheuvel, K.C. Smith, Nickel Hexacyanoferrate Electrodes for Continuous Cation Intercalation Desalination of Brackish Water, Electrochim. Acta. 255 (2017) 369–378. doi:10.1016/j.electacta.2017.09.137.

[13] T. Kim, C.A. Gorski, B.E. Logan, Low Energy Desalination Using Battery Electrode Deionization, Environ. Sci. Technol. Lett. 4 (2017) 444–449. doi:10.1021/acs.estlett.7b00392.

[14] S. Malifarge, B. Delobel, C. Delacourt, Determination of Tortuosity Using Impedance Spectra Analysis of Symmetric Cell, J. Electrochem. Soc. 164 (2017) 3329–3334. doi:10.1149/2.0331711jes.

[15] J. Landesfeind, J. Hattendorff, A. Ehrl, W.A. Wall, H.A. Gasteiger, Tortuosity Determination of Battery Electrodes and Separators by Impedance Spectroscopy, J. Electrochem. Soc. 163 (2016) A1373–A1387. doi:10.1149/2.1141607jes.

[16] V.P. Nemani, S.J. Harris, K.C. Smith, Design of Bi-Tortuous, Anisotropic Graphite Anodes for Fast Ion-Transport in Li-Ion Batteries, J. Electrochem. Soc. 162 (2015)

A1415–A1423. doi:10.1149/2.0151508jes.

[17] M. Zhu, J. Park, A.M. Sastry, Particle Interaction and Aggregation in Cathode Material of Li-Ion Batteries: A Numerical Study, J. Electrochem. Soc. 158 (2011) A1155. doi:10.1149/1.3625286.

[18] M. Zhu, J. Park, A.M. Sastry, W. Lu, Numerical Study of Interaction and Aggregation of Non-Spherical Particles in Forming Li-Ion Battery Cathodes, J. Electrochem. Soc. 161 (2014) A1247–A1252. doi:10.1149/2.0211409jes.

[19] A. van Bommel, R. Divigalpitiya, Effect of Calendering LiFePO4 Electrodes, J. Electrochem. Soc. 159 (2012) A1791–A1795. doi:10.1149/2.029211jes.

[20] R. Zhao, S. Porada, P.M. Biesheuvel, A. van der Wal, A. der Wal, A. van der Wal, A. der Wal, Energy consumption in membrane capacitive deionization for different water recoveries and flow rates, and comparison with reverse osmosis, Desalination. 330 (2013) 35–41. doi:10.1016/j.desal.2013.08.017.

[21] S.A. Hawks, A. Ramachandran, S. Porada, P.G. Campbell, M.E. Suss, P.M. Biesheuvel, J.G. Santiago, M. Stadermann, Performance metrics for the objective assessment of capacitive deionization systems, Water Res. 152 (2019) 126–137. doi:10.1016/j.watres.2018.10.074.

[22] A.C. Arulrajan, D.L. Ramasamy, M. Sillanpää, A. Van Der Wal, P.M. Biesheuvel, S. Porada, J.E. Dykstra, Exceptional Water Desalination Performance with Anion-Selective Electrodes, (2019) 1–5. doi:10.1002/adma.201806937.

[23] M. Son, V. Pothanamkandath, W. Yang, C.A. Gorski, B.E. Logan, Improving the Thermodynamic Energy Efficiency of Battery Electrode Deionization Using Flow-Through Electrodes, Environ. Sci. Technol. (2020). doi:10.1021/acs.est.9b06843.

[24] Y. Liu, X. Gao, Z. Wang, K. Wang, X. Dou, H. Zhu, X. Yuan, L. Pan, Controlled synthesis of bismuth oxychloride-carbon nanofiber hybrid materials as highly efficient electrodes for rocking-chair capacitive deionization, Chem. Eng. J. 403 (2021) 126326. doi:10.1016/j.cej.2020.126326.

[25] V. Pothanamkandathil, J. Fortunato, C.A. Gorski, Electrochemical Desalination Using Intercalating Electrode Materials: A Comparison of Energy Demands, Environ. Sci. Technol. 54 (2020) 3653–3662. doi:10.1021/acs.est.9b07311.

[26] J. Lee, S. Kim, J. Yoon, Rocking Chair Desalination Battery Based on Prussian Blue Electrodes, ACS Omega. 2 (2017) 1653–1659. doi:10.1021/acsomega.6b00526.

[27] J. Ahn, J. Lee, S. Kim, C. Kim, J. Lee, P.M. Biesheuvel, J. Yoon, High performance electrochemical saline water desalination using silver and silver-chloride electrodes, Desalination. 476 (2020) 114216. doi:10.1016/j.desal.2019.114216.

[28] P. Xu, T.Y. Cath, A.P. Robertson, M. Reinhard, J.O. Leckie, J.E. Drewes, Critical review of desalination concentrate management, treatment and beneficial use, Environ. Eng. Sci. 30 (2013) 502–514. doi:10.1089/ees.2012.0348.

[29] D.A. Roberts, E.L. Johnston, N.A. Knott, Impacts of desalination plant discharges on the marine environment: A critical review of published studies, Water Res. 44 (2010) 5117–5128. doi:10.1016/j.watres.2010.04.036.

[30] S. Porada, R. Zhao, A. Van Der Wal, V. Presser, P.M. Biesheuvel, Review on the science and technology of water desalination by capacitive deionization, Prog. Mater. Sci. 58 (2013) 1388–1442. doi:10.1016/j.pmatsci.2013.03.005.

[31] S. Porada, M. Bryjak, A. Van Der Wal, P.M. Biesheuvel, A. Van Der Wal, Effect of electrode thickness variation on operation of capacitive deionization, Electrochim. Acta.

75 (2012) 148–156. doi:10.1016/j.electacta.2012.04.083.

[32] S. Jeon, H. Park, J. Yeo, S. Yang, C.H. Cho, M.H. Han, D.K. Kim, Desalination via a new membrane capacitive deionization process utilizing flow-electrodes, Energy Environ. Sci. 6 (2013) 1471–1475. doi:10.1039/C3EE24443A.

[33] K.C. Smith, R. Dmello, Na-Ion Desalination (NID) Enabled by Na-Blocking Membranes and Symmetric Na-Intercalation: Porous-Electrode Modeling, J. Electrochem. Soc. 163 (2016) A530–A539. doi:10.1149/2.0761603jes.

[34] M. Pasta, C.D. Wessells, Y. Cui, F. La Mantia, A Desalination Battery, Nano Lett. 12 (2012) 839–843. doi:10.1021/nl203889e.

[35] J. Lee, S. Kim, C. Kim, J. Yoon, Hybrid capacitive deionization to enhance the desalination performance of capacitive techniques, Energy Environ. Sci. 7 (2014) 3683–3689. doi:10.1039/C4EE02378A.

[36] N. Epstein, On tortuosity and the tortuosity factor in flow and diffusion through porous media, Chem. Eng. Sci. 44 (1989) 777–779. doi:10.1016/0009-2509(89)85053-5.

[37] M. Ebner, D.W. Chung, R.E. García, V. Wood, Tortuosity anisotropy in lithium-ion battery electrodes, Adv. Energy Mater. 4 (2014) 1–6. doi:10.1002/aenm.201301278.

[38] J. van Brakel, P.M. Heertjes, Analysis of diffusion in macroporous media in terms of a porosity, a tortuosity and a constrictivity factor, Int. J. Heat Mass Transf. 17 (1974) 1093–1103. doi:10.1016/0017-9310(74)90190-2.

[39] I. V. Thorat, D.E. Stephenson, N.A. Zacharias, K. Zaghib, J.N. Harb, D.R. Wheeler, Quantifying tortuosity in porous Li-ion battery materials, J. Power Sources. 188 (2009) 592–600. doi:10.1016/j.jpowsour.2008.12.032.

[40] C.-J.J. Bae, C.K. Erdonmez, J.W. Halloran, Y.-M.M. Chiang, Design of battery electrodes

with dual-scale porosity to minimize tortuosity and maximize performance, Adv. Mater. 25 (2013) 1254–1258. doi:10.1002/adma.201204055.

[41] D.-W. Chung, M. Ebner, D.R. Ely, V. Wood, R. Edwin García, Validity of the Bruggeman relation for porous electrodes, Model. Simul. Mater. Sci. Eng. 21 (2013) 074009. doi:10.1088/0965-0393/21/7/074009.

[42] C.L. Cobb, M. Blanco, Modeling mass and density distribution effects on the performance of co-extruded electrodes for high energy density lithium-ion batteries, J. Power Sources. 249 (2014) 357–366. doi:10.1016/j.jpowsour.2013.10.084.

[43] C.L. Cobb, S.E. Solberg, Communication—Analysis of Thick Co-Extruded Cathodes for Higher-Energy-and-Power Lithium-Ion Batteries, J. Electrochem. Soc. 164 (2017) A1339–A1341. doi:10.1149/2.0101707jes.

[44] Y. Li, K.K. Fu, C. Chen, W. Luo, T. Gao, S. Xu, J. Dai, G. Pastel, Y. Wang, B. Liu, J. Song, Y. Chen, C. Yang, L. Hu, Enabling High-Areal-Capacity Lithium-Sulfur Batteries: Designing Anisotropic and Low-Tortuosity Porous Architectures, ACS Nano. 11 (2017) 4801–4807. doi:10.1021/acsnano.7b01172.

[45] J. Billaud, F. Bouville, T. Magrini, C. Villevieille, A.R. Studart, Magnetically aligned graphite electrodes for high-rate performance Li-ion batteries, Nat. Energy. 1 (2016) 1–6. doi:10.1038/nenergy.2016.97.

[46] X. He, J.E. Yoo, M.H. Lee, J. Bae, Morphology engineering of ZnO nanostructures for high performance supercapacitors : enhanced electrochemistry of ZnO nanocones compared to ZnO nanowires, Nanotechnology. 28 (2017).

[47] E.R. Reale, K.C. Smith, Capacitive Performance and Tortuosity of Activated Carbon Electrodes with Macroscopic Pores, J. Electrochem. Soc. 165 (2018) A1685–A1693.

doi:10.1149/2.0601809jes.

[48] J.-A. Lim, N.-S. Park, J.-S. Park, J.-H. Choi, L. Jung-Ae, P. Nam-Soo, P. Jin-Soo, C. Jae-Hwan, Fabrication and characterization of a porous carbon electrode for desalination of brackish water, Desalination. 238 (2009) 37–42. doi:http://dx.doi.org/10.1016/j.desal.2008.01.033.

[49] V.S. Battaglia, Optimization of Acetylene Black Conductive Additive and PVDF Composition for High-Power Rechargeable Lithium-Ion, (2007) 1129–1134. doi:10.1149/1.2792293.

[50] A. Kolodziej, K. Fic, E. Frackowiak, Towards sustainable power sources: chitin-bound carbon electrodes for electrochemical capacitors, J. Mater. Chem. A. 3 (2015) 22923–22930. doi:10.1039/C5TA06750B.

[51] H. Zarrabi, M.E. Yekavalangi, V. Vatanpour, A. Shockravi, M. Safarpour, Improvement in desalination performance of thin film nanocomposite nanofiltration membrane using amine-functionalized multiwalled carbon nanotube, Desalination. 394 (2016) 83–90. doi:10.1016/j.desal.2016.05.002.

[52] K. Laxman, M.T.Z. Myint, M. Al Abri, P. Sathe, S. Dobretsov, J. Dutta, Desalination and disinfection of inland brackish ground water in a capacitive deionization cell using nanoporous activated carbon cloth electrodes, Desalination. 362 (2015) 126–132. doi:10.1016/j.desal.2015.02.010.

[53] J.H. Chen, W.Z. Li, D.Z. Wang, S.X. Yang, J.G. Wen, Z.F. Ren, Electrochemical characterization of carbon nanotubes as electrode in electrochemical double-layer capacitors, 40 (2002) 1193–1197.

[54] M.T.Z. Myint, S.H. Al-Harthi, J. Dutta, Brackish water desalination by capacitive

deionization using zinc oxide micro/nanostructures grafted on activated carbon cloth electrodes, Desalination. 344 (2014) 236–242. doi:10.1016/j.desal.2014.03.037.

[55] A.M. Johnson, J. Newman, Desalting by Means of Porous Carbon Electrodes, J. Electrochem. Soc. 118 (1971) 510–517. doi:10.1149/1.2408094.

[56] M.E. Suss, T.F. Baumann, W.L. Bourcier, C.M. Spadaccini, K.A. Rose, J.G. Santiago, M. Stadermann, Capacitive desalination with flow-through electrodes, Energy Environ. Sci. 5 (2012) 9511. doi:10.1039/c2ee21498a.

[57] W. Lai, F. Ciucci, Mathematical modeling of porous battery electrodes-Revisit of Newman's model, Electrochim. Acta. 56 (2011) 4369–4377. doi:10.1016/j.electacta.2011.01.012.

[58] J.S. Newman, K.E. Thomas-Alyea, Electrochemical Systems, 3rd Ed., Wiley, 2004.

[59] M. Della Monica, G. Petrella, A. Sacco, S. Bufo, Transference numbers in concentrated sodium chloride solutions, Electrochim. Acta. 24 (1979) 1013–1017. doi:10.1016/0013-4686(79)87099-1.

[60] K.C. Smith, Theoretical evaluation of electrochemical cell architectures using cation intercalation electrodes for desalination, Electrochim. Acta. 230 (2017) 333–341. doi:10.1016/j.electacta.2017.02.006.

[61] X. Shang, R.D. Cusick, K.C. Smith, A Combined Modeling and Experimental Study Assessing the Impact of Fluid Pulsation on Charge and Energy Efficiency in Capacitive Deionization, J. Electrochem. Soc. 164 (2017) E536–E547. doi:10.1149/2.0841714jes.

[62] A. Hemmatifar, M. Stadermann, J.G. Santiago, Two-Dimensional Porous Electrode Model for Capacitive Deionization, J. Phys. Chem. C. 119 (2015) 24681–24694. doi:10.1021/acs.jpcc.5b05847.

[63] J.F. Chambers, J.M. Stokes, R.H. Stokes, Conductance of Concentrated Aqueous Sodium and Potassium Chloride Solutions at 25, 60 (1956) 985–986. doi:10.1021/j150541a040.

[64] C. Kim, J. Lee, P. Srimuk, M. Aslan, V. Presser, Concentration-Gradient Multichannel Flow-Stream Membrane Capacitive Deionization Cell for High Desalination Capacity of Carbon Electrodes, ChemSusChem. (2017) 4914–4920. doi:10.1002/cssc.201700967.

[65] M.E. Orazem, I. Frateur, B. Tribollet, V. Vivier, S. Marcelin, N. Pebere, A.L. Bunge, E.A. White, D.P. Riemer, M. Musiani, Dielectric Properties of Materials Showing Constant-Phase-Element (CPE) Impedance Response, J. Electrochem. Soc. 160 (2013) C215–C225. doi:10.1149/2.033306jes.

[66] J. Bisquert, G. Garcia-Belmonte, P. Bueno, E. Longo, L.O.. Bulhões, Impedance of constant phase element (CPE)-blocked diffusion in film electrodes, J. Electroanal. Chem. 452 (1998) 229–234. doi:10.1016/S0022-0728(98)00115-6.

[67] M. Egashira, N. Sawada, K. Ueda, N. Yoshimoto, M. Morita, Capacitance of porous carbon electrode in mixed salt non-aqueous electrolytes, J. Power Sources. 195 (2010) 1761–1764. doi:10.1016/j.jpowsour.2009.09.041.

[68] B.T. Habte, F. Jiang, Effect of microstructure morphology on Li-ion battery graphite anode performance: Electrochemical impedance spectroscopy modeling and analysis, Solid State Ionics. 314 (2018) 81–91. doi:10.1016/j.ssi.2017.11.024.

[69] A.P. Bhat, E.R. Reale, K.C. Smith, R.D. Cusick, Reducing impedance to ionic flux in capacitive deionization with Bi-tortuous activated carbon electrodes coated with asymmetrically charged polyelectrolytes, Water Res. X. 3 (2019) 100027. doi:10.1016/j.wroa.2019.100027.

[70] L. Wang, S. Lin, Intrinsic Tradeoff Between Kinetic and Energetic Efficiencies in

Membrane Capacitive Deionization, Water Res. 129 (2018) 394–401. doi:10.1016/j.watres.2017.11.027.

[71] S.A. Hawks, J.M. Knipe, P.G. Campbell, C.K. Loeb, M.A. Hubert, J.G. Santiago, M. Stadermann, Quantifying the flow efficiency in constant-current capacitive deionization, Water Res. 129 (2018) 327–336. doi:10.1016/j.watres.2017.11.025.

[72] T. Kim, J. Yoon, CDI ragone plot as a functional tool to evaluate desalination performance in capacitive deionization, RSC Adv. 5 (2014) 1456–1461. doi:10.1039/C4RA11257A.

[73] M.F. Ashby, Materials Selection in Mechanical Design, 4th ed., 2011.

[74] R. Dmello, J.D. Milshtein, F.R. Brushett, K.C. Smith, Cost-Driven Materials Selection Criteria for Redox Flow Battery Electrolytes, J. Power Sources. 330 (2016) 261–272. doi:10.1016/j.jpowsour.2016.08.129.

[75] T. Wei, F.Y. Fan, A. Helal, A. Shrivastava, G.H. Mckinley, Y. Chiang, J.A. Lewis, Biphasic Electrode Suspensions for Li-Ion Semi-solid Flow Cells with High Energy Density , Fast Charge Transport , and Low-Dissipation Flow, Adv. Energy Mater. (2015) 1–7. doi:10.1002/aenm.201500535.

[76] M.E. Suss, Water Desalination with Energy Storage Electrode Materials, Joule. 2 (2018) 10–15. doi:10.1016/j.joule.2017.12.010.

[77] A. Shrivastava, K.C. Smith, Electron Conduction in Nanoparticle Agglomerates Limits Apparent Na+ Diffusion in Prussian Blue Analogue Porous Electrodes, J. Electrochem. Soc. 165 (2018) A1777. doi:10.1149/2.0861809jes.

[78] S. Liu, K.C. Smith, Quantifying the Trade-offs between Energy Consumption and Salt Removal Rate in Membrane-free Cation Intercalation Desalination, (n.d.).

[79] K. Singh, H.J.M. Bouwmeester, L.C.P.M. De Smet, M.Z. Bazant, P.M. Biesheuvel, Theory of Water Desalination with Intercalation Materials, Phys. Rev. Appl. 9 (2018) 64036. doi:10.1103/PhysRevApplied.9.064036.

[80] W. Zhao, L. Guo, M. Ding, Y. Huang, H.Y. Yang, Ultrahigh-Desalination-Capacity Dual-Ion Electrochemical Deionization Device Based on Na3V2(PO4)3@C–AgCl Electrodes, ACS Appl. Mater. Interfaces. 10 (2018) 40540–40548. doi:10.1021/acsami.8b14014.

[81] D. Nam, K. Choi, Bismuth as a New Chloride-Storage Electrode Enabling the Construction of a Practical High Capacity Desalination Battery, J. Amercian Chem. Soc. 139 (2017) 11055−11063. doi:10.1021/jacs.7b01119.

[82] P. Srimuk, J. Lee, A. Tolosa, C. Kim, M. Aslan, V. Presser, Titanium Disulfide : A Promising Low-Dimensional Electrode Material for Sodium Ion Intercalation for Seawater Desalination, Chem. Mater. 29 (2017) 9964−9973. doi:10.1021/acs.chemmater.7b03363.

[83] Y. Huang, F. Chen, L. Guo, H.Y. Yang, Ultrahigh performance of a novel electrochemical deionization system based on a $NaTi_2(PO_4)_3$/rGO nanocomposite, J. Mater. Chem. A. 5 (2017) 18157–18165. doi:10.1039/C7TA03725B.

[84] L. Guo, Y. Huang, M. Ding, Z.Y. Leong, S. Vafakhah, H.Y. Yang, A high performance electrochemical deionization method to desalinate brackish water with an FePO4/RGO nanocomposite, J. Mater. Chem. A. 6 (2018) 8901–8908. doi:10.1039/c8ta01361f.

[85] C. Meyer, H. Bockholt, W. Haselrieder, A. Kwade, Characterization of the calendering process for compaction of electrodes for lithium-ion batteries, J. Mater. Process. Technol. 249 (2017) 172–178. doi:10.1016/j.jmatprotec.2017.05.031.

[86] G.F. Yang, S.K. Joo, Calendering effect on the electrochemical performances of the thick

Li-ion battery electrodes using a three dimensional Ni alloy foam current collector, Electrochim. Acta. 170 (2015) 263–268. doi:10.1016/j.electacta.2015.04.119.

[87] Y. Sheng, C.R. Fell, Y.K. Son, B.M. Metz, J. Jiang, B.C. Church, Effect of Calendering on Electrode Wettability in Lithium-Ion Batteries, Front. Energy Res. 2 (2014) 1–8. doi:10.3389/fenrg.2014.00056.

[88] H. Kondo, H. Sawada, C. Okuda, T. Sasaki, Influence of the Active Material on the Electronic Conductivity of the Positive Electrode in Lithium-Ion Batteries, 166 (2019). doi:10.1149/2.0051906jes.

[89] E.R. Reale, A. Shrivastava, K.C. Smith, Effect of conductive additives on the transport properties of porous flow-through electrodes with insulative particles and their optimization for Faradaic deionization, Water Res. 165 (2019) 114995. doi:10.1016/j.watres.2019.114995.

[90] A. Hassanvand, G.Q. Chen, P.A. Webley, S.E. Kentish, Improvement of MCDI operation and design through experiment and modelling : Regeneration with brine and optimum residence time, Desalination. 417 (2017) 36–51. doi:10.1016/j.desal.2017.05.004.

[91] Q. Abbas, D. Pajak, Effect of binder on the performance of carbon/carbon symmetric capacitors in salt aqueous electrolyte, Electrochim. Acta. 140 (2014) 132–138. doi:10.1016/j.electacta.2014.04.096.

[92] H.-M. Li, K. Xu, B. Bourdon, H. Lu, Y.-C. Lin, J.A. Robinson, A.C. Seabaugh, S.K. Fullerton-Shirey, Electric Double Layer Dynamics in Poly(ethylene oxide) $LiClO_4$ on Graphene Transistors, J. Phys. Chem. C. 121 (2017) 16996–17004. doi:10.1021/acs.jpcc.7b04788.

[93] J.H. Kang, S.H. Lee, K.M. Yu, Development of a handheld sheet resistance meter with the

dual-configuration four-point probe method, J. Electr. Eng. Technol. 12 (2017) 1314–1319. doi:10.5370/JEET.2017.12.3.1314.

[94] U. Tröltzsch, O. Kanoun, Generalization of transmission line models for deriving the impedance of diffusion and porous media, Electrochim. Acta. 75 (2012) 347–356. doi:10.1016/j.electacta.2012.05.014.

[95] J.D. Flygare, A.A. Riet, B.A. Mazzeo, D.R. Wheeler, Mathematical Model of Four-Line Probe to Determine Conductive Properties of Thin-Film Battery Electrodes, J. Electrochem. Soc. 162 (2015) A2136–A2144. doi:10.1149/2.0571510jes.

[96] B.J. Lanterman, A.A. Riet, N.S. Gates, J.D. Flygare, A.D. Cutler, J.E. Vogel, D.R. Wheeler, B.A. Mazzeo, Micro-Four-Line Probe to Measure Electronic Conductivity and Contact Resistance of Thin-Film Battery Electrodes, J. Electrochem. Soc. 162 (2015) A2145–A2151. doi:10.1149/2.0581510jes.

[97] X. Ke, J.I.D. Alexander, J.M. Prahl, R.F. Savinell, A simple analytical model of coupled single flow channel over porous electrode in vanadium redox flow battery with serpentine flow channel, J. Power Sources. 288 (2015) 308–313. doi:10.1016/j.jpowsour.2015.04.138.

[98] A. You, M.A.Y. Be, I. In, Computer simulation study of the effective viscosity in Brinkman's equation, Phys. Fluids. 1434 (2010). doi:10.1063/1.868258.

[99] V.M. Starov, V.G. Zhdanov, Effective viscosity and permeability of porous media, Colloid Polym. Sci. 192 (2001) 363–375.

[100] M.M. Forouzan, M. Wray, L. Robertson, D.R. Wheeler, Tortuosity of Composite Porous Electrodes with Various Conductive Additives in an Alkaline System, J. Electrochem. Soc. 164 (2017) A3117–A3130. doi:10.1149/2.0911713jes.

[101] T. Kim, C.A. Gorski, B.E. Logan, Low Energy Desalination Using Battery Electrode Deionization Supporting Information, Environ. Sci. Technol. Lett. 4 (2017) 444–449. doi:10.1021/acs.estlett.7b00392.

[102] H. Yoon, J. Lee, S. Kim, J. Yoon, Electrochemical sodium ion impurity removal system for producing high purity KCl, Hydrometallurgy. 175 (2018) 354–358. doi:10.1016/j.hydromet.2017.12.017.

[103] F. Chen, Y. Huang, L. Guo, L. Sun, Y. Wang, H. Ying Yang, Dual-ions electrochemical deionization: a desalination generator, Energy Environ. Sci. (2017). doi:10.1039/c7ee00855d.

[104] L. Guo, M.R. Wei, W. Shi, Y. Huang, F. Chen, M. Ding, Z. Leong, H.Y. Yang, Prussian blue anode for high performance electrochemical deionization promoted by faradic mechanism, Nanoscale. (2017). doi:10.1039/C7NR03579A.

[105] P. Srimuk, J. Lee, S. Fleischmann, M. Aslan, C. Kim, V. Presser, Potential-dependent, switchable ion selectivity in aqueous media using titanium disulfide, ChemSusChem. 11 (2018) 2091-2100. doi:10.1002/cssc.201800452.

[106] J. Lee, P. Srimuk, K. Aristizabal, C. Kim, S. Choudhury, Y.C. Nah, F. Mücklich, V. Presser, Pseudocapacitive Desalination of Brackish Water and Seawater with Vanadium-Pentoxide-Decorated Multiwalled Carbon Nanotubes, ChemSusChem. 10 (2017) 3611–3623. doi:10.1002/cssc.201701215.

[107] M. Qin, A. Deshmukh, R. Epsztein, S.K. Patel, Comparison of energy consumption in desalination by capacitive deionization and reverse osmosis, Desalination. 455 (2019) 100–114. doi:10.1016/j.desal.2019.01.003.

[108] E.N. Guyes, A. Simanovski, M.E. Suss, Several orders of magnitude increase in the

hydraulic permeability of flow-through capacitive deionization electrodes via laser perforations, RSC Adv. 7 (2017) 21308–21313. doi:10.1039/C7RA00459A.

[109] C.H. Tian, R. Chein, K.L. Hsueh, C.H. Wu, F.H. Tsau, Design and modeling of electrolyte pumping power reduction in redox flow cells, Rare Met. 30 (2011) 16–21. doi:10.1007/s12598-011-0229-1.

[110] M. Al-Yasiri, J. Park, A novel cell design of vanadium redox flow batteries for enhancing energy and power performance, Appl. Energy. 222 (2018) 530–539. doi:10.1016/j.apenergy.2018.04.025.

[111] C.R. Dennison, E. Agar, B. Akuzum, E.C. Kumbur, Enhancing Mass Transport in Redox Flow Batteries by Tailoring Flow Field and Electrode Design, J. Electrochem. Soc. 163 (2015) A5163–A5169. doi:10.1149/2.0231601jes.

[112] M. Al-Yasiri, J. Park, Study on Channel Geometry of All-Vanadium Redox Flow Batteries, J. Electrochem. Soc. 164 (2017) A1970–A1982. doi:10.1149/2.0861709jes.

[113] G. Liu, H. Zheng, V. Battaglia, A.S. Simens, A.M. Minor, X. Song, Optimization of Acetylene Black Conductive Additive and Polyvinylidene Difluoride Composition for High Power Rechargeable Lithium-Ion Cells, ECS Trans. 6 (2007) 45–56. doi:10.1149/1.2811942.

[114] J.A. Shetzline, S.E. Creager, Quantifying Electronic and Ionic Conductivity Contributions in Carbon/Polyelectrolyte Composite Thin Films, J. Electrochem. Soc. 161 (2014) H917–H923. doi:10.1149/2.0621414jes.

[115] S. Nadakatti, M. Tendulkar, M. Kadam, Use of mesoporous conductive carbon black to enhance performance of activated carbon electrodes in capacitive deionization technology, Desalination. 268 (2011) 182–188. doi:10.1016/j.desal.2010.10.020.

[116] S. Hand, X. Shang, J.S. Guest, K.C. Smith, R.D. Cusick, Global sensitivity analysis to characterize operational limits and prioritize performance goals of capacitive deionization, Environ. Sci. Technol. (2019). doi:10.1021/acs.est.8b06709.

[117] J. Goodwin, Colloids and Interfaces with Surfactants and Polymers, First, Wiley, 2009.

[118] A. Maria, M. Mouas, A. Videcoq, M. Cerbelaud, M. Bienia, P. Bowen, R. Ferrando, How colloid – colloid interactions and hydrodynamic effects influence the percolation threshold : A simulation study in alumina suspensions, J. Colloid Interface Sci. 458 (2015) 241–246. doi:10.1016/j.jcis.2015.07.058.

[119] M. Cerbelaud, B. Lestriez, A. Videcoq, R. Ferrando, D. Guyomard, Understanding the Structure of Electrodes in Li-Ion Batteries: A Numerical Study, J. Electrochem. Soc. 162 (2015) A1485–A1492. doi:10.1149/2.0431508jes.

[120] J. Landesfeind, A. Eldiven, H.A. Gasteiger, Influence of the Binder on Lithium Ion Battery Electrode Tortuosity and Performance, J. Electrochem. Soc. 165 (2018) A1122–A1128. doi:10.1149/2.0971805jes.

[121] S. Dhaybi, B. Marsan, A. Hammami, A novel low-cost and simple colloidal route for preparing high-performance carbon-coated LiFePO4 for lithium batteries, J. Energy Storage. 18 (2018) 259–265. doi:10.1016/j.est.2018.05.009.

[122] S. Dhaybi, B. Marsan, LiFe0.5Mn0.5PO4/C prepared using a novel colloidal route as a cathode material for lithium batteries, J. Alloys Compd. 737 (2018) 189–196. doi:10.1016/j.jallcom.2017.12.064.

[123] Y.K. Cho, R. Wartena, S.M. Tobias, Y.M. Chiang, Self-assembling colloidal-scale devices: Selecting and using short-range surface forces between conductive solids, Adv. Funct. Mater. 17 (2007) 379–389. doi:10.1002/adfm.200600846.

[124] F. Ma, Y. Fu, V. Battaglia, R. Prasher, Microrheological modeling of lithium ion battery anode slurry, J. Power Sources. 438 (2019) 226994. doi:10.1016/j.jpowsour.2019.226994.

[125] K.G. Gallagher, S.E. Trask, C. Bauer, T. Woehrle, S.F. Lux, M. Tschech, P. Lamp, B.J. Polzin, S. Ha, B. Long, Q. Wu, W. Lu, D.W. Dees, A.N. Jansen, Optimizing Areal Capacities through Understanding the Limitations of Lithium-Ion Electrodes, J. Electrochem. Soc. 163 (2016) A138–A149. doi:10.1149/2.0321602jes.

[126] L. Zolin, M. Chandesris, W. Porcher, B. Lestriez, An Innovative Process for Ultra-Thick Electrodes Elaboration: Toward Low-Cost and High-Energy Batteries, Energy Technol. 7 (2019) 1–11. doi:10.1002/ente.201900025.

[127] J.N. Israelachvili, Intermolecular and Surface Forces, 3rd ed., Elsevier Inc., 2011.

[128] L. Bergstrom, Hamaker constants of inorganic materials Lennart, Adv. Colloid Interface Sci. 70 (1997) 125–169. doi:10.102/la201387d.

[129] R.R. Dagastine, D.C. Prieve, L.R. White, Calculations of van der Waals forces in 2-dimensionally anisotropic materials and its application to carbon black, J. Colloid Interface Sci. 249 (2002) 78–83. doi:10.1006/jcis.2002.8239.

[130] M.J. Synodis, C.L. Porter, N.M. Vo, A.J.L. Reszka, M.D. Gross, R.C. Snyder, A Model to Predict Percolation Threshold and Effective Conductivity of Infiltrated Electrodes for Solid Oxide Fuel Cells, J. Electrochem. Soc. 160 (2013) F1216–F1224. doi:10.1149/2.035311jes.

[131] M. Cerbelaud, B. Lestriez, A. Videcoq, R. Ferrando, D. Guyomard, Understanding the Structure of Electrodes in Li-Ion Batteries: A Numerical Study, J. Electrochem. Soc. 162 (2015) A1485–A1492. doi:10.1149/2.0431508jes.

[132] H. Sis, M. Birinci, Effect of nonionic and ionic surfactants on zeta potential and dispersion

properties of carbon black powders, Colloids Surfaces A Physicochem. Eng. Asp. (2017). doi:10.1016/j.colsurfa.2009.03.039.

[133] B.P. Singh, R. Menchavez, C. Takai, M. Fuji, M. Takahashi, Stability of dispersions of colloidal alumina particles in aqueous suspensions, J. Colloid Interface Sci. 291 (2005) 181–186. doi:10.1016/j.jcis.2005.04.091.

[134] E. Thormann, On understanding of the Hofmeister effect: How addition of salt alters the stability of temperature responsive polymers in aqueous solutions, RSC Adv. 2 (2012) 8297–8305. doi:10.1039/c2ra20164j.

[135] K. Singh, Z. Qian, P.M. Biesheuvel, H. Zuilhof, S. Porada, Nickel hexacyanoferrate electrodes for high mono/divalent ion-selectivity in capacitive deionization, Desalination. 481 (2020) 114346. doi:10.1016/j.desal.2020.114346.

[136] S.K. Patel, C.L. Ritt, A. Deshmukh, Z. Wang, M. Qin, R. Epsztein, M. Elimelech, The relative insignificance of advanced materials in enhancing the energy efficiency of desalination technologies, Energy Environ. Sci. 13 (2020) 1694–1710. doi:10.1039/d0ee00341g.

[137] J. Ahn, S. Kim, S. il Jeon, C. Lee, J. Lee, J. Yoon, Nafion-coated Prussian blue electrodes to enhance the stability and efficiency of battery desalination system, Desalination. (2020) 114778. doi:10.1016/j.desal.2020.114778.

[138] S. Bortolin, P. Toninelli, D. Maggiolo, M. Guarnieri, D. Del Col, CFD study on electrolyte distribution in redox flow batteries, J. Phys. Conf. Ser. 655 (2015) 012049. doi:10.1088/1742-6596/655/1/012049.

[139] A. Bhattarai, N. Wai, R. Schweiss, A. Whitehead, T.M. Lim, H.H. Hng, Advanced porous electrodes with flow channels for vanadium redox flow battery, J. Power Sources. 341

(2017) 83–90. doi:10.1016/j.jpowsour.2016.11.113.

[140] X. Wang, Y. Duan, W. Yan, X. Peng, Effects of flow channel geometry on cell performance for PEM fuel cells with parallel and interdigitated flow fields, Electrochim. Acta. 53 (2008) 5334–5343. doi:10.1016/j.electacta.2008.02.095.

[141] R. Zhao, S. Porada, P.M. Biesheuvel, A. Van der Wal, Energy consumption in membrane capacitive deionization for different water recoveries and flow rates, and comparison with reverse osmosis, Desalination. 330 (2013) 35–41. doi:10.1016/j.desal.2013.08.017.

[142] J. Marschewski, L. Brenner, N. Ebejer, P. Ruch, B. Michel, D. Poulikakos, 3D-printed fluidic networks for high-power-density heat-managing miniaturized redox flow batteries, Energy Environ. Sci. (2017) 780–787. doi:10.1039/c6ee03192g.

[143] P.A. García-Salaberri, T.C. Gokoglan, S.E. Ibáñez, E. Agar, M. Vera, Modeling the effect of channel tapering on the pressure drop and flow distribution characteristics of interdigitated flow fields in redox flow batteries, Processes. 8 (2020) 1–26. doi:10.3390/PR8070775.

[144] Q. Li, Y. Zheng, D. Xiao, T. Or, R. Gao, Z. Li, M. Feng, L. Shui, G. Zhou, X. Wang, Z. Chen, Faradaic Electrodes Open a New Era for Capacitive Deionization, Adv. Sci. 2002213 (2020). doi:10.1002/advs.202002213.

[145] F. Liu, O. Coronell, D.F. Call, Electricity generation using continuously recirculated flow electrodes in reverse electrodialysis, J. Power Sources. 355 (2017) 206–210. doi:10.1016/j.jpowsour.2017.04.061.

[146] K.C. Smith, Y. Chiang, W.C. Carter, Maximizing Energetic Efficiency in Flow Batteries Utilizing Non-Newtonian Fluids, J. Electrochem. Soc. 161 (2014) 486–496. doi:10.1149/2.011404jes.

[147] K.H. Chen, M.J. Namkoong, V. Goel, C. Yang, S. Kazemiabnavi, S.M. Mortuza, E. Kazyak, J. Mazumder, K. Thornton, J. Sakamoto, N.P. Dasgupta, Efficient fast-charging of lithium-ion batteries enabled by laser-patterned three-dimensional graphite anode architectures, J. Power Sources. 471 (2020) 228475. doi:10.1016/j.jpowsour.2020.228475.

[148] H. Hu, W. Liu, M. Zhu, Y. Lin, Y. Liu, J. Zhang, T. Chen, K. Liu, Yolk-shell Prussian blue nanoparticles with fast ion diffusion for sodium-ion battery - Supplementary Data, Mater. Lett. 249 (2019) 206–209. doi:10.1016/j.matlet.2019.04.102.

[149] Y. Xu, M. Ou, Y. Liu, J. Xu, X. Sun, C. Fang, Q. Li, J. Han, Y. Huang, Crystallization-induced ultrafast Na-ion diffusion in nickel hexacyanoferrate for high-performance sodium-ion batteries, Nano Energy. 67 (2020) 104250. doi:10.1016/j.nanoen.2019.104250.

[150] H. Wang, T. Zhang, C. Chen, M. Ling, Z. Lin, S. Zhang, F. Pan, High-performance aqueous symmetric sodium-ion battery using NASICON-structured Na2VTi(PO4)3, Nano Res. 11 (2018) 490–498.

[151] S. Qiu, X. Wu, M. Wang, M. Lucero, Y. Wang, J. Wang, Z. Yang, W. Xu, Q. Wang, M. Gu, J. Wen, Y. Huang, Z.J. Xu, Z. Feng, NASICON-type Na3Fe2(PO4)3 as a low-cost and high-rate anode material for aqueous sodium-ion batteries, Nano Energy. 64 (2019) 103941. doi:10.1016/j.nanoen.2019.103941.